MICRO/NANO-PATTERNING OF SUPPORTED LIPID BILAYERS: BIOPHYSICAL STUDIES AND MEMBRANE-ASSOCIATED SPECIES SEPARATION

A Dissertation

by

JINJUN SHI

Submitted to the Office of Graduate Studies of
Texas A&M University
in partial fulfillment of the requirements for the degree of

DOCTOR OF PHILOSOPHY

May 2008

Major Subject: Chemistry

MICRO/NANO-PATTERNING OF SUPPORTED LIPID BILAYERS: BIOPHYSICAL STUDIES AND MEMBRANE-ASSOCIATED SPECIES SEPARATION

A Dissertation

by

JINJUN SHI

Submitted to the Office of Graduate Studies of
Texas A&M University
in partial fulfillment of the requirements for the degree of

DOCTOR OF PHILOSOPHY

Approved by:

Chair of Committee,	Paul S. Cremer
Committee Members,	Gregory D. Reinhart
	D. Wayne Goodman
	Paul A. Lindahl
Head of Department,	David H. Russell

May 2008

Major Subject: Chemistry

ABSTRACT

Micro/Nano-Patterning of Supported Lipid Bilayers: Biophysical Studies and Membrane-Associated Species Separation. (May 2008)

Jinjun Shi, B.S., Tsinghua University, China

Chair of Advisory Committee: Dr. Paul S. Cremer

Micro/nano-patterning of supported lipid bilayers (SLBs) has shown considerable potential for addressing fundamental biophysical questions about cell membrane behavior and the creation of a new generation of biosensors. Herein are presented several novel lithographic methods for the size-controlled patterning of SLBs from the microscale to the nanoscale. Using these methods, chemically distinct types of phospholipid bilayers and/or Escherichia Coli (E. Coli) membranes can be spatially addressed on a single microchip. These arrays can, in turn, be employed in the studies of multivalent ligand-receptor interactions, enzyme kinetics, SLBs size limitation, and membrane-associated species separation.

The investigations performed in the Laboratory for Biological Surface Science include the following projects. Chapters II and III describe the creation of lab-on-a-chip based platforms by patterning SLBs in microfluidic devices, which were employed in high throughput binding assays for multivalent ligand-receptor interactions between cholera toxin B subunits (CTB) and ganglioside GM_1. The studies on the effect of ligand density for multivalent CTB-GM_1 interactions revealed that the CTB-GM_1

binding weakened with increasing GM_1 density. Such a result can be explained by the clustering of GM_1 on the supported phospholipid membranes, which in turn inhibits the binding of CTB. Chapter IV characterizes the enzymatic activity of phosphatase tethered to SLBs in a microfluidic device. Higher turnover rate and catalytic efficiency were observed at low enzyme surface densities, ascribing to the low steric crowding hindrance and high enzyme fluidity, as well as the resulting improvement of substrate accessibility and affinity of enzyme catalytic sites. Chapter V presents sub-100 nm patterning of supported biomembranes by atomic force microscopy (AFM) based nanoshaving lithography. Stable SLBs formed by this method have a lower size limit of ~ 55 nm in width. This size limit stems from a balance between a favorable bilayer adhesion energy and an unfavorable bilayer edge energy. Finally, chapter VI demonstrates the electrophoretic separation of membrane-associated fluorophores in polymer-cushioned lipid bilayers. This electrophoretic method was applied to the separation of membrane proteins in E. Coli ghost membranes.

DEDICATION

To my parents, Huixin Shi and Lengqing Li

And to my wife, Yujing Lu

ACKNOWLEDGEMENTS

First of all, I would like to give my deepest gratitude to my advisor Dr. Paul S. Cremer for his elegant advice, patient guidance, and great encouragement throughout my study at Texas A&M University. His wide knowledge, enthusiasm towards science, and creative thinking have been of great value to me. More importantly, the free environment of pursuing science in his group lets my imagination soar. I would also like to thank Dr. Goodman, Dr. Reinhart, and Dr. Lindahl for serving as my committee members and for their guidance and helpful advice.

Next, I thank the group members in Cremer laboratory: "without your help, I could not have done this." I especially thank Tinglu and Yanjie for their help and guidance in and outside of the laboratory. When I meet with trouble, you are the first two that show up to help me. To Xin, Jixin, Weissu, Arnaldo, Susan, Sho, Matt, Hyunsook, Younhee, Tao, and Richard, thank you so much for your helpful discussions, encouragement, and dedication to my research work. I also thank Arnaldo and Younhee for their friendship with me and thank Sean and Vanessa for their help with my English.

Thanks also go to my friends in the USA, especially to Agu, SunLi, Xiaolin, LiuLu, Yajie, Wentao, Qingyang, Hui, Shuzhi, KongKe, Liangxing, and Kin. Thank you for your constant help and encouragement. I also thank Dr. Xinrong Zhang at Tsinghua University in China. Thank you, Lao Zhang, for encouraging me and for trusting that I can be a good scientist. Thank you, Chao, Sichun, and the Zhang group, for your past, present, and future help.

Finally, I thank my mother, Lengqing, my father, Huixin, and my wife, Yujing. Mom and Dad, thanks for your forever love and support and your belief that I can be excellent at whatever I chose. I owe you a great debt of gratitude. Yujing, my beloved wife, thanks for your encouragement when I feel frustrated, your belief that I am the best in your heart, and your patience and love. I dedicate my dissertation to you!

Financial support from the National Institutes of Health (NIH) and the Army Research Office (ARO) is also acknowledged.

TABLE OF CONTENTS

Page

LIST OF FIGURES

FIGURE Page

FIGURE Page

LIST OF TABLES

TABLE Page

CHAPTER I

INTRODUCTION

Objective

Surface patterning in array formats has become a commonly used methodology in a variety of fields including biochemistry, biotechnology, chemistry, materials science, etc.[1-4] Such array systems have been successfully employed in high throughput assays for drug design, gene sequencing, new material discovery, and chemical/bio-sensing.[5-8] Although supported lipid bilayers (SLBs) provide an excellent model system to mimic the properties of cellular membranes, lipid bilayer patterning on surfaces has not been well considered until late 1990s.[9,10] Recently, micro/nano-patterned SLB arrays have shown great potential for addressing fundamental biophysical questions about cell membrane behavior and creating a new generation of biosensors.[11-13] The research presented in this dissertation aims to develop novel lithographic techniques for patterning SLBs on planar surfaces and address some biophysical and bioanalytical questions including multivalent ligand-receptor interactions, enzyme kinetics, size limitations of SLBs, and membrane protein separation.

Since the pioneering work of partitioning SLBs into lithographically patterned grids in 1997, a number of techniques have been developed for bilayer surface patterning, including microcontact printing, photolithography, etc.[10,13,14] Among them,

---

This dissertation follows the style of *Journal of the American Chemical Society*.

SLBs patterning inside microfluidic devices provided a powerful on-chip platform for studying ligand-receptor interactions and enzyme kinetics with high throughput and low sample consumption properties.[15-17] Chapters II and IV extend such bilayer-coated microfluidics to the studies of multivalent CTB-GM_1 interactions and phosphatase enzyme kinetics as a function of ligand and enzyme density.

Although each of the achieved SLBs patterning techniques has its merits, two problems remain unsolved: (1) spatially addressing bilayer arrays inside individual microfluidic channels, and (2) size-controlled patterning of bilayers from the microscale to the sub-100 nm scale. Chapters III and V seek to develop novel lithographic methods to achieve the specific goals. By utilizing deep UV lithography, Chapter III demonstrates that the light exposed protein monolayer in microchannels can be removed and SLBs can be subsequently deposited over the exposed area. In a sequential patterning procedure, SLB patches with different components are spatially addressed into individual microfluidic channels. Such a bilayer array-coated microfluidic device is proven to be suitable for multiple multivalent ligand-receptor interactions measurement in one-shot experiments. Chapter V presents a size-controlled patterning technique by using AFM-based nanoshaving lithography. The method enables the study of inherent size limitations of SLBs.

Besides its great potential in biophysical studies, lipid bilayer patterning has also been applied in bioanaltyical science. For instance, the patterning of SLBs containing small molecules, peptides, and membrane proteins is of great importance in biosensor array design.[11,18] The separation of membrane-bound dyes by SLB electrophoresis also requires the patterning of one SLB adjacent to another.[19] Chapter VI aims to pattern Escherichia Coli (E. Coli) membrane containing membrane proteins next to polymer-supported lipid bilayer medium and separate the proteins by electrophoresis. Membrane protein separation and purification are tough tasks since many of the proteins are water insoluble and easily lose their structure and function.[20] Thus, typical protein separation methods such as two-dimensional polyacrylamide gel electrophoresis (2D-PAGE) are not well suitable.[19,20] The proposed strategy in Chapter VI may allow us to circumvent the drawbacks.

Supported Lipid Bilayers

Supported Lipid Bilayers (SLBs), first pioneered by McConnell and his co-workers[21,22] two decades ago, retain many of the structural and dynamic properties of cellular membranes (Figure 1.1).[9] For instance, the lateral lipid mobility is preserved by a thin water layer (~ 1 nm) trapped between the membrane and the underlying solid surface, and thus allows for the reorganization of membrane components.[23-25] SLBs also provide a natural environment for embedding membrane proteins, receptors, membrane fragments, etc.[26] Therefore, SLBs have served as biomimetics for a variety of chemical and biological processes which occur in cellular membranes.[9] Examples include lipid phase separation[27], lipid rafts formation[28], membrane fusion and fission[29,30], enzymatic reactions[17,31], ligand-receptor interactions[16,32-34], cell adhesion and growth[35,36], immunological synapse[37], viral attack[38], etc. Besides, SLBs are of great importance in

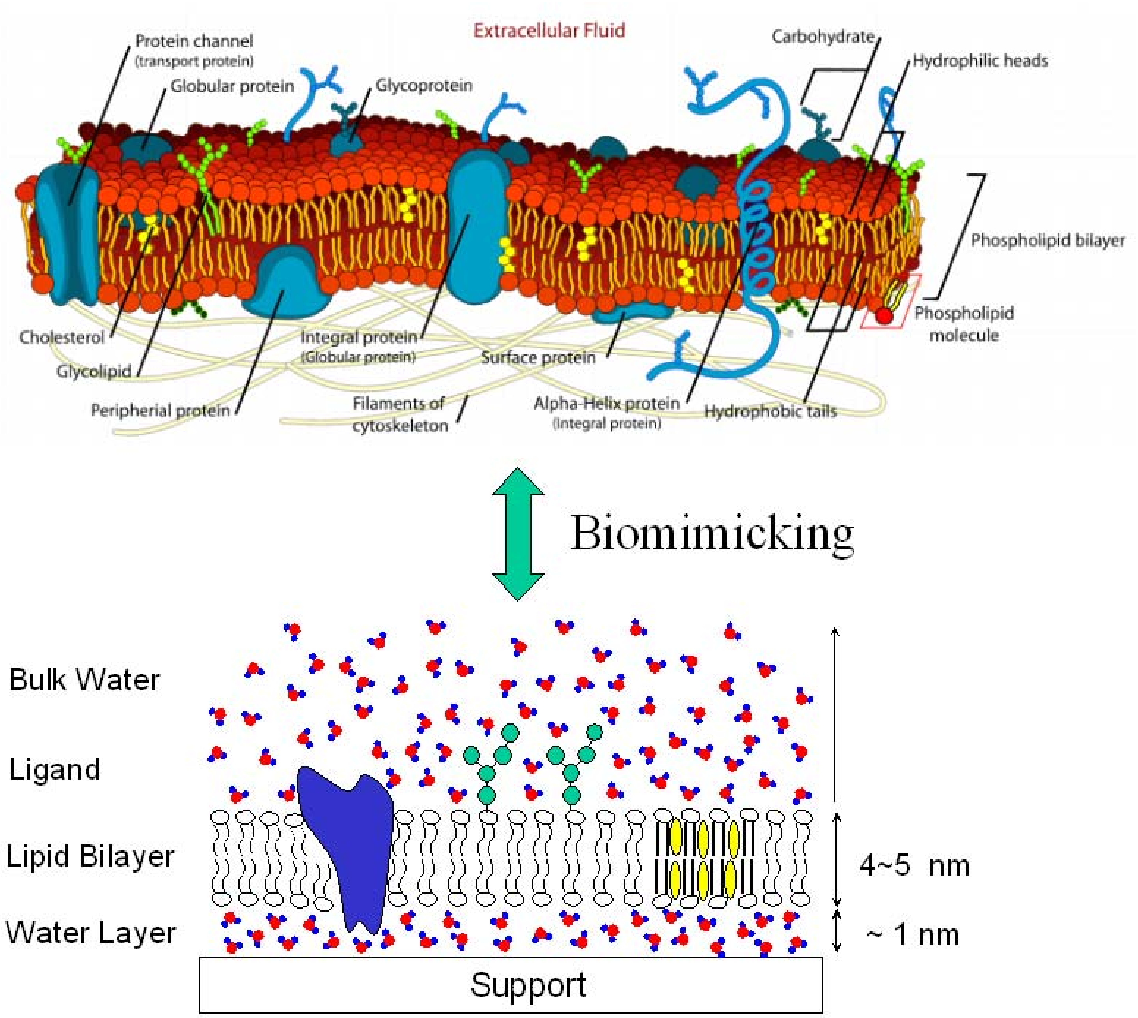

Figure 1.1. Supported Lipid Bilayers biomimicking cellular membranes. The top image is a fluid mosaic model of cellular membranes and the bottom image is a schematic representation of supported lipid bilayers. The top image was adapted from www.wikipedia.org.

chemical/biological sensing[11], drug discovery[12], membrane-associated compounds separation[19,39], protein purification[40,41], prevention of protein adsorption in capillary electrophoresis[42,43], and fabrication of matrices for tissue engineering[44].

SLBs can be formed by two general methods (Figure 1.2). In the first method, the lower leaflet of the bilayer is formed by the Langmuir–Blodgett technique. The hydrophobic tails of the lipids from the air-water interface will orient themselves toward the air, while the polar headgroups toward the hydrophilic substrate. The upper leaflet is formed by the Langmuir-Schaffer procedure, which involves horizontally dipping the substrate to create the second leaflet.[22] The second method is called vesicle fusion.[21,45] In this technique, SLBs are formed through the fusion of small unilamellar vesicles (SUVs) to a planar solid substrate. SUVs are prepared by either sonication or vesicle extrusion.[46-48] Either way it is relatively straightforward to incorporate these SLBs with species including peptides, channel forming proteins, ligands, etc.

To support fluid lipid bilayers, the solid substrate surface should be smooth and clean.[9,13] These substrates can be broadly classified into four categories (Figure 1.3). (1) The commonly used materials known to support lipid bilayers include borosilicate glass, fused quartz, mica, oxidized Si, etc.[10,22,49] These surfaces are hydrophilic and need no further modification. (2) Some conducting substrates such as gold are not suitable for SLBs formation. By modifying the conducting surfaces with self-assembled monolayers (SAM) of alkanethiols, one lipid monolayer can be deposited on the well-defined hydrophobic surface (Figure 1.3b).[50] This kind of system is called supported hybrid bilayer.[51] If the SAMs are generated by ω-functionalized alkanethiols, it will

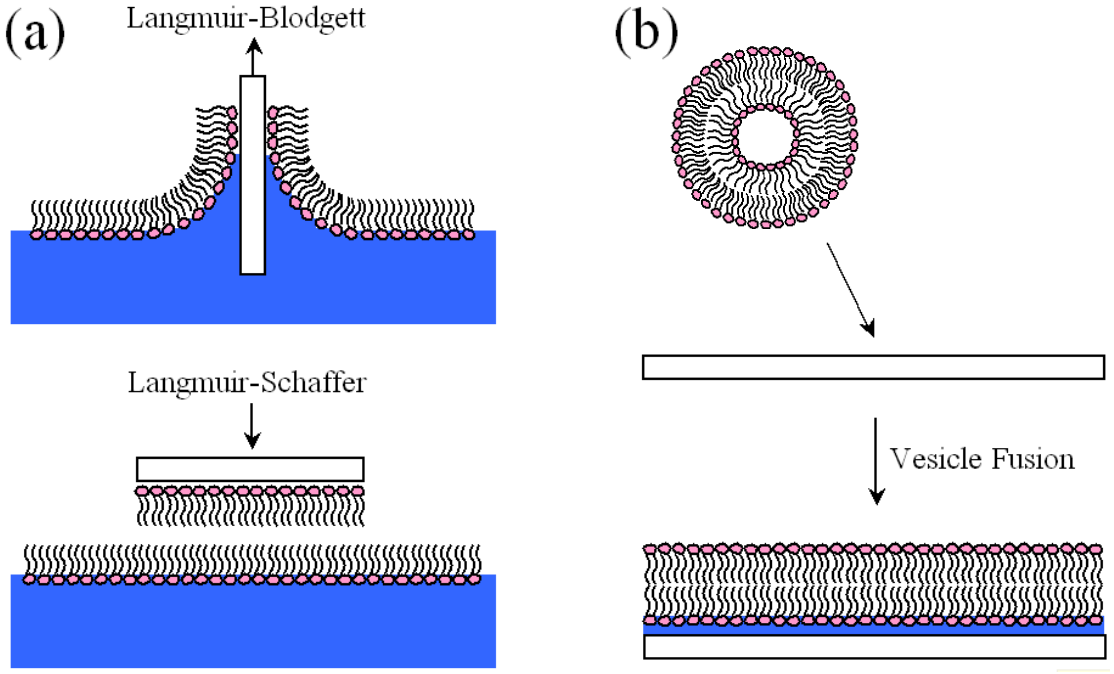

Figure 1.2. Two general methods for SLBs formation: (a) Langmuir-Blodgett pulling for the bottom layer and Langmuir-Schaffer pushing for the top layer, (b) vesicle fusion.

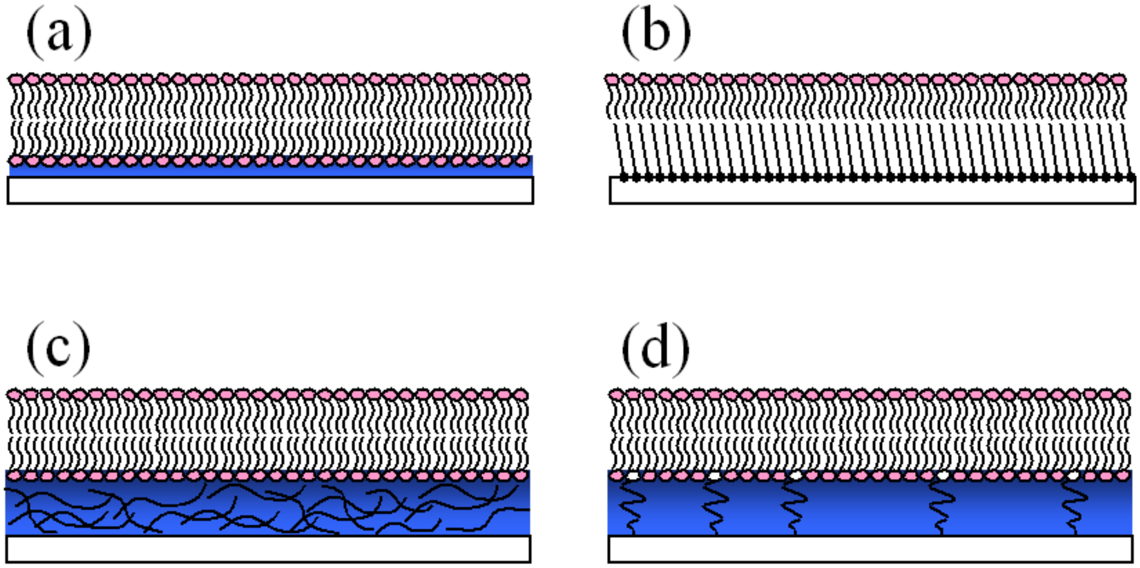

Figure 1.3. Four categories of supported lipid bilayers: (a) solid-supported lipid bilayer, (b) hybrid lipid bilayer, (c) polymer-cushioned lipid bilayer, and (d) tethered bilayer lipid membrane.

facilitate the formation of lipid bilayers.[52] Although both of the above SLB models provide useful platforms for studying ligand-receptor interactions, cell adhesion, lipid raft formation, etc., they have one fundamental drawback. When transmembrane proteins, especially those presenting large peripheral domains, are incorporated in these SLBs, the bilayer-substrate distance (~ 1 nm) does not provide a sufficient internal water reservoir to avoid the direct contact between proteins and the solid surface, thus causing the denaturation of proteins.[13,26]

To overcome this drawback, two strategies are provided by modifying the underlying substrate with cushions or tethers.[26] (3) Polymer-cushioned lipid bilayers separate the membranes from the solid substrate by adding one hydrophilic polymer layer between the bilayer and substrate (Figure 1.3c). These polymer cushions, such as cellulose[53-55], dextran[56], and polyelectrolytes[57-61], can reduce the frictional coupling between membrane-incorporated proteins and the solid support. (4) The alternative SLB model is called tethered bilayer lipid membrane (tBLM). This strategy uses lipopolymer tethers, which include one terminal group that binds to the substrate, another terminal group that inserts into the lipid bilayer, and a hydrophilic linker (e.g. polyethylene glycol, PEG) that defines the water/ionic reservoir (Figure 1.3d).[62-66] The reservoir space, controlled by the linker length, decouples the bilayer from the surface and enables the functional reconstitution of transmembrane proteins. Such tBLM can also be created by attaching biotinylated vesicles to the surface through biotin-streptavidin interaction followed by PEG-triggered fusion of vesicles to form a planar bilayer.[67,68]

Patterning of Supported Lipid Bilayers

One key feature of SLBs is the lateral fluidity of lipid molecules, which distinguishes them from other surfaces and allows them to closely resemble cellular membranes. However, the lipid mobility also means the membrane components are continually mixing. Surface patterning of fluid lipid bilayers preserves many of their distinctive properties of cell surfaces while creating broad opportunities for the manipulation, control, and analysis of membranes, and the reaction environments.[10,14,69] Moreover, large SLB arrays presenting combinatorial libraries of small molecules, peptides, or proteins provide an extremely rapid and powerful means of data collection.[13]

Surface patterning of lipid bilayers has been achieved by a variety of techniques that can fall into two broad categories: indirect and direct patterning. Indirect methods first introduce pre-patterned barriers into the solid substrate to prevent lipid diffusion, and then assemble lipid bilayers into the corrals. Barrier pre-patterning can be constructed by using photolithography, soft lithography, electron-beam lithography, scanning probe lithography, and microcontact printing, with a variety of barrier materials including plastic, metals, metal dioxides, semiconductors, proteins, photoresists, polymers, and polymerized lipid bilayers.[10,14-18,70-77] Direct patterning methods include simple mechanical scratching[70,71], poly-dimethylsilane (PDMS) stamping and blotting[72-74], hydrogel stamping[75], polymer lift-off[76], robotic pin printing[77,78], deep ultraviolet (deep UV) lithography[79,80], air bubble collapse[81], and dip-pen nanolithography[82]. Most of the techniques show the ability controlling the size of SLB patterns down to micron scale. Dip-pen nanolithography[82] and nanoshaving lithography[83] are till now the only methods that can achieve sub-100 nm patterning of SLBs.

Among these patterning methods, some are capable of spatially addressing different bilayer chemistries in one array. For example, Cremer and Yang[18] first showed the use of pulled microcapillaries to deliver unique vesicle solutions to an array of hydrophilic patches patterned on a substrate with hydrophobic barriers. Subsequently, other methods have been developed for the same purpose, including microcontact printing,[73-75] laminar flow vesicle deposition,[84] mechanical erasing and writing,[70] robotic pin printing,[78] scanning probe lithography,[85] and dip-pen nanolithography.[82]

Applications of Lipid Bilayer Arrays

Since the emergence of lipid membrane patterning technique developed by Groves et al.[10], micro/nano-patterning of SLBs has shown great potential in fundamental and applied bioanalytical and biophysical research. Due to its capability of presenting different biologically functional species, SLB arrays play a pivotal role in the development of biosensors, proteomics, and drug discovery.[11-13,69] For example, small SLB arrays containing different concentrations of DNP hapten and cholesterol have been made for antibody sensing.[18,86] Submicron-sized SLBs inside Au nanoholes has been employed for label-free biorecognition in conjunction with localized surface plasmon resonance.[87,88] It is also believed that the SLB arrays incorporated with membrane proteins could provide valuable information for biological warfare sensing and for the discovery of new drugs.[12,69] A recent application of SLBs patterning is membrane-bound compounds separation by supported bilayer electrophoresis.[19]

These patterned lipid bilayers can also be employed to address fundamental biophysical questions about cell membrane behaviors. Micro-patterned SLBs have been applied in the investigation of cell adhesion and growth, radial location of T-cell receptors in immunological synapses, and membrane compartmentalization during receptor-mediated signaling.[35,37,89-91] By incorporating SLB arrays in microfluidic devices, it provides a high-throughput platform for studying multivalent ligand-receptor interactions and enzymatic reactions at lipid membrane interfaces, and phase transition of lipid membranes.[15-17,31,34,92-96]

CHAPTER II

GM_1 CLUSTERING INHIBITS CHOLERA TOXIN BINDING IN SUPPORTING PHOSPHOLIPID MEMBRANES

Introduction

Multivalent ligand-receptor interactions are frequently utilized by nature because their properties can be remarkably different from the corresponding monovalent recognition events. For example, multivalent interactions can achieve tighter binding, enhance receptor selectivity, induce receptor clustering on cell surfaces, and control signal transduction within cells.[97] A great diversity of biological processes including cell signaling[98] and cell-pathogen interactions[99-101] are associated with multivalent ligand-receptor binding. The recognition of cholera toxin (CT) by ganglioside GM_1 is considered to be a paradigm of multivalent carbohydrate-protein binding.[102] Understanding the underlying physical chemistry of this model system should therefore lead to a better appreciation of multivalent binding phenomena and may provide insight into strategies for inhibitory drug design.[97,99,103,104]

Cholera toxin is a member of the AB_5 class of cytotoxins, composed of a catalytically active A subunit and doughnut-shaped homopentameric B subunits that recognize and bind to the pentasaccharide moiety of GM_1 in the cell's membrane. The interaction of cholera toxin or its pentameric B-subunits with GM_1 has been investigated

---

*Reproduced with permission from "GM_1 Clustering Inhibits Cholera Toxin Binding in Supported Phospholipid Membranes" by Shi, J. J.; Yang, T. L.; Kataoka, S.; Zhang, Y. J.; Diaz, A. J.; Cremer, P. S. *J. Am. Chem. Soc.* **2007**, 129, 5954-5961. Copyright 2007 American Chemical Society.

by using a variety of techniques. ^{125}I-labeled CT was first utilized to study binding on isolated fat cells and liver membranes,[105,106] and intestinal cells[107]. Thermodynamic data were obtained by isothermal titration calorimetry.[108,109] Surface plasmon resonance was used to obtain the kinetics of CTB binding to GM_1 in supported bilayers[110,111] and in vesicles[112,113]. Other diagnostic methods used to explore CTB-GM_1 binding include quartz crystal microbalance analysis,[114] flow cytometry,[115] fluoroimmunoassays,[116] fluorescence resonance energy transfer,[117] atomic force microscopy,[118] and a novel colloid phase transition method.[33,119] The buffer conditions, temperatures, ionic strengths, and membrane chemistries varied amongst the different experiments. Accordingly, the measured values for the apparent dissociation constant, K_{Dapp}, ranged from 4.55 pM[111] on the low end to 41 nM[33] and even 370 nM[94] on the high end.

In multivalent binding systems ligand density is a key parameter, since it affects ligand distribution and interligand distance.[97,99,104,120,121] We previously showed that K_{Dapp} for an antibody-antigen binding system tightened by a factor of ~ 12 as the ligand density increased from 0.1% to 5.0 mol% in a supported phospholipid membrane.[16] The hapten was a dinitrophenyl (DNP) moiety covalently conjugated to the headgroup of a phospholipid, which was recognized by an anti-DNP IgG. The change in K_{Dapp} with ligand density could be predicted extremely well by taking into account the dissociation constants for the individual steps in a sequential binding model:

$$K_{Dapp} = \frac{K_{D1}K_{D2}}{K_{D2} + 2[L]_s} \tag{1}$$

where K_{D1} and K_{D2} are the equilibrium dissociation constants for the first and second binding events, respectively, and *[L]ₛ* is the surface density of the ligands in the lipid bilayer.

Beyond bivalent binding, very little work has been done to probe the effect of membrane ligand density for the binding of proteins with multiple binding pockets. Indeed, the thermodynamics and kinetics of CTB-GM_1 binding have typically been studied at only one or a few ligand densities at a time. Curiously, MacKenzie et al.[112] showed data that indicated approximately 4 times tighter apparent binding of CTB to liposomes containing 2.0 mol% GM_1 than those containing 4.0 mol% GM_1. Lencer et al.[122] investigated cholera toxin binding to an intestinal microvillus membrane during development that possessed different GM_1 ligand densities. In that case, the binding also appeared to be stronger at lower ligand density. These results led us to hypothesize that a systematic study of multivalent CTB-GM_1 binding over a range of GM_1 concentrations could reveal that a different binding mechanism was at work than in the simple case of the bivalent ligand-receptor interaction of the DNP/anti-DNP system.

In Chapter II, a series of binding experiments were performed within microfluidic channels coated with 1-palmitoyl-2-oleoyl-sn-glycero-3-phosphocholine (POPC) bilayers containing GM_1. The results showed that the binding of CTB was continuously weakened as the ligand density was increased. Atomic force microscopy (AFM) studies revealed GM_1 clustering on the phospholipid membranes, which became more pronounced at increased GM_1 densities. Based on these observations, it is suggested that CTB binding to GM_1 is inhibited by the clustering of the glycolipid within the phospholipid membrane (Figure 2.1).

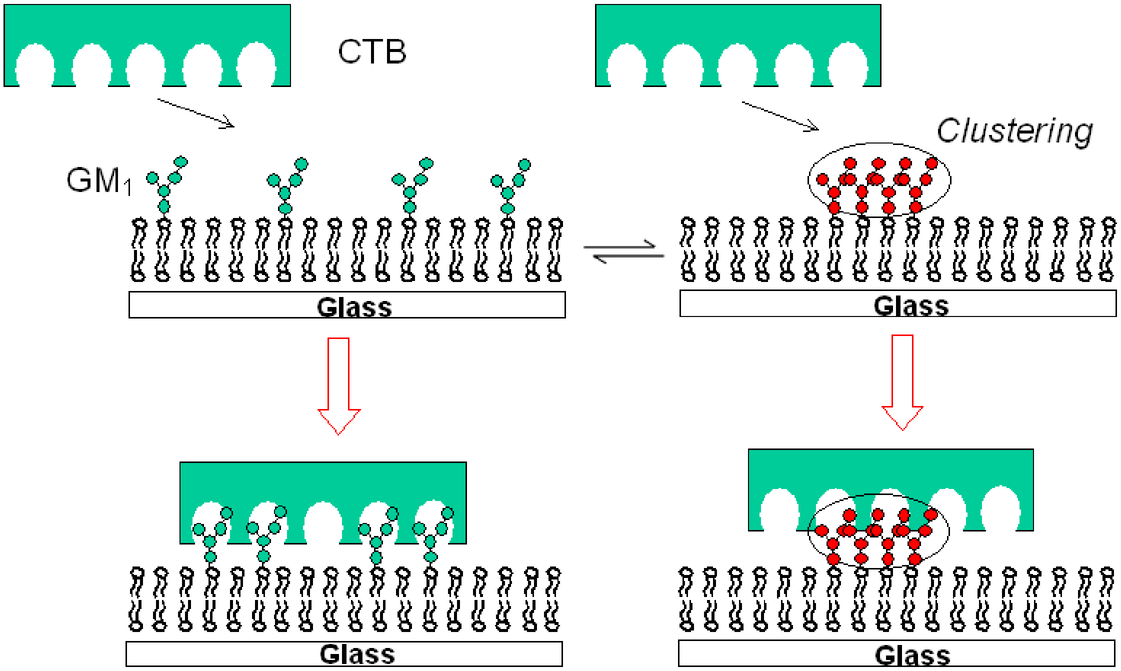

Figure 2.1. Schematic representation of the inhibition of CTB binding by GM_1 clustering on supported POPC bilayers. For simplicity GM_1 molecules in the lower leaflet are not drawn.

Experimental

Materials Ganglioside GM_1 (Brain, Ovine-Ammonium Salt) and POPC were obtained from Avanti Polar Lipids (Alabaster, AL). Texas Red-DHPE and Rabbit IgG antibodies were purchased from Molecular Probes, Inc. (Eugene, OR). CTB from *Vibrio cholerae* was purchased from Sigma-Aldrich. The CTB was labeled with Alexa Fluor-594 dye by using a standard protein-labeling kit (A10239, Molecular Probes, Eugene, OR). Labeling yielded ~ 0.8 fluorophores per protein as determined by UV/Vis absorption spectroscopy. The dye-labeled protein was stored in a phosphate buffered saline (PBS) solution containing 10 mM sodium phosphate, 150 mM NaCl, and 0.2 mM sodium azide. The pH of the PBS was set to 7.2 by dropwise addition of 2.0 M NaOH. The same buffer was also used for vesicle preparation and the successive dilution of protein solutions. Purified water for these experiments came from a NANOpure Ultrapure Water System (18.2 MΩ·cm, Barnstead, Dubuque, IA).

Microfluidic Devices Fabrication We employed microfluidic devices and total internal reflection fluorescence microscopy to study CTB-GM_1 interactions using our previously established methods.[15,16] The devices were made from planar borosilicate glass substrates and lithographically patterned polydimethylsiloxane (PDMS) molds. The devices afforded high throughput capabilities and had extremely low sample consumption compared with traditional analytical tools. Additionally, the glass and PDMS surfaces served as good supports for fluid phospholipid bilayers.[9] Lipid mobility was preserved because a thin water layer (~ 1 nm thick)[25] was trapped between the phospholipid bilayer and the underlying solid surface. Lipid molecules in the membrane were thus able to diffuse laterally to accommodate multivalent interactions.

The seven-channel microfluidic devices used in these experiments were fabricated by soft lithographic techniques.[15,123] In a first step, microfluidic channels were designed with Corel Draw software (Version 9, Corel Corp.). By printing out the design and transferring it onto black and white high-contrast Kodak technical pan film, the image could be used as a photomask for photolithography. Soda-lime glass slides were cleaned in hot surfactant solution (ICN x7 detergent, Costa Mesa, CA) for 1 h, rinsed with copious amounts of purified water, and dried with nitrogen gas. Next, the glass slides were coated with a thin layer of hexamethyldisilazane (HMDS) to improve adhesion of the photoresist to the glass surface,[124] followed by spin coating with Shipley 1827 photoresist. The substrates were then exposed to UV light through the photomask and treated with developing solution. After baking the photoresist/glass systems at 120 °C overnight, the substrates were immersed in buffered oxide etchant (BOE) in an ultrasonic bath to etch the glass. After etching, the remaining photoresist was removed with ethanol. PDMS was then poured over the glass masters and cured. The elastomeric molds were carefully peeled off, washed with ethanol and purified water, and dried under a stream of nitrogen. In the penultimate step, the molds were treated in an oxygen plasma for 30 s along with clean planar borosilicate glass substrates. It should be noted that the borosilicate substrates were cleaned in a boiling 1:3 solution of ICN x7 detergent and purified water. Then the substrates were rinsed with copious amounts of purified water, dried with nitrogen, and annealed in a kiln at 480 °C for 5 hours before introduction into the oxygen plasma. Finally, the PDMS molds and glass substrates were brought into contact immediately after oxygen plasma treatment to create finished microfluidic devices.

Preparation of Small Unilamellar Vesicles and Bilayer Formation Small unilamellar vesicles (SUVs) were prepared by vesicle extrusion.[15,47,48] Lipids dissolved in chloroform were dried under a stream of nitrogen followed by overnight vacuum desiccation. Next, the lipids were rehydrated in PBS buffer (pH 7.2). After five freeze-thaw cycles, the vesicles were extruded more than seven times through a polycarbonate filter (Whatman) containing 50 nm pores. SUVs prepared by this method were 70 ± 10 nm in diameter as determined by dynamic light scattering with a Brookhaven Instruments 90Plus Particle Size Analyzer.

For bilayer formation, 5 µL of a 2.5 mg/mL SUV solution were injected through each inlet port of the linear array microfluidic device. The solution was introduced immediately after plasma treatment and bonding of the PDMS/glass microfluidic platform to insure that the surfaces remained hydrophilic. Vesicle fusion occurred on both the PDMS walls and the glass substrate to form a continuous lipid bilayer coating as has been previously reported.[17] The incubation time for bilayer formation was 1 h. The microchannels were rinsed with PBS buffer to remove excess vesicles. Fluorescence recovery after photobleaching (FRAP)[125,126] was employed to verify the quality of the supported bilayers on the glass surfaces from which all binding data were obtained.

All solid-supported membranes were made from the fusion of POPC vesicles containing a series of GM_1 concentrations from 0 to 10.0 mol%. The distribution of GM_1 between the upper and lower leaflets of the supported bilayers was tested and found to be the same within experimental error using methods developed by Parikh and coworkers.[127] Before the injection of protein solution, the bilayer-coated microchannels were incubated with a 0.5 mg/mL Rabbit IgG antibody solution for 30 minutes to block defect sites in the membrane and thereby suppress non-specific adsorption of CTB.

Epifluorescence Microscopy and TIRFM To check the quality and fluidity of supported GM_1/POPC bilayers, FRAP studies were conducted using an inverted epifluorescence Nikon Eclipse TE2000-U microscope with a 10× objective. Laser radiation from a 2.5 W mixed gas Ar^+/K^+ laser (Stabilite 2018, Spectra Physics) was used to bleach the lipid bilayer samples. FRAP images were obtained with a MicroMax 1024b CCD camera (Princeton Instruments). Total internal reflection fluorescence microscopy (TIRFM),[128,129] which can discriminate between dye-labeled CTB molecules bound to the supported membrane and those in the bulk solution, was employed for the determination of binding isotherms. In this case the fluorescence images were obtained with a Nikon E800 fluorescence microscope using a 4× objective. In the TIRFM experiments, a 594 nm Helium-Neon laser beam (4 mW, Uniphase, Manteca, CA) was passed through a dove prism that was optically coupled to the bottom of the borosilicate substrate of the microfluidic device by index matching immersion oil. Alexa 594-labeled CTB solutions were simultaneously flowed through each channel at various concentrations at a rate of 0.2 μL/min by a Harvard PHD 2000 syringe pump (Harvard Apparatus, Holliston, MA). The Helium-Neon laser beam was telescoped out by a line generator lens (BK7 for 30°, Edmund Optics, Barrington, NJ) to create a uniform intensity profile across the microchannel array. As the laser illuminated the interface between the bilayer-coated glass substrate and the bulk aqueous solution, it was totally internally reflected, creating an evanescent wave above the interface. The evanescent wave decayed exponentially to its 1/e value by ~ 70 nm above the interface under the experiment conditions employed here.[15,130] This allowed the proteins bound to the supported lipid bilayer to be studied with high specificity. The TIRFM images were captured with a Micromax 1024b CCD camera, collected using Metamorph software (Universal Imaging Corp.), and transferred to Sigma Plot for further processing.

Atomic Force Microscopy AFM images of supported lipid bilayers were acquired with a Nanoscope IIIa Multimode SPM (Digital Instruments, Santa Barbara, CA) equipped with a J-type scanner. POPC bilayers samples were probed with 0.0 mol%, 0.1 mol%, 0.5 mol%, 1.0 mol%, 3.0 mol%, 5.0 mol%, and 10.0 mol% GM_1. The experimental conditions were identical to those used in the microfluidic devices except for the fact that the PDMS mold above the glass surface was absent. Instead, the bilayer coated borosilicate glass served as the bottom of a standard AFM liquid sample cell. All images were obtained in fluid contact mode at a scan rate of 2.0 Hz using oxide-sharpened DNP-S1 silicon nitride probes (spring constant: 0.06 N/m; Veeco Probes, Santa Barbara, CA). The only treatment applied to the images was flattening. GM_1

domains were judged to be present on the POPC bilayer surface when the feature height exceeded 1.0 nm above the membrane background. In this case, the nominal width of a domain was taken from the point where the feature height first began to rise above the background level and ended when it returned to background level. To abstract more quantitative information on the GM_1 cluster size, a standard deconvolution method was employed.[131,132] For this purpose a nominal AFM tip radius of 10 nm was assumed (according to the manufacturer's specifications) and a headgroup height of 1.0 nm for the GM_1 features was also employed. Under these conditions, the size of the GM_1 clusters, which had nominal mean diameters between 16.1 and 28.3 nm, were reduced by 8.8 nm to take tip-sample convolution effects into account.

Results

A schematic representation of the lipid coated PDMS microchannels bonded to a planar glass support is shown in Figure 2.2a. GM_1/POPC bilayers were coated over the entire surface (shown in green). The surface binding process was monitored by TIRFM as a function of time until the fluorescence intensity remained constant. A typical TIRF image is shown in Figure 2.2b. In this case the bulk CTB concentration ranged from 6.0 nM to 0.090 nM (left to right). Control experiments were conducted under the same conditions without GM_1 in the POPC membrane. Under these conditions, virtually no background fluorescence signal was observed, as the bulk protein concentrations were so low.[115,118] Intensity profiles across the TIRF image (dotted red line in Figure 2.2b) were employed to obtain quantitative binding data.

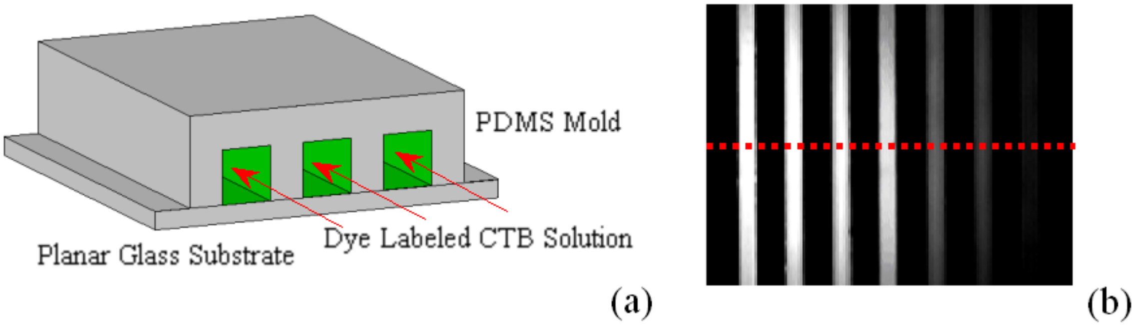

Figure 2.2. (a) Schematic representation of bilayer-coated PDMS/glass microchannels. (b) TIRF image of a bilayer-coated microchannel array containing various concentrations of dye-labeled CTB.

In a first set of experiments, solid supported POPC bilayers containing 0.05, 0.5, and 5.0 mol% GM_1 were prepared in separate parallel arrays of microfluidic channels and tested for CTB binding (Figure 2.3). In order to abstract equilibrium dissociation constants, the CTB-GM_1 binding curves were fit to both the Langmuir isotherm (eqn. 2) and Hill-Waud (eqn. 3) binding models:[122]

$$F = F_{\max} \times \frac{[P]}{K_d + [P]} \tag{2}$$

$$F = F_{\max} \times \frac{([P])^n}{(K_H)^n + ([P])^n} \tag{3}$$

where F is the fluorescence intensity from surface bound proteins, F_{max} is the maximum fluorescence intensity when proteins completely saturate the bilayer surface, $[P]$ is the bulk CTB concentration, K_d and K_H are the apparent equilibrium dissociation constants for the respective models, and n is the Hill coefficient of cooperativity.[122] The Langmuir isotherm model[32,133] is valid for pentavalent CTB binding to multiple ligands on the surface so long as the individual binding events are independent.[112,114,119] On the other hand, the Hill-Waud model takes into account binding cooperativity by introducing the Hill coefficient, n.[94,122] The Langmuir isotherm fit became progressively poorer as the concentration of surface bound ligands was increased. In fact, the Hill-Waud model (regression coefficient, $R^2 = 0.99$) more closely fit the CTB binding data in comparison to the Langmuir adsorption isotherm ($R^2 = 0.96$) at the highest glycolipid concentration. The apparent dissociation constants K_d (0.69 ± 0.11 nM) and K_H (0.50 ± 0.07 nM) were also somewhat different under these circumstances.

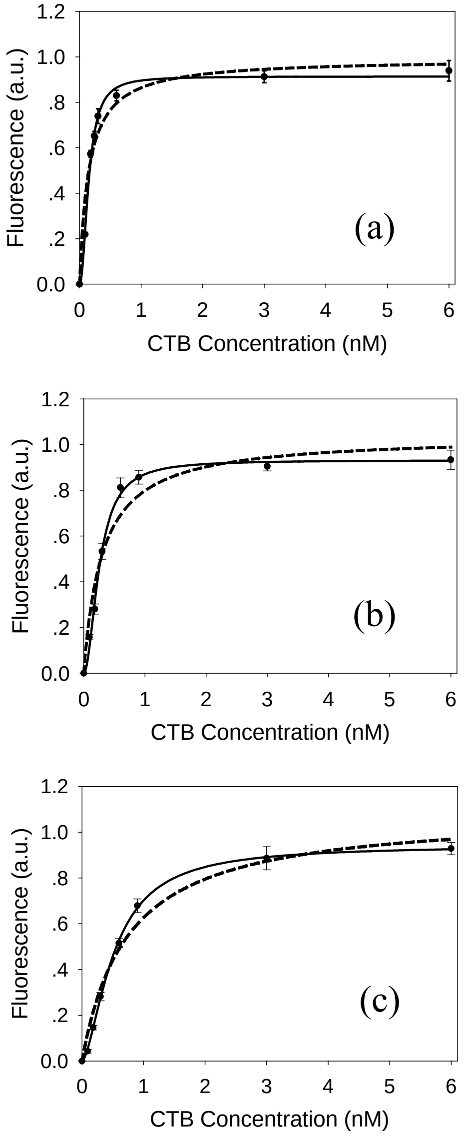

Figure 2.3. TIRF intensity of surface-bound CTB vs. bulk protein concentration at three different GM_1 densities in POPC bilayers: (a) 0.05 mol%, (b) 0.5 mol%, and (c) 5.0 mol%. The dashed curves were fits to a Langmuir adsorption isotherm while the solid curves were fits to the Hill-Waud model.

Table 2.1. CTB-GM_1 binding constant as a function of ligand density.

Conc. of GM_1 (mol%) in POPC Bilayers	K_d (nM)	K_H (nM)	n
0.02	0.11 ± 0.07	0.11 ± 0.05	1.3
0.05	0.16 ± 0.05	0.15 ± 0.03	1.6
0.1	0.23 ± 0.10	0.17 ± 0.06	1.5
0.5	0.32 ± 0.07	0.26 ± 0.04	1.8
1.0	0.39 ± 0.08	0.31 ± 0.05	1.9
2.0	0.46 ± 0.15	0.37 ± 0.10	1.9
5.0	0.69 ± 0.11	0.50 ± 0.07	2.0
10.0	0.86 ± 0.09	0.59 ± 0.05	2.0

Similar experiments to those shown in Figure 2.3 were performed at eight GM_1 concentrations ranging from 0.02 to 10.0 mol% in POPC bilayers. The fits to the Hill-Waud and Langmuir binding models are provided in Table 2.1. As can be seen, as the GM_1 density was increased, the Hill coefficient, n, deviated ever further from 1.0 and K_H became significantly different from K_d. At the lowest GM_1 density, however, K_d and K_H were indistinguishable within experimental error and the Hill coefficient approached 1.0. This suggests that CTB binds cooperatively to GM_1 at high ligand densities. Such a finding is in agreement with previous observations.[94,108,109,122] More significantly, the apparent equilibrium dissociation constant continuously weakened with increasing ligand density.

The K_H values as a function of GM_1 concentration in the POPC bilayer from Table 2.1 are plotted in Figure 2.4. As can be seen, the data do not show a linear trend as a function of ligand density. Rather, the apparent dissociation constant weakens more sharply as a function of concentration at low GM_1 concentrations, but begins to level out at higher concentrations. The curve shape is reminiscent of a binding isotherm. Two possible origins for this phenomenon need to be considered. First, one might hypothesize that the weakening of the binding could be caused by clustering of the GM_1 lipids. Alternatively, weakening of K_H might be the result of electrostatic repulsion between the negatively charged CTB and the increasingly negatively charged membrane as the ligand density is increased (note: each GM_1 headgroup has a charge of -1).[111]

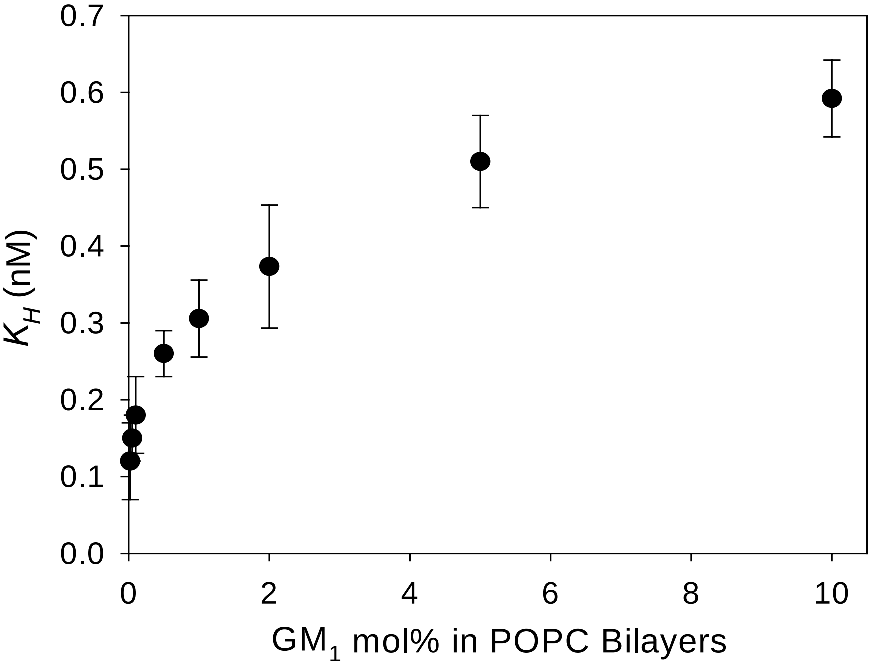

Figure 2.4. K_H vs. the concentration of GM$_1$ in the POPC bilayers for CTB-GM$_1$ binding.

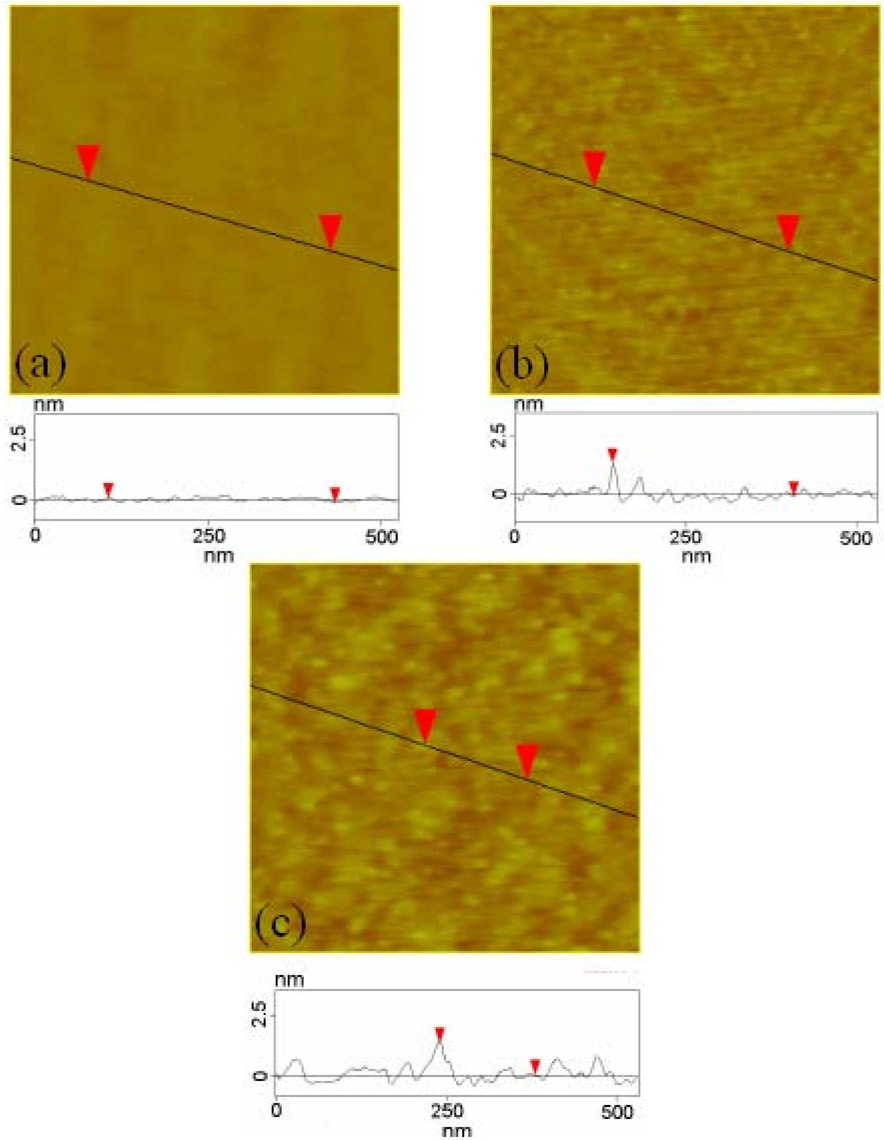

Figure 2.5. AFM images of GM_1 clustering on POPC bilayers: (a) a pure POPC bilayer, (b) a POPC bilayer containing 0.5 mol% GM_1, and (c) a POPC bilayer containing 5.0 mol% GM_1. Each image is 500 nm × 500 nm.

To investigate GM_1 clustering, AFM experiments were performed as a function of GM_1 concentration in supported POPC bilayers in the absence of CTB. A pure POPC membrane was imaged first as a control (Figure 2.5a). As expected, the membrane looked relatively flat and featureless. By contrast, systems containing 0.5 mol% GM_1 (Figure 2.5b) and 5.0 mol% GM_1 (Figure 2.5c) contained 1.0 ~ 2.0 nm high features which are consistent with the presence of GM_1.[134] In fact, the height of the GM_1 pentasacchride headgroup has been measured by X-ray diffraction and is consistent with this finding.[135,136] POPC bilayers containing 0.1 mol%, 1.0 mol%, 3.0 mol%, and 10.0 mol% GM_1 were also imaged by AFM. The apparent size of the domains in these images ranged from approximately 15 to 60 nm. Consistent with expectations, these domains were more prevalent at high GM_1 density (e.g. 5.0 mol%) than at low density (e.g. 0.5 mol%).

To quantify the domain size distribution in the POPC bilayers, the approximate diameter of the GM_1 domains were measured and counted from four independent 500 nm × 500 nm AFM micrographs at each ligand density. Histograms for the number of GM_1 domains as a function of apparent cluster size at GM_1 densities between 0.1 mol% and 10.0 mol% are provided in Figure 2.6. As can be seen from Figures 2.5 and 2.6, GM_1 clustering within the POPC bilayers became more pronounced at increased GM_1 densities. The mean domain size after deconvolution at 0.5 mol% was 11.0 nm and this value rose to 18.6 nm for 5.0 mol% GM_1. In fact, the mean domain size continually

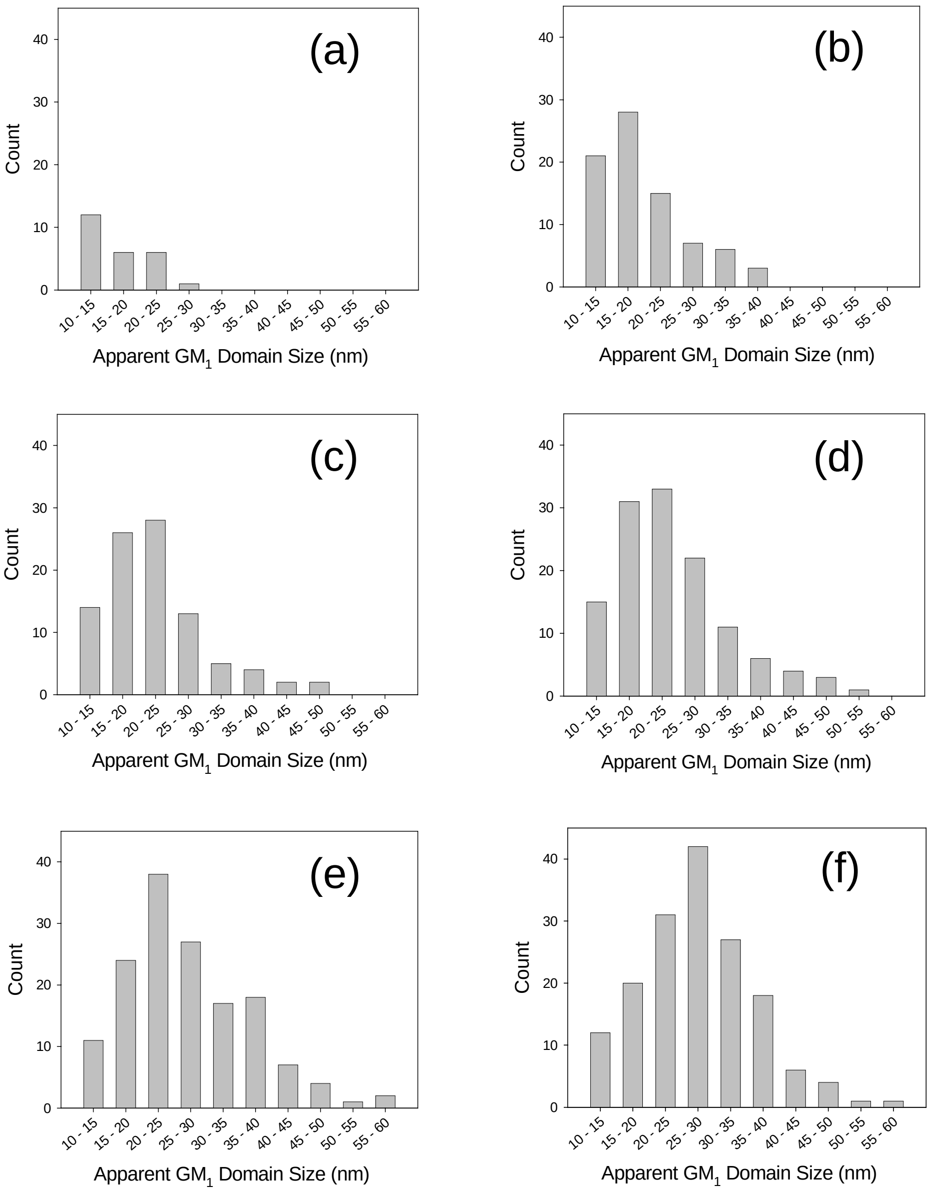

Figure 2.6. Histograms for the distribution of GM_1 domains within POPC bilayers: (a) 0.1 mol%, (b) 0.5 mol%, (c) 1.0 mol%, (d) 3.0 mol%, (e) 5.0 mol%, and (f) 10.0 mol% GM_1/POPC.

Table 2.2. GM_1 domain size as a function of ligand density.

GM_1 mol%	Calc. GM_1 surface conc. (nmol/dm^2)	Apparent mean size (nm)	Mean size after deconvolution (nm)
10.0	2.37	28.3	19.5
5.0	1.19	27.4	18.6
3.0	0.71	24.1	15.3
1.0	0.24	22.4	13.6
0.5	0.12	19.8	11.0
0.1	0.024	16.1	7.3

shifted from ~ 7 nm to ~ 20 nm as the GM_1 density was increased from 0.1 mol% to 10.0 mol% (Table 2.2).

To further elucidate the binding mechanism as a function of ligand density, the shape of the K_H vs. GM_1 ligand density curve shown in Figure 2.4 needs to be considered. As mentioned above, the curve shape is reminiscent of a binding isotherm. Treating the curve in this manner requires that the y-axis be considered in a fashion analogous to a fractional coverage of available sites. This was achieved by fitting the data in Figure 2.4 to a binding isotherm equation, $y = y_0 + y_{max}x/(b+x)$, to obtain the y intercept (y_0 at $x = 0$) and the maximum value (y_{max} at $x = \infty$). By offsetting y_0 to 0 and normalizing y_{max} to equal 1, the y-axis essentially becomes analogous to a surface coverage. On the other hand, the x-axis must be treated as a two dimensional concentration. This can be done by noting that 1.0 mol% GM_1 is equivalent to a number density of 0.237 nmol/dm^2 (assuming an average area per POPC lipid of ~ 0.7 nm^2).[137] Number density units of square decimeters rather than square meters are employed in analogy to molar units which are moles/dm^3. Doing this produces an equation in the form:

$$f = \frac{[L]_s}{B_s + [L]_s} \tag{4}$$

where f is a unitless fraction which ranges from 0 to 1. $[L]_s$ is the two-dimensional number density of the glycolipid. The subscript, s, is used to denote the fact that this is a surface concentration. B_s is the apparent two-dimensional dissociation constant which

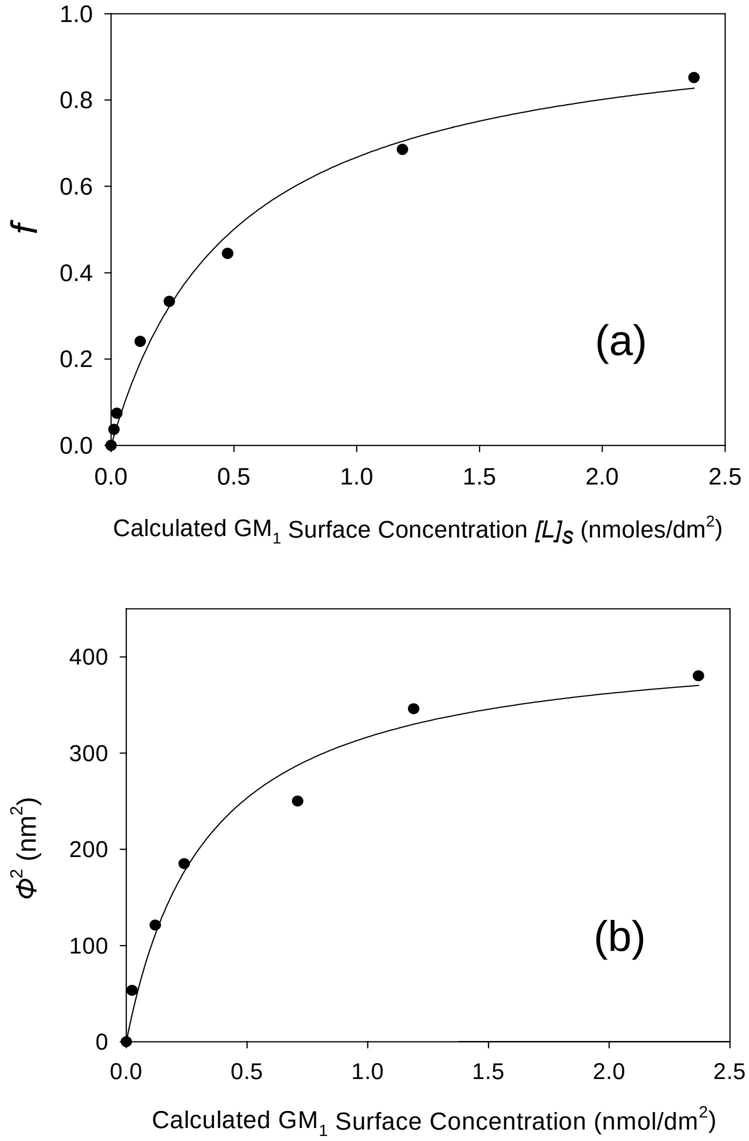

Figure 2.7. Fitted plots of (a) f and (b) the square of characteristic domain size, (Φ^2), vs. the GM_1 surface concentration in POPC membranes.

also has units of moles/dm^2. The value of f approaches zero if all of the glycolipids are separated from one another and reaches 1.0 when they are completely clustered. A fit to the data is shown in Figure 2.7a. The abstracted parameter, B_s = 0.50 nmol/dm^2, is a remarkably good fit to the data (R^2 = 0.99). This would imply that half of the ganglioside molecules are clustered at 2.1 mol% GM_1 in the POPC membrane.

The abstracted value of B_s for GM_1 clustering should be compared with the AFM data in Table 2.2. To do this, the square of the mean domain diameter, Φ^2, is plotted as a function of GM_1 density in Figure 2.7b. Φ^2 was chosen instead of Φ because it is proportional to the area of the GM_1 domains and, hence, to the number of glycolipids. By fitting the domain area data to a Langmuir isotherm, a nominal equilibrium dissociation constant for GM_1 clustering on the POPC bilayer can nominally be extracted. The result gives an apparent value of K_d = ~ 1.4 mol% GM_1 for the AFM data, which is a rather close match to the results in Figure 2.7a. This is strong evidence that GM_1 clustering is correlated to the observed weakening of the equilibrium dissociation constant for CTB-GM_1 as a function of glycolipid density.

Although, the clustering hypothesis is consistent with the AFM results, an electrostatic repulsion hypothesis was also considered to explain the data in Figure 2.4. It should be noted, however, that an electrostatic effect seems implausible on several other grounds. First, electrostatic repulsion between the negatively charged GM_1 glycolipids and the CTB proteins would probably not be expected to show the type of saturation behavior found in Figure 2.4. Moreover, the Debye length is already rather short at the lower salt concentration employed in these experiments (~ 0.8 nm for 150 mM NaCl).[138] This means that an incoming CTB molecule should not experience significant electrostatic repulsion from the charge on the membrane.

Nevertheless, we wished to test the electrostatic hypothesis. To do this, we monitored CTB binding in the presence of PBS buffer with a higher NaCl concentration (300 mM). Under these conditions one might expect the apparent dissociation constant to tighten if electrostatic repulsion were playing a significant role in the effects observed in Figure 2.4. Our results, however, showed no evidence for a change in the binding constant at higher salt concentration. This was true even when 10.0 mol% GM_1 was present in the membrane. In fact, K_H was measured to be 0.62 nM for 10.0 mol% GM_1 in the presence of 300 mM NaCl. This value is identical within experimental error to the value obtained in Table 2.1 with 150 mM NaCl (0.59 nM). Illustrative data are shown in Figure 2.8. This plot shows the line profile of the fluorescence intensity across a seven-channel microfluidic device containing POPC membranes with 10.0 mol% GM_1. The first three channels show data at various concentrations of CTB in the presence of PBS buffer with 300 mM NaCl, while the last three channels are for the identical conditions, but employing buffer with 150 mM NaCl. As can be seen, the fluorescence intensities are virtually unaffected by the increase in salt.

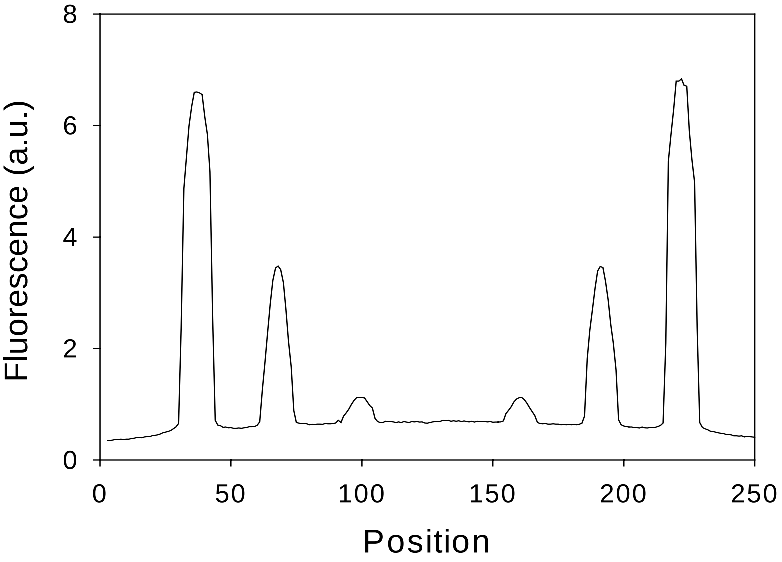

Figure 2.8. Line profile of the TIRF intensity across a seven-channel, bilayer-coated microfluidic device containing 10.0 mol% GM_1. 6.0 nM, 0.6 nM, and 0.12 nM CTB solutions containing 300 mM NaCl were flowed through the first three channels, respectively. Similar samples in the reverse order with 150 mM NaCl were flowed through the last three channels. The channel in the middle was filled with PBS buffer and used as a reference for determining the background level.

Discussion

The effect of ligand density on CTB-GM_1 binding presented here is opposite to that which would be predicted by a simple non-cooperative sequential binding model (eqn. 1). In the absence of interacting ligands, steric/allosteric effects, or other related phenomena, one would expect that increasing ligand density at the membrane interface would strengthen ligand-receptor binding as was previously found in the case of antibody-antigen interactions.[16] Herein, however, increased GM_1 density in the phospholipid membrane actually led to a weakening of the apparent equilibrium binding constant. This effect is almost certainly caused by interactions between the ganglioside molecules, which induced GM_1 clustering on the solid-supported phospholipid membranes.

The crystal structure of the CT-GM_1 binding complex has been investigated by Merritt[139] and isothermal titration calorimetry investigations have been performed by Turnbull.[140] These studies show that the binding site specificity of cholera toxin for GM_1 arises from recognition of the sialic acid, terminal galactose, and *N*-acetylgalactosamine moieties. Specifically, the majority of CTB-GM_1 interactions involve hydrogen bonds to the sugar hydroxyl groups. The clustering found in our AFM images suggests that at least some of these moieties may be involved in hydrogen bond formation with neighboring GM_1 molecules. This idea is further supported by EPR experiments of GM_1 in phospholipid membranes, which indicated that the oligosaccharide head group is capable of forming intermolecular H-bonds.[141] Hydrogen bonding between membrane bound GM_1 molecules in model membranes has also been suggested on the basis of freeze-etch electron microscopy.[142] In the present experiments, such lateral interactions should effectively compete with the binding of the CTB proteins. Moreover, the crowding of the GM_1 molecules may limit CTB binding on steric grounds. The putative mechanism for these effects is presented in Figure 2.1.

It is interesting to note that previous studies have concluded that GM_1 enriched lipid raft domains are needed to ensure maximal binding of CT to the cell surface.[143,144] Wolf et al.[145] proposed that toxin-induced signal transduction depends on the coupling of CT with GM_1 enriched caveolae or caveolae-like membrane domains. No results to date, however, have shown stronger binding of CT to GM_1 enriched raft domains. The results in this chapter indicate that GM_1 domain clustering may not strengthen toxin-ligand interactions. Rather, higher GM_1 concentrations would simply lead to greater number densities of toxin molecules bound in these locations. It should be noted, however, that cell membranes typically included other lipids such as sphingolipids and cholesterol which could possibly play a role in GM_1 presentation and, hence, in the thermodynamics of cholera toxin binding.

Conclusion

Systematic studies of multivalent CTB-GM_1 interactions in Chpater II were undertaken as a function of ligand density by using a microfluidic strategy in conjunction with TIRFM. CTB bound more weakly at higher ligand densities and this observation was ascribed to the clustering of GM_1 in the phospholipid bilayer. AFM results supported this hypothesis. Furthermore, characteristic equilibrium dissociation constant measurements for GM_1 clustering on solid-supported phospholipid membranes were determined.

CHAPTER III

MULTIPLE MULTIVALENT LIGAND-RECEPTOR INTERACTIONS MEASUREMENT WITHIN ONE-SHOT BINDING EXPERIMENTS

Introduction

Multivalent ligand-receptor interactions are ubiquitous on cell surfaces. They have a wide variety of consequences including enhanced binding, greater receptor selectivity, and receptor clustering.[97] They can also play a direct role in signal transduction processes.[146] Examination of the underlying thermodynamics of multivalency may lead to a greater understanding of its biological role and could provide insight into biomedical applications involving inhibitory drug design.[97,99,104] Unfortunately, high-throughput, low protein consumption assays are not presently well enough developed in this field to afford rapid, accurate systematic studies of ligand-receptor binding at membrane interfaces in a systematic fashion.[16]

In previous work our laboratory demonstrated that microfluidic devices can be designed for measuring binding affinities in multivalent systems at lipid membrane interfaces.[15,16,34,92-94] In our setup, ligands were incorporated into supported lipid bilayers (SLBs) coated on the walls and floors of polydimethylsiloxane/glass microchannels. Linear arrays of channels were then monitored by total internal reflection fluorescence microscopy (TIRFM)[128] to obtain equilibrium dissociation constants in one-shot assays. This could be done by using the same surface chemistry in each microchannel while varying the solution concentration of the aqueous proteins.

This made these assays more rapid, afforded high accuracy, and used only a few microliters of protein solution. Nevertheless, these assays could still be improved considerably by measuring multiple binding constants for various membrane chemistries simultaneously. This could be done by employing a variety of different lipid bilayer chemistries in each microfluidic channel while still arraying the solution concentration of the aqueous protein over the entire array. This would essentially amount to a two-dimensional assay whereby both the surface chemistry and aqueous solutions are varied on a single chip. Such assays would be extremely useful for probing multivalent binding as a function of ligand density, cholesterol content, membrane charge, etc. in one-shot experiments. Such designs are also reminiscent of other on-chip two-dimensional assays.[147-149]

The key to achieving two-dimensional binding assay is to create spatially addressed arrays of bilayers inside individual microchannels. There have already been a number of techniques developed to array different bilayer chemistries at each address. For example, we first showed the use of pulled microcapillaries to deliver unique vesicle solutions to an array of hydrophilic patches arrayed on a substrate with hydrophobic barriers.[18] Subsequently, other methods for creating spatially addressed bilayer arrays have been developed. These include microcontact printing,[73-75] laminar flow vesicle deposition,[84] mechanical erasing and writing,[70] robotic pin printing,[78] scanning probe lithography,[85] and dip-pen nanolithography.[82] Although each of these techniques has its merits, it would be most convenient to develop a procedure that allows bilayers to be arrayed inside enclosed microchannels with a well characterized and predetermined chemistry at each location. The most attractive way of obtaining such a result will be to develop a light directed patterning method analogous to the ones we have already developed for arraying immobilized ligands inside microfluidic devices.[150]

Pioneering work has been done by the Parikh laboratory to pattern solid supported lipid bilayer using deep UV radiation.[79,80,127,151] Additional with UV radiation had been undertaken to pattern organosilane monolayers[152,153], polysaccharides,[54] and S-layer proteins.[154] Chapter III extends this idea to patterning sacrificial adsorbed protein layers at the liquid/solid interface. We show it is possible to deposit films made from bovine serum albumin (BSA), immunoglobulins, and fibrinogen. Areas containing the protein layer resist the fusion of vesicles to form fluid lipid bilayers, while irradiated regions allow bilayers to form. We exploited this ability to pattern linear arrays of phospholipid membranes containing four different concentrations of ganglioside GM_1 (Figure 3.1). Each channel in a seven-channel device contained the same four membranes. At this point, a unique concentration of cholera toxin B subunits (CTB) was flowed into each channel to yield 28 simultaneously data points for the CTB-GM_1 binding pair. This afforded multiple equilibrium dissociation constants for ligand-receptor binding on fluid phospholipid membranes.

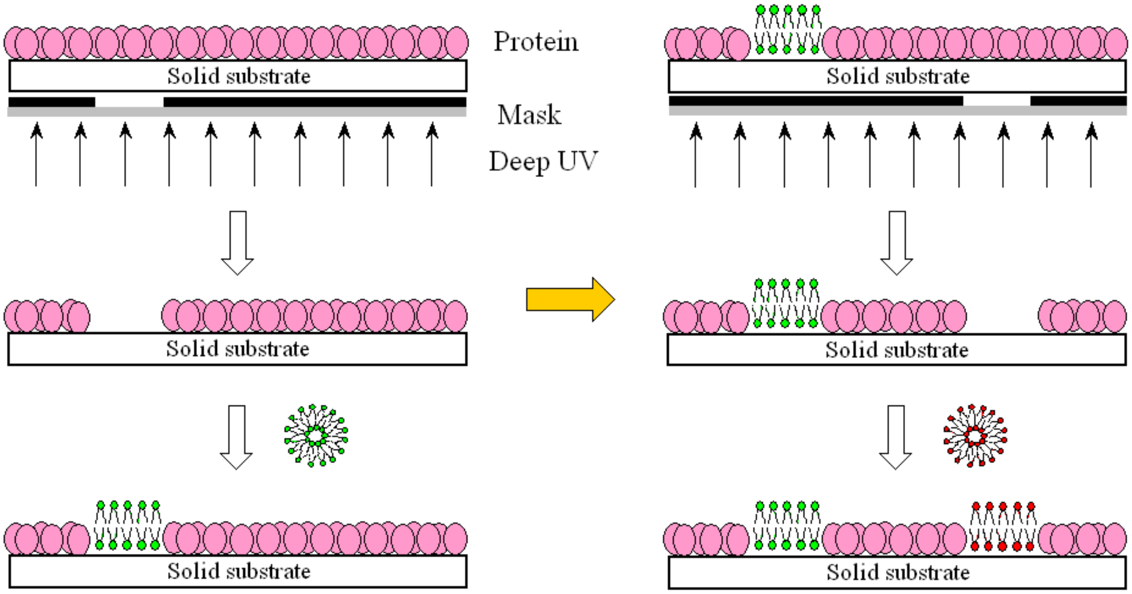

Figure 3.1. Schematic representation of the general process steps for creating spatially addressed bilayer arrays. A sacrificial protein monolayer was patterned in a single microchip or individual microfluidic channels by deep UV radiation. SLBs were formed by vesicle fusion. The solid substrate is 0.2 mm thick quartz.

Experimental

Materials Bovine serum albumin (BSA), Texas Red conjugated BSA, Rabbit IgG, and Texas Red-labeled 1,2-dihexadecanoyl-*sn*-glycero-3-phosphoethanolamine, triethylammonium salt (TR-DHPE) were purchased from Molecular Probes, Inc. (Eugene, OR). Fibrinogen from human plasma and CTB from *Vibrio cholerae* were obtained from Sigma-Aldrich. Ganglioside GM_1 (Brain, Ovine-Ammonium Salt), 1-palmitoyl-2-oleoyl-sn-glycero-3-phosphocholine (POPC), and 1,2-Dipalmitoyl-sn-Glycero-3-phosphoethanolamine-N-(7-nitro-2-1,3-benzoxadiazol-4-yl) (Ammonium Salt) (NBD-PE) were purchased from Avanti Polar Lipids (Alabaster, AL). CTB was labeled with Alexa Fluor-594 dye using a standard protein-labeling kit (A10239, Molecular Probes, Eugene, OR). The degree of labeling was about 0.8 fluorophores per protein as determined by UV/Vis absorption spectroscopy. The dye-labeled protein was stored in PBS buffer solution containing 10 mM sodium phosphate, 150 mM NaCl, and 0.2 mM sodium azide. The pH of the PBS was set to 7.2 by dropwise addition of 2.0 M NaOH. The PBS buffer was also used for vesicle preparation and the successive dilution of protein solutions. Purified water for these experiments came from a NANOpure Ultrapure Water System ($\geq$18.2 MΩ·cm, Barnstead, Dubuque, IA). Quartz coverslips (1×1 inch, 0.2 mm thick, Electron Microscopy Sciences, Hatfield, PA) were used as substrates for lipid bilayer formation. Electron Microscope grids (EM-grids, Gilder Grids from Electron Microscopy Sciences, Hatfield, PA) were employed as photomasks in deep UV lithography.

Small Unilamellar Vesicles Preparation Small unilamellar vesicles (SUVs) was prepared by vesicle extrusion as reported previously.[15,47,48] Briefly, lipids dissolved in chloroform were dried under a stream of nitrogen followed by vacuum desiccation for 4 hours. The lipids were then rehydrated in PBS buffer. The concentration of lipids in solution was 2.0 mg/mL. After five freeze-thaw cycles the vesicles were extruded more than seven times through a polycarbonate filter (Whatman) with 50 nm pores. SUVs prepared by this method were characterized by dynamic light scattering (90Plus particle size analyzer, Brookhaven Instruments Corp.) and showed a size of 70 ± 10 nm in diameter. Sample vesicles include pure POPC, TR-DHPE/POPC mixtures with 0.5 - 0.05 mol% TR-DHPE, NBD-PE/POPC mixtures with 2 mol% and 0.5 mol% NBD-PE, and GM_1/POPC mixtures containing 0.2 mol%, 0.5 mol%, and 2.0 mol% GM_1, respectively.

Microfluidic Device Fabrication The seven-channel microfluidic devices were fabricated as described previously.[34] The only difference is that we used 0.2 mm thick quartz substrate, instead of borosilicate glass. Basically, we fabricated the seven-channel geometry pattern on cleaned soda lime microscope slides by photolithography and buffered oxide etchant (BOE) etching. Degassed PDMS was then poured over the glass master and cured in a convection oven at 55 °C overnight. The elastomeric mold was carefully peeled off, washed with ethanol and purified water, and dried under a stream of nitrogen. Inlets were reamed at the channel termini using a hollow flat-tipped syringe needle. Finally, the PDMS mold and a clean planar quartz coverslip were treated in an oxygen plasma for 30 s. The two were brought immediately into contact to create the finished microfluidic device. It should be noted that the quartz substrate was cleaned in a boiling 1:3 solution of ICN x7 detergent and purified water. It was then rinsed with copious amounts of purified water, dried with nitrogen, and annealed in a kiln at 500 °C for 5 hours before use.

Epifluorescence and TIRF Microscopy Epifluorescence images of protein patterns and SLBs were obtained using a Nikon E800 fluorescence microscope with a Roper Scientific Micromax CCD camera. To check the quality and fluidity of the SLBs, Fluorescence Recovery after Photobleaching (FRAP)[125,126] experiments were conducted using an inverted epifluorescence Nikon Eclipse TE2000-U microscope with a 10× objective. Laser radiation from a 2.5 W mixed gas Ar^+/K^+ laser (Stabilite 2018, Spectra Physics) was used to bleach the lipid bilayer samples. FRAP images were obtained with a MicroMax 1024b CCD camera (Princeton Instruments). Total internal reflection fluorescence (TIRF) microscopy[128] was employed in CTB-GM_1 binding studies as a function of ligand density. In the TIRF microscopy experiments, a 594 nm Helium-Neon laser beam (4 mW, Uniphase, Manteca, CA) was passed through a dove prism that was optically coupled to the quartz substrate of the microfluidic device by index matching immersion oil. The laser beam was telescoped out by a line generator lens (BK7 for 30°, Edmund Optics, Barrington, NJ) to create a uniform intensity profile across the microchannel array. As the laser illuminated the interface between the quartz substrate and the bilayer, it was internally reflected, creating an evanescent wave above the interface. The evanescent wave decayed exponentially to its 1/e value by ~ 70 nm from the interface under the experiment conditions employed here.[15,130] This allowed the proteins bound to the SLBs to be studied with high specificity. All images were collected using Metamorph software (Universal Imaging Corp.) and transferred to Microsoft Excel and Sigma Plot for further processing.

Results

In a first set of experiments, we wished to test the use of a bovine serum albumin (BSA) as a sacrificial protein monolayer in deep UV patterning experiments. To this end, a 10 mg/mL solution of BSA was introduced above a quartz surface and allowed to incubate for 20 min. This should form a continuous monolayer of BSA at the interface.[155] Excess proteins were washed away with copious amounts of purified water. The protein was conjugated with a Texas Red fluorophore so that it could be visualized under a fluorescence microscope. Electron Microscope grids (EM-grids) were exploited as a photomask for photopatterning. Deep UV radiation was produced by a mercury Pen-Ray lamp (UVP Inc., Upland, CA) in a quartz envelope. The protein-coated substrate was placed ~ 3 mm under the UV light source. The BSA monolayer could be either under water or exposed to air. ~ 2.8 W of radiation with wavelengths of ~ 190 nm and ~ 254 nm was introduced to the sample surface through a photomask for 2 min. The surface was then washed with copious amounts of D.I. water.

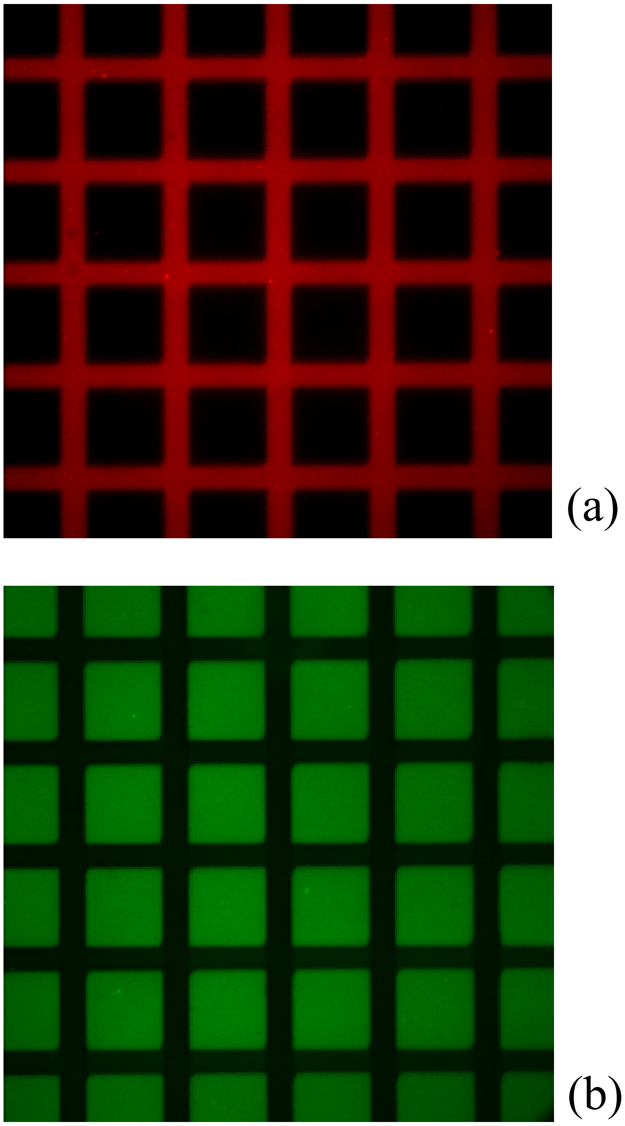

Figure 3.2. (a) Epifluorescence image of Texas Red-conjugated BSA protein pattern. (b) Epifluorescence image of POPC bilayer containing 2.0 mol% NBD-PE formed over deep UV exposed regions.

Figure 3.2a shows the resultant pattern formed on the substrate. Specifically, ~ 90 × 90 μm voids were created which were separated by ~ 35 μm protein bars. This was identical to the dimensions of the 200 mesh EM-grid used to make the pattern. At this point, POPC vesicle solutions containing 2 mol% NBD-PE/POPC were introduced above the patterned surface and allowed to form bilayers by the vesicle fusion method.[9] This led to the creation of patterned POPC membranes separated by BSA barriers (Figure 3.2b). The high contrast epifluorescence image consisting of green lipid bilayers and dark bars demonstrates that SLBs were confined in the protein corrals.[156] The two-dimensional fluidity of the bilayer microarray was confirmed by the fluorescence recovery after photobleaching technique[125,126] (Figure 3.3). The diffusion constant for the NBD-PE lipid was 3.4 ± 0.8 $\mu m^2/s$ and the mobile fraction was ~ 97%.

Next, it was necessary to demonstrate that this method could be used as a sequential patterning technique. The ability of the present method for spatial addressing a bilayer array with different lipid components was created in a single microchip or individual microchannels. The general steps were illustrated in Figure 3.1. Basically, after deep UV illumination through a single slot EM-grid photomask (hole size: ~ 100 μm), BSA under light exposure was selectively removed to form a round vacancy on the substrate. A supported lipid bilayer was then addressed over the light exposed region through vesicle fusion. In the second step, the photomask is manually aligned to another unexposed protein region. Repeating the erasing and addressing step, second supported lipid bilayer was deposited into the new vacancy. Multiple distinct lipid components can

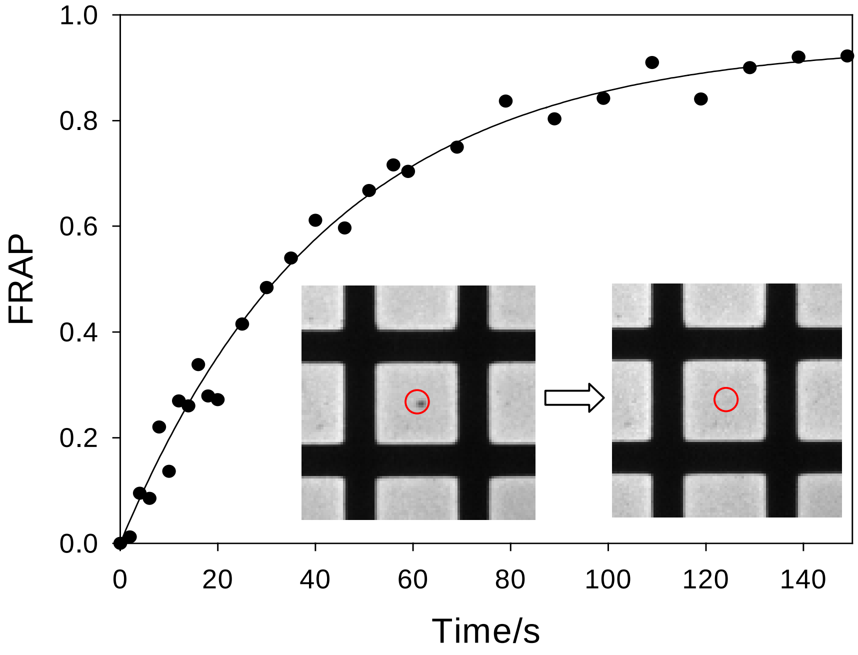

Figure 3.3. FRAP recovery curve for 0.1 mol% TR-DHPE/POPC bilayer on a planar borosilicate substrate. Inset is the fluorescence images right after photobleaching and after recovery.

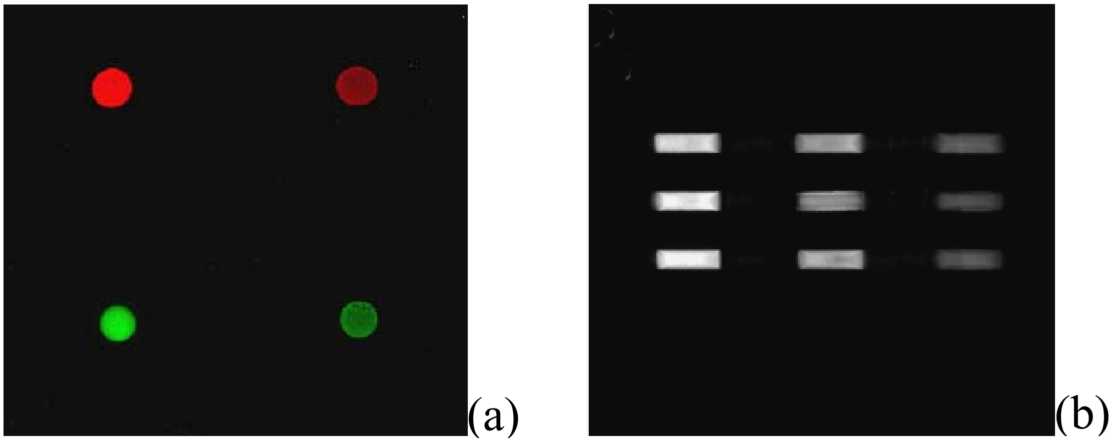

Figure 3.4. (a) Epifuorescence image of a single microchip containing various lipid compositions (top left: 0.5 mol% TR-DHPE/POPC, top right: 0.1 mol% TR-DHPE/POPC, bottom left: 2.0 mol% NBD-PE/POPC, and bottom right: 0.5 mol% NBD-PE/POPC). (b) Epifuorescence image of SLBs array addressed in three microchannels. The three lipid bilayer regions are 0.5 mol%, 0.2 mol%, and 0.05 mol% TR-DHPE/POPC from left to right. Scale bar is 200 μm.

be spatially addressed into a single microchip by repeating this process. Figure 3.4a shows the epifluorescence image of four 99 ± 4 μm circles addressed with four chemically different lipid bilayers, including 0.5 mol% TR-DHPE/POPC, 0.1 mol% TR-DHPE/POPC, 2.0 mol% NBD-PE/POPC, and 0.5 mol% NBD-PE/POPC.

By using the same strategy, SLBs with different components can also be spatially addressed into individual microfluidic channels. Microfluidic devices are consisted of PDMS molds and quartz substrates. It should be noted that instead of glass, quartz is used as the substrate of microfluidic device since deep UV at ~ 190 nm, which is necessary for protein ablation, cannot penetrate through PDMS and glass. Protein solutions were injected into four individual microchannels and allowed to incubate for 20 min to form a thin protein film coating on quartz surface and PDMS walls. After incubation, purified water was flushed through the channels to remove excess proteins. Next, deep UV radiation was passed through a photomask localized on bottom of the microfluidic device as shown in Figure 3.1. The photomask was made by bringing two glass coverslips close to each other over a quartz substrate. The slit between the two glass coverslips is ~ 450 μm wide. Thus deep UV can pass through the slit, but is otherwise completely absorbed by glasses. After removing the proteins exposed to deep UV, vesicle solution was injected into the microchannels. Vesicle fusion occurred on both the PDMS walls and the glass substrate to form a continuous lipid bilayer coating.[17] The incubation time for bilayer formation was 5 min. The microchannels were rinsed with PBS buffer to remove excess vesicles. By repeating these steps, three different lipid bilayers were patterned inside four microchannels as illustrated in Figure 3.4b. The three lipid bilayers are 0.5 mol%, 0.2 mol%, and 0.05 mol% TR-DHPE/POPC from left to right.

To prove such SLBs spatially addressed microfluidic device is suitable for multiple multivalent ligand-receptor interactions measurement simultaneously, pentavalent CTB-GM_1 system was chosen as a demo. The microfluidic device was fabricated from quartz substrate and PDMS mold with seven microchannels. Each microchannel was spatially addressed with four POPC bilayer regions containing 0 mol%, 0.2 mol%, 0.5 mol%, and 2.0 mol% GM_1 ligand from left to right as shown in Figure 3.5a. TIRF microscopy was applied to study the pentavalent CTB-GM_1 interactions as a function of ligand density. Before the injection of protein solution, the bilayer-coated microchannels were incubated with a 0.5 mg/mL Rabbit IgG antibody solution for 30 min to block defect sites in the membrane and thereby suppress non-specific adsorption of CTB. Next, Alexa 594-labeled CTB solutions were flowed through each channel at various concentrations, simultaneously at a rate of 0.2 μL/min. The surface binding process was monitored by TIRF microscope as a function of time until the fluorescence intensity remained constant. A typical TIRF age is shown in Figure 3.5a. In this case the bulk CTB concentration ranged from 0.09 nM to 2.15 nM (top to bottom). Pure POPC bilayers outlined with the first red rectangle on left, was used as a background control. Under the present conditions, virtually no background fluorescence signal was observed, as the bulk protein concentrations were so low.[34,115] Intensity profiles across the TIRF image (red rectangles shown in Figure 3.5a) were employed to obtain quantitative binding data. Figure 3.5b shows the binding

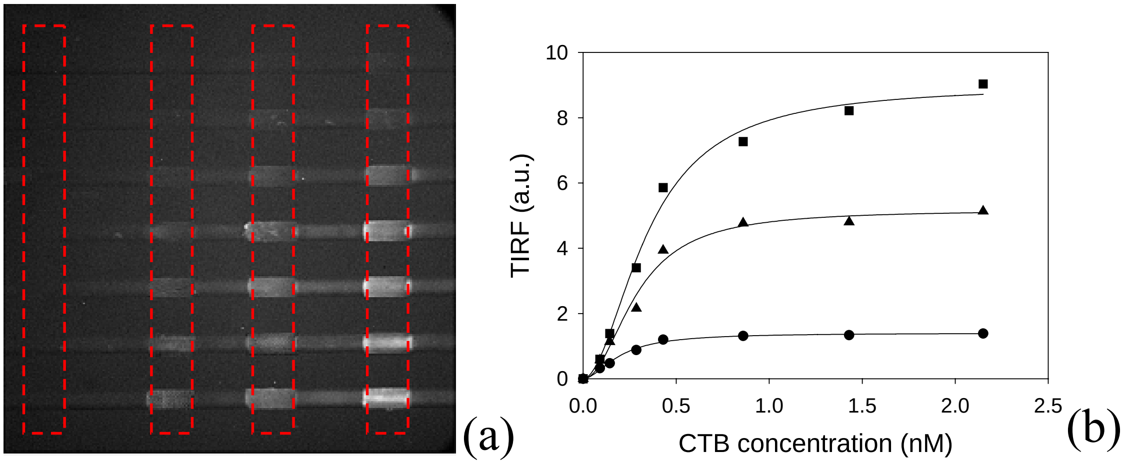

Figure 3.5. (a) TIRF image of lipid bilayers-coated microchannel array containing various concentrations of dye-labeled CTB. Lipid bilayers highlighted in four red rectangles from left to right are pure POPC, GM_1/POPC containing 0.2, 0.5, and 2.0 mol% GM_1, respectively. (b) Fluorescence signal vs. bulk CTB concentration in supported POPC membranes containing 2.0 (square), 0.5 (triangle), 0.2 (circle) mol% GM_1. The curves were fit to the Hill-Waud equation.

results on supported POPC membranes containing 2.0 mol%, 0.5 mol%, and 0.2 mol% GM_1.

To abstract equilibrium dissociation constant data from the CTB-GM_1 binding data, the curves were fit to Hill-Waud (eq 1) binding model[34,94,122]:

$$F = F_{\max} \times \frac{([P])^n}{(K_d)^n + ([P])^n} \tag{5}$$

where F is the fluorescence intensity from surface bound proteins, F_{max} is the maximum fluorescence intensity when proteins completely saturated the bilayer surface, $[P]$ is the bulk CTB concentration, K_d is the apparent equilibrium dissociation constants, and n is the Hill coefficient of cooperativity.[122] In our previous work[34], this binding model was found to be more suitable to pentavalent CTB-GM_1 interaction compared with Langmuir adsorption isotherm model. The Hill-Waud model was also used by other groups, and proved to be good at fitting CTB-GM_1 binding data.[94,122] The apparent dissociation constants K_d extracted from Figure 3.5b are 0.20 nM, 0.29 nM, and 0.35 nM for 0.2 mol%, 0.5 mol%, and 2.0 mol% GM_1/POPC, respectively. The binding results are in good agreement with our previous study of CTB-GM_1 interaction.[34] Also it can be found that the apparent dissociation constant weakens as a function of GM_1 density in the POPC bilayer. Such effect of ligand density on CTB-GM_1 interaction was contributed to the clustering of GM_1 in the supported phospholipid membranes, which in turn inhibits the binding of CTB. GM_1 clustering was directly verified by atomic force microscopy (AFM) experiments.[34]

In this binding study, two things should be noted. One thing is the spontaneous lipid transfer between existed supported lipid bilayers and vesicles for subsequent lipid bilayer formation.[157] If such transfer happens very quickly during the patterning of supported GM_1/POPC bilayer arrays in microchannels, GM_1 density in POPC bilayers should thus be calibrated. To check the effect of lipid transfer, one control experiment was conducted by incubation of pure POPC vesicle solution with solid supported 0.1 mol% TR-DHPE/POPC bilayers for 1 hour which is longer than the time necessary for GM_1/POPC bilayer array formation in microchannels. Then bulk vesicle solution was rinsed with copious PBS buffer. The fluorescence intensity of supported lipid bilayer before incubation and after 1 hour incubation showed no difference. This result suggests that spontaneous lipid transfer is negligible for SLBs microarray formation and multivalent interactions under the present experimental conditions.

Discussion

Besides BSA, other proteins such as IgG and fibrinogen can also be selectively removed from solid substrates by deep UV radiation and used as sacrifice layers for SLBs spatial addressing. Although other strategies including microcontact printing[156], micro-electrochemical lithography[158], nanoshaving lithography[159], and photolithography[160,161] have been developed for protein patterning on solid substrates, they need to use PDMS molds, electrodes, AFM tips, or photoactive moieties. Compared to these methods, deep UV lithography for protein patterning is relatively elegant, simple, and easy to control. It should be noted that deep UV at ~ 190 nm is necessary for the degradation of proteins.

The working mechanism of deep UV for photochemical degradation of proteins could contribute to the high energy (~ 150 kcal/mol) of photons at the wavelength of ~ 190 nm, since the energy is higher than most of the single bonds and multiple bonds of proteins. The energy of UV with higher wavelength (e.g. 254 nm) is not high enough to crack the chemical structure of proteins such as BSA. This mechanism can be proved by switching the quartz substrate over which photomask is coated to glass or PDMS. In Figure 3.6a, UV-Vis spectra show that quartz is transparent to UV down to 190 nm, UV above 240 nm can pass PDMS, and glass almost blocks most of the UV light. By conducting the experiment as illustrated in Figure 3.1 with different photomask substrates, results showed that dye-labeled BSA pattern could only be created by using quartz photomask substrate. It means that deep UV at ~ 190 nm is necessary for the ablation of proteins. Figure 3.6b demonstrates that after 2 min exposure to deep UV, the BSA monolayer can be removed. This result is consistent with previous reports that deep UV at ~ 190 nm can be used to degrade organosliane monolayers[152,153] and S-layer proteins[154].

Another ablation mechanism in the case of lipid bilayers was proposed by Parikh and colleagues.[79,80] They mentioned that two wavelength, ~ 185 nm and ~ 254 nm, of the mercury lamp are both relevant to the photodegradation process. Strong oxidizing agents including ozone and singlet molecular oxygen ($^1O_2$*) were created after the ~ 185 nm wavelength was absorbed by O_2 in the solution. Lipid molecules were excited by absorbing ~ 254 nm wavelength to produce ions, free radicals, and excited molecules.

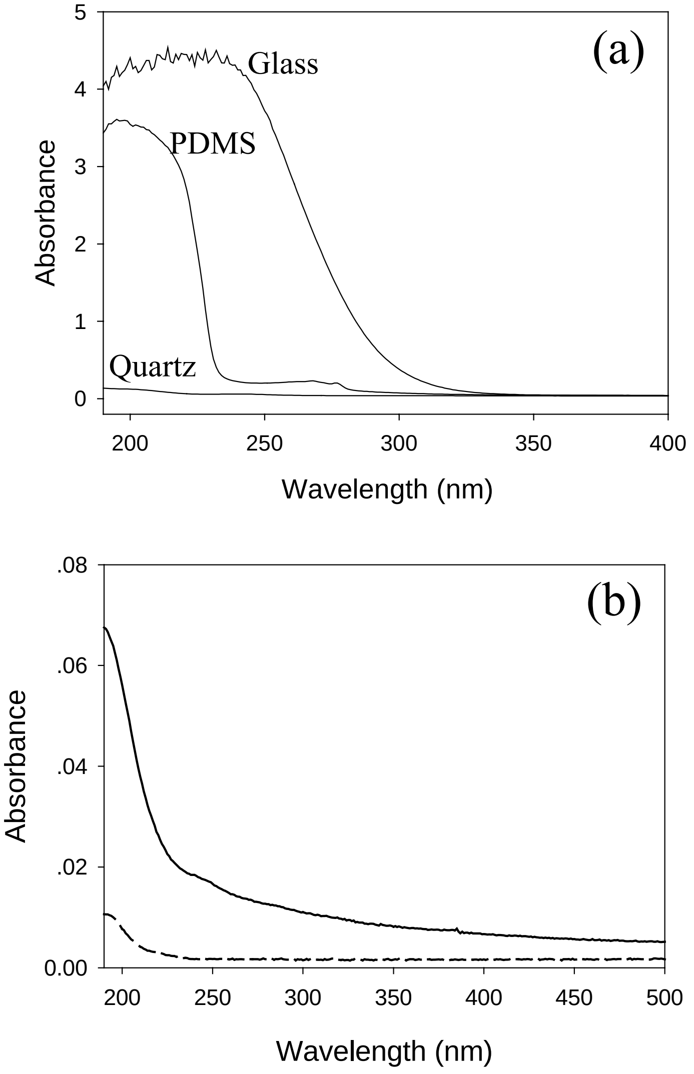

Figure 3.6. (a) UV-Vis spectra of quartz, PDMS, and glass. (b) UV-Vis spectra of BSA monolayer-coated quartz before (solid line) and after 2 min deep UV exposure (dash line).

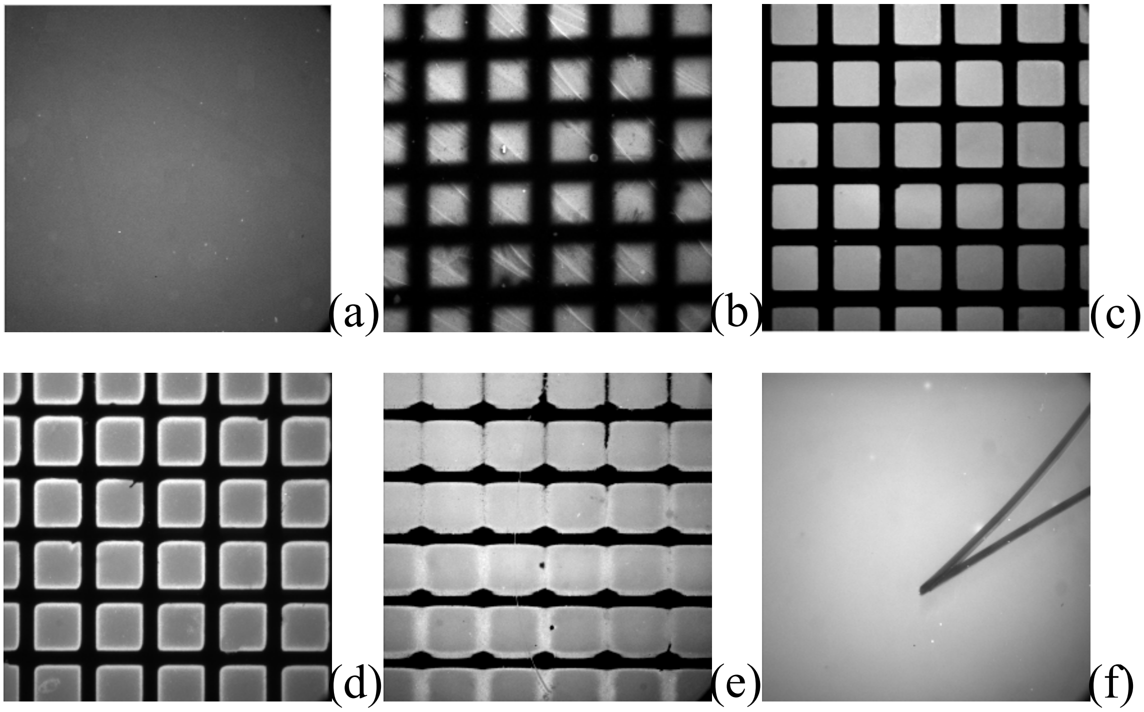

Figure 3.7. Epifluorescence image of 0.1 mol% TR-DHPE/POPC bilayer microaaray with different deep UV exposure time: (a) 0, (b) 30, (c) 120, (d) 180, (e) 300, (f) 450 sec.

When the activated species were reacted with $^1O_2$* and O_3, lipid molecules were degraded and dissolved in the solution. Real-time ATR-FTIR spectroscopy was used to monitor the products of the deep UV-induced lipid degradation.[79,80]

It should be also noted that radiation exposure time is the key parameter for uniform lipid bilayer formation. Results in Figure 3.7 show epifluorescence images of TX-DHPE/POPC bilayer as a function of exposure time. Figure 3.7a shows that without deep UV exposure, SLBs cannot form on BSA monolayer. When the exposure time is not enough, BSA cannot be fully degraded, and the quality of SLBs is not good. When the BSA monolayer is overexposed, lipid vesicles adsorbed on the boundaries can be observed (Fiugre 3.7d and 3.7e). The reason may be contributed to the low collimation quality of deep UV light from mercury Pen-Ray lamp. Then BSA under photomask-covered regions will be partially degraded by the deep UV radiation and induces the adsorption of lipid vesicles. When the exposure time further increased, uniform lipid bilayer can form on the whole substrate without any pattern. Scratches in Figure 3.7f were made by a sharp needle for image focusing. Uniform lipid bilayer patterns can only be obtained under the optimal conditions as shown in Figure 3.7c. This parameter will vary from different proteins.

Conclusion

This chapter developed a novel technique for spatial addressing of SLBs in a single microchip or individual microfluidic channels using a protein sacrifice layer. These arrays could, in turn, be employed in high throughput assays for biosensing, enzyme kinetics, and multivalent ligand-receptor isotherms. In fact, in conjunction with TIRFM, multiple equilibrium dissociation constants were abstracted from one-shot binding experiments. Other advantages include low protein consumption and elimination of experimental errors. Besides, with the size reduction of lipid bilayer regions in microchannels, more binding curves could be obtained simultaneously. And if different kinds of ligands were addressed in one assay, numerous ligand-receptor interactions could be compared, not necessarily limited to multivalent events.

CHAPTER IV

CHARACTERIZATION OF PHOSPHATASE ENZYME TETHERED TO SUPPORTED LIPID BILAYERS: EFFECT OF ENZYME SURFACE DENSITY

Introduction

Enzyme immobilization on various surfaces has gathered great attention for its numerous applications on biosensors, bioreactors, bioelectronics, biofuel cells, immunoassays, etc.[160,162,163] The integration of enzymes with solid supports has been achieved by many technologies, which can conveniently be divided into three categories.[160,164] Adsorption immobilization can non-covalently assemble enzymes to surfaces by electrostatic, hydrophobic, and hydrophilic interactions. This method is simple, but suffers from nonspecific binding and enzyme leakage from substrates. Chemical immobilization methods involve the formation of covalent binding between enzymes and support materials. For example, amino, hydroxyl, and carboxyl groups on enzyme surfaces are often used in the attachment to supports containing different surface functional groups (carboxylic acid, amine, lactone, thiol, etc.). Affinity interactions, such as antigen-antibody and biotin-avidin (streptavidin) binding, provide a different technique for enzyme immobilization. Recently, our group utilized biotinylated phospholipid bilayers and protein layers photoattached with biotin-linked dye to immobilize and characterize avidin (streptavidin)-conjugated enzymes in microfluidic systems.[17,150]

Compared with enzymes in free solution, surface-immobilized enzymes have some prominent features, such as easy separation of the enzyme and the reaction product, and continuous re-use. However, immobilization often affects the stability and activity of the enzyme. The turnover number of enzymes upon immobilization could be reduced several folds to ~ 30 times relative to the soluble enzymes.[17,165-170] Several factors may contribute to the loss of enzyme activity, including partial enzyme denaturation, steric effects, enzyme orientations, and immobilization matrix microenvironment effects. To improve the immobilized enzyme activity, a lot of efforts have been made, such as controlling orientation of the linked enzyme, reducing nonspecific absorption, increasing distance between enzyme and substrate using a spacer arm, etc.[166,171-175] These strategies can reduce the steric hindrance and improve the substrate accessibility of enzyme catalytic sites.

Beyond the above efforts, few studies have been done to probe the effect of surface density of immobilized enzyme on its catalytic efficiency and turnover number, although surface density may affect the enzyme distribution, flexibility, lateral interactions, etc. DeLouise and Miller[168] covalently immobilized two different concentrations of glutathione-*S*-transferase (GST) on porous silicon films and measured the kinetic parameters. Results showed that the turnover rate is independent of the enzyme surface density, although the turnover number of immobilized GST is ~ 5 times lower than that of the free enzyme in solution. Xu et al.[167] utilized surface plasmon resonance spectroscopy and fiber optic absorbance spectrometer to monitor the enzymatic activity of biotin-β-lactamase immobilized on NeutrAvidin-functionlized chip. Kinetic parameters of surface-linked enzyme with three different enzyme surface coverages were obtained. The catalytic efficiency of the enzyme at low surface density is ~ 2 and ~ 9 times higher than that at medium and high surface density, but the turnover rate at three different densities shows little difference. Caseli et al.[170] reported the adsorption of three different densities of detergent-solubilized alkaline phosphatase onto dimyristoyl phosphatidic acid Langmuir-Blodgett films. Catalytic activity of the immobilized phosphatase with different surface densities was compared by measuring the conversion rate of 1 mM substrate of para-nitrophenyl phosphate. An increase of enzymatic activity was found as the enzyme surface density decreases. However, kinetic parameters including turnover number and catalytic efficiency were not provided in the work. These results inspired us to conduct a systematic study of surface density effects on enzyme activity.

In this chapter, we employed biotinylated phospholipid bilayers to immobilize streptavidin-conjugated alkaline phosphatase in microfluidic channels. Such biotin-streptavidin immobilization matrix in conjunction with supported lipid bilayers (SLBs) will provide some benefits. First, nonspecific absorption of phosphatase on supported lipid bilayers is tiny and lipid bilayer serves as a cushion to prevent the enzyme denaturation upon immobilization.[17] Second, an uniform oriented protein film could be generated without requiring a close packed monolayer on SLBs surface.[176] Third, 16:0 N-Biotinyl-Cap-PE and biotin-streptavidin linker provide a good space arm to facilitate the substrate access of enzyme active sites. Fourth, with two-dimensional fluidity of the lipid bilayer on solid supports, immobilized enzymes can be well organized on bilayer surface, and keeps mobile at low enzyme surface density. Besides, microfluidic devices made of glass and poly-(dimethylsiloxane) (PDMS) offer high-throughput capabilities and extremely low sample consumption, and can serve as supports for SLBs formation.[15]

To obtain enzyme turnover rates, catalytic efficiency, and other kinetic parameters under different enzyme surface densities, 4-methylumbelliferyl phosphate (MUP) was utilized as substrate for dephosphorylation. Biotinylated POPC bilayer was formed in microchannels by vesicle fusion method.[17,21] Alkaline phosphatase density on membrane surface can be controlled by changing the biotin-cap-PE percentage in POPC bilayers. Conversion rate of blue fluorescent product of 7-hydroxy-4-methylcoumarin (HMC) was recorded by Epifluorescence microscopy. Kinetic parameters were extracted using Lineweaver-Burk equation.[177] In addition, enzyme kinetics in free solution was also measured using the same microfluidic devices. Results indicate higher turnover rate and catalytic efficiency at low enzyme surface densities than at high densities, although the enzyme in solution shows the highest activity. Turnover rate and enzymatic efficiency increasing at low enzyme surface densities could be explained by low steric crowding hindrance and high enzyme fluidity, as well as the resulting improvement of substrate accessibility and affinity of enzyme catalytic sites.

Experimental

Materials Texas Red-labeled streptavidin, streptavidin-cojugated alkaline phosphatase (1:1 stoichiometry), 4-methylumbelliferyl phosphate (MUP), Texas Red-labeled 1,2-dihexadecanoyl-*sn*-glycero-3-phosphoethanolamine, triethylammonium salt

(TR-DHPE), and Fibrinogen were purchased from Molecular Probes, Inc. (Eugene, OR). 1-palmitoyl-2-oleoyl-sn-glycero-3-phosphocholine (POPC) and 16:0 N-Biotinyl-Cap-PE were obtained from Avanti Polar Lipids (Alabaster, AL). High blue fluorescent 7-Hydroxy-4-methylcoumarin (HMC), product of MUP dephosphorylation, was from Fisher Scientific. Borosilicate glass coverslips (VWR Scientific, No. 1, 22 × 22 mm) were used as microchannel substrates for lipid bilayer formation. PBS buffer solution (20 mM sodium phosphate, 150 mM NaCl, 0.2 mM sodium azide, and titrated to pH 7.2 with 2.0 M NaOH) was used for vesicle preparation. MUP and HMC solutions were prepared using carbonate buffer (pH 9.8, 50 mM Na_2CO_3, 50 mM $NaHCO_3$, ionic strength 150mM). Purified water for these experiments came from a NANOpure Ultrapure Water System (≥18.2 MΩ·cm, Barnstead, Dubuque, IA).

Small Unilamellar Vesicles Preparation Small unilamellar vesicles (SUVs) was prepared by vesicle extrusion as reported previously.[15,47,48] Briefly, phospholipids were dissolved in chloroform with the desired molar ratio. Bulk chloroform was dried under a stream of nitrogen and evaporated under vacuum overnight. PBS buffer (pH 7.2) was then added to the dried lipids to yield a lipid concentration of 2.5 mg/ml. After rehydration, the lipid samples were subject to at least five freeze-thaw cycles, and extruded more than seven times through a polycarbonate filter (Whatman) with 50 nm pores. SUVs prepared by this method were characterized by dynamic light scattering (90Plus particle size analyzer, Brookhaven Instruments Corp.) and showed a size distribution of 70 ± 10 nm in diameter. Sample vesicles include pure POPC, and biotin/POPC mixtures containing 0.01 mol% to 2.0 mol% biotin-cap-PE.

SLBs Formation in Microfluidic Devices All enzyme kinetics experiments were conducted inside linear arrays of lipid bilayer-coated microchannels (Figure 4.1). Each channel was ~ 150 μm in width, ~ 20 μm in height, and separated from its neighbors by ~ 250 μm barriers. The seven-channel microfluidic devices consisted of lithographically patterned PDMS molds (Dow Corning Sylgard Silicone Elastomer-184, Krayden, Inc.) and borosilicate glasses were prepared as previously described.[15] Briefly, 50 × 75 mm soda lime microscope slides were coated with a thin layer of hexamethyldisilazane (HMDS) to improve the adhesion of the photoresist to the glass surface,[124] followed by spin coating with Shipley 1827 photoresist to a thickness of 10 μm. Photomasks were prepared by transferring the geometry of microfluidic channels onto photographic films. The photoresist-coated substrates were then exposed using a Quintel 6000 mask aligner, treated with a 1:1 solution of Microposit developer concentrate (Microchem) and purified water, and baked at 120 °C overnight. After post-baking, the glass substrates were immersed in buffered oxide etchant (BOE) in an ultrasonic bath. The etching process included 1.5 min etching in BOE, 30 sec dipping in a 1M HCl solution, and 30 sec rinsing with purified water. This process was repeated seven cycles to get ~ 20 μm thick features. The remaining photoresist was removed with ethanol after etching. Inlet and outlet holes were punctured in to the PDMS for

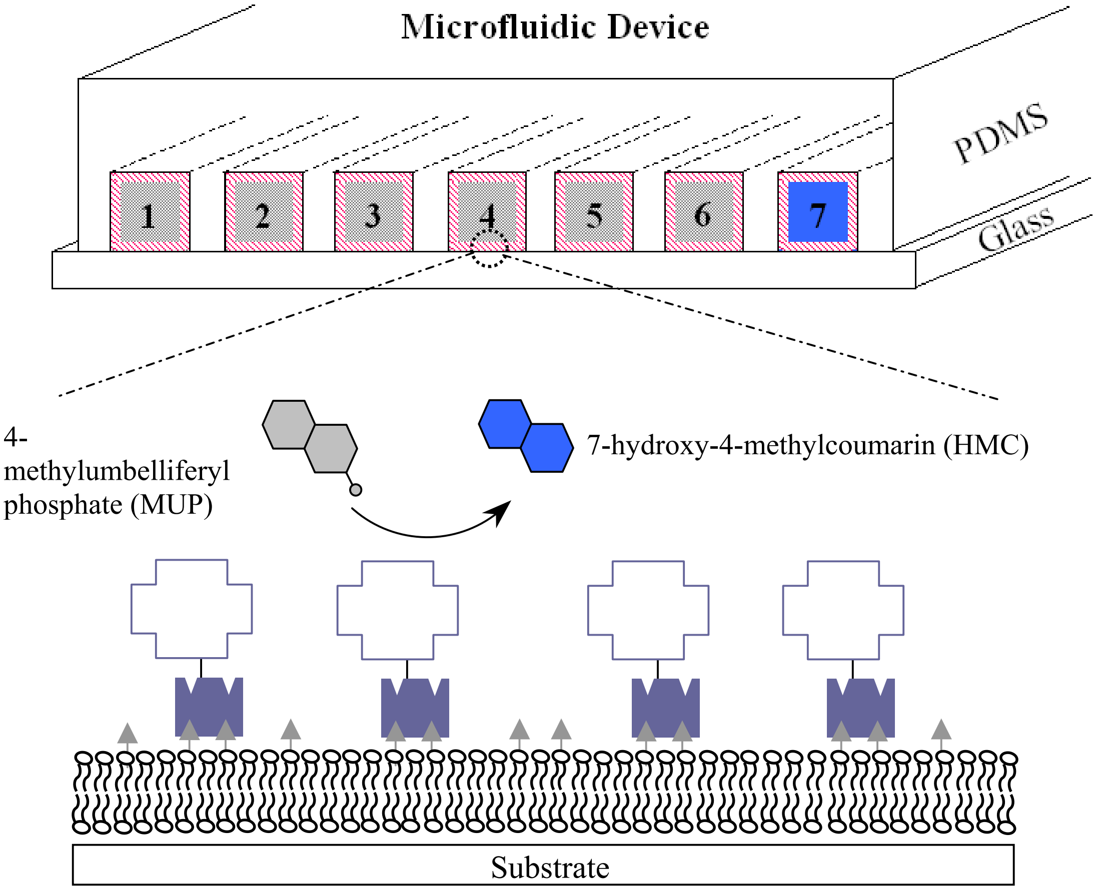

Figure 4.1. Schematic representation of seven-channel microfluidic device and streptavidin-conjugated alkaline phosphatase tethered to a biotinylated POPC bilayer. Channel 1 to 6 was filled with MUP solution with different concentrations and channel 7 was filled with 1.0 mM HMC as standard. For simplification, biotin molecules in the lower POPC leaflet were not drawn.

experimental purposes. Degassed PDMS was then poured over the glass master and cured in a convection oven at 55 °C overnight. The elastomeric molds, which bore the negative pattern of the master, were carefully peeled off and washed repeatedly with acetone and ethanol. Finally, the PDMS mold and a clean planar glass coverslip were treated by oxygen plasma (plasma cleaner PDC-32G, Harrick Scientific, Ossining, NY) for 30 s and brought immediately into contact to create the finished microfluidic device. It should be noted that the borosilicate coverslips were cleaned in hot surfactant solution (ICN ×7 detergent, Costa Mesa, CA), rinsed with copious amounts of purified water, and then annealed in a kiln at 480 °C for 5 h before use.

For SLBs formation, 5 μL of an SUV solution was injected through each inlet port of the linear array microfluidic device. It should be noted that this was done immediately after plasma treatment to insure that the surfaces rendered hydrophilic. Supported lipid bilayers formed spontaneously on both the PDMS walls and the glass substrate via the vesicle fusion method.[15,17] The incubation time for bilayer formation was 10 min. The microchannels were rinsed with PBS buffer to remove excess lipid vesicles. Fluorescence recovery after photobleaching (FRAP)[125,126] was employed to verify the quality of the supported bilayers on the channel surfaces.

Enzyme Immobilization SLBs containing biotin-cap-PE were first formed on the microchannel surfaces as described above. A solution of 5 mg/mL Fibrinogen in PBS buffer was then injected and incubated for 30 min before it was washed out by carbonate buffer (pH 9.8). This incubation step can passivate the defect sites in the membrane and thereby suppress the nonspecific absorption of alkaline phosphatase. Next, a solution of 0.02 mg/mL streptavidin-conjugated alkaline phosphatase was flowed through each channel using a Harvard PHD 2000 syringe pump (Harvard Apparatus, Holliston, MA) at a rate of 0.05 μL/min for 30 min. Total internal reflcection fluorescence (TIRF) experiments showed that biotin-streptavidin interaction could reach equilibrium under the above conditions. Extra alkaline phosphatase was washed out with carbonate buffer (pH 9.8). To obtain different enzyme surface densities, percentage of biotin-cap-PE in lipid membranes was changed from 0.01 mol% to 2.0 mol%. Alkaline phosphatase surface density, $[E]_s$, on the bilayer can be estimated from the footprint size of crystalline streptavidin, POPC headgroup area, and percentage of biotin in POPC bilayers.

Epifluorescence and TIRF Microscopy To check the quality and fluidity of supported lipid bilayers, FRAP studies were conducted using an inverted epifluorescence Nikon Eclipse TE2000-U microscope with a 10× objective. Laser radiation from a 2.5 W mixed gas Ar^+/K^+ laser (Stabilite 2018, Spectra Physics) was used to bleach the lipid bilayer samples. FRAP images were obtained with a MicroMax 1024b CCD camera (Princeton Instruments). FRAP experiments were also conducted to study the effect of biotin-cap-PE density on the mobility of streptavidin bound to lipid bilayers. Enzyme kinetics in microchannels was obtained using an upright Nikon E800 fluorescence microscope with a 4× objective. After the enzyme immobilization, the microfluidic device was placed under the microscope. One Harvard PHD 2000 syringe pump was employed to quickly infuse MUP solutions with different concentrations into the PDMS microchannels, simultaneously. Once the microchannels were filled with MUP solution, the flowing was stopped immediately, and fluorescence change during dephosphorylation of MUP by immobilized alkaline phosphatase was recorded by Roper Scientific Micromax 1024b CCD camera. Total internal reflection fluorescence (TIRF)[128,129] microscopy was employed to study biotin-streptavidin binding for the estimation of the protein density on lipid bilayer surfaces. TIRF can discriminate between dye-labeled streptavidin molecules bound to the supported membrane and those in the bulk solution. This allowed the proteins bound to the supported lipid bilayer to be studied with high specificity. All the fluorescence images were collected using Metamorph software (Universal Imaging Corp.) and transferred to Sigma Plot for further processing.

Results

Characterization of Immobilized Phosphatase For the characterization of surface immobilized alkaline phosphatase, 4-methylumbelliferyl phosphate (MUP) was chosen as the substrate for dephosphorylation, because MUP is only weakly fluorescent, but becomes strongly fluorescent in the blue visible light region upon dephosphorylation. A schematic representation of the alkaline phosphatase-immobilized PDMS microchannels bonded to a planar glass support is shown in Figure 4.1. The alkaline phosphatase was tethered to the lipid bilayers through biotin-streptavidin

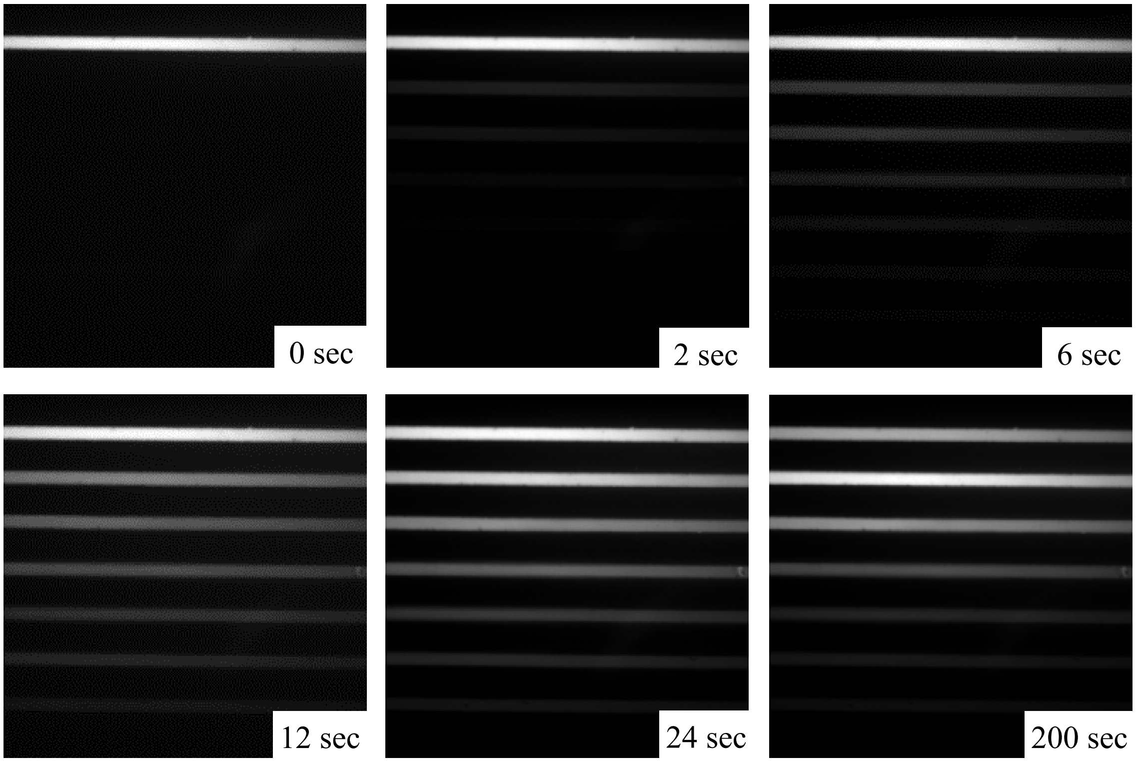

Figure 4.2. Time-lapse epifluorescence images revealing the conversion of MUP to HMC by the alkaline phosphatase tethered to the 0.08 mol% biotin/POPC bilayer. The top first channel was filled with 1.0 mM HMC as standard. Other six channels (top to bottom) were filled with MUP solution from 2.0 mM to 0.25 mM at 0 sec.

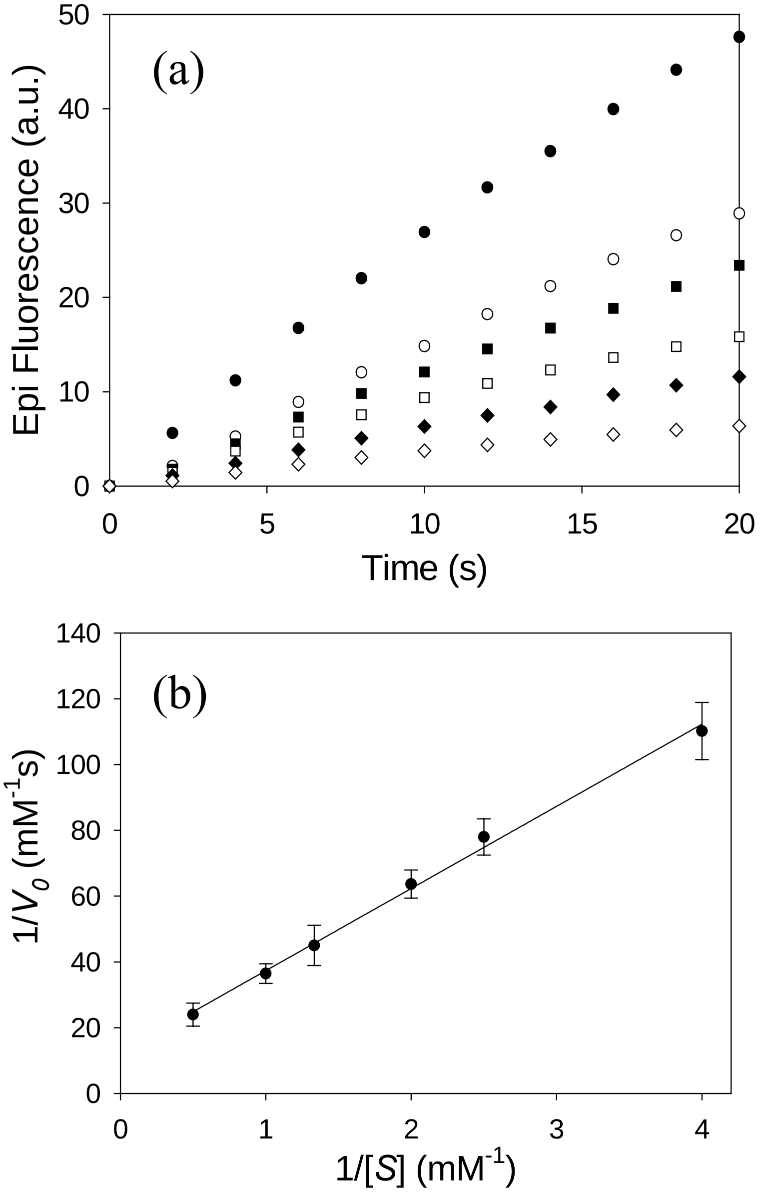

Figure 4.3. (a) Fluorescence intensity of HMC produced in the first 20 sec from the dephosphorylation reaction in six microchannels in Figure 4.2. (b) Lineweaver-Burk plot of the reciprocal initial reaction velocity obtained from (a) vs. the reciprocal of MUP substrate concentrations.

interaction. The formation of HMC product was monitored by following the change in the blue fluorescence intensity as a function of time (Figure 4.2). In this case, the concentration of MUP solution ranged from 0.25 mM to 2.0 mM (bottom to top, channel 1 to 6 in Figure 4.1). The supported POPC bilayers contained 0.08 mol% biotin-cap-PE. The top first channel (channel 7 in Figure 4.1) was filled with 1.0 mM HMC, product of dephosphorylation, as standard. After ~ 200 sec, the enzymatic reaction reached equilibrium. Comparing the maximum fluorescence signal from the channel filled with 1.0 mM MUP with that from the standard channel, it can be found that the conversion of 1.0 mM MUP to HMC is close to 100%. The maximum fluorescence intensity from each channel showed linearly related to the initial MUP concentration, which is consistent with the control experiment using HMC solution at the same concentrations. This result revealed that the conversion of MUP under the experimental conditions is complete.

The conversion of MUP to HMC was recorded by plotting the blue fluorescence intensity versus reaction time at each microchannel. The initial reaction velocity (v_0) was calculated by measuring the slope of the fluorescence change versus time for the first 20 sec (Figure 4.3a). Then the slope value was divided by the fluorescence density from the standard channel with 1.0 mM HMC to yield v_0 with the unit of *mM/s*. To obtain kinetic parameters including Michaelis-Menton constant and maximum velocity of the immobilized enzyme, the reciprocal initial velocity $1/v_0$ was plotted as a function of the reciprocal of substrate MUP initial concentration ($1/[S]$, mM^{-1}) as shown in Figure 4.3b. The data were fitted to the Lineweaver-Burk equation:[177]

$$1/v_0 = (K_M / V_{\max})/[S] + 1/V_{\max} \tag{6}$$

where K_M is the Michaelis-Menton constant indicating the affinity that an enzyme has for a given substrate, and V_{max} is the velocity of the reaction when the active sites of the enzyme are saturated with substrate. The results revealed that V_{max} is ~ 0.08 mM/s, and K_M is ~ 1.47 mM for alkaline phophatase immobilized on 0.08 mol% biotin/POPC bilayer surface.

Enzyme Surface Density Estimation To determine the turnover number (k_{cat}, s^{-1}) and catalytic efficiency (k_{cat}/K_M, $M^{-1}s^{-1}$) of the enzymatic reaction, it is necessary to estimate the total enzyme concentration ($[E]_T$, mM), since the turnover number is obtained from $k_{cat} = V_{max}/[E]_T$.[177] As alkaline phosphatase was immobilized on the membrane, the $[E]_T$ can be obtained from enzyme surface density ($[E]_s$, nmoles/dm^2) with known surface area and volume of the microchannels. In this study, two cases should be discussed about $[E]_s$. At high biotin concentration in lipid bilayers (≥ 1.0 mol%), streptavidin-conjugated alkaline phosphatase can saturate the membrane surfaces as described in our previous work.[17] In this case, enzyme surface density $[E]_s$ can be calculated from the footprint size of crystalline streptavidin (~ 33.6 nm^2).[178] Since streptavidin-conjugated alkaline phosphatase occupied ~ 4 times greater surface area per molecule than streptavidin alone,[17] we can get that $[E]_s$ at high biotin concentration equals ~ 0.124 nmoles/dm^2. With the known microchannel dimensions (height ~ 20 μm, width ~150 μm), the total enzyme concentration $[E]_T$ was calculated to

Table 4.1. The values of V_{max}, K_M, k_{cat}, and k_{cat}/K_M as a function of enzyme surface density.

Biotin/POPC (mol%)	$[B]_s$ (nmoles/dm^2)	$[E]_s$ (nmoles/dm^2)	$[E]_T$ (µM)	V_{max} (mM/s)	K_M (mM)	k_{cat} (s^{-1})	k_{cat}/K_M (µM^{-1}s^{-1})
2.0	0.48	0.124	1.405	0.48	2.06	342	0.17
0.8	0.19	0.095	1.076	0.45	2.10	419	0.20
0.4	0.095	0.048	0.538	0.24	1.85	447	0.26
0.2	0.048	0.024	0.265	0.12	1.54	449	0.29
0.1	0.024	0.012	0.135	0.086	1.49	638	0.43
0.08	0.019	9.50e-3	0.108	0.080	1.47	741	0.50
0.04	9.50e-3	4.75e-3	0.0537	0.038	0.99	708	0.72
0.01	2.37e-3	1.19e-3	0.0134	0.010	0.84	746	0.89

be ~ 1.41×10^{-3} mM as shown in Table 4.1. In the other case, streptavidin-conjugated alkaline phosphatase cannot saturate the bilayer-coated microchannel surfaces at low biotin concentration in lipid bilayers (less than 1.0 mol%). The $[E]_s$ will then change as the decreasing of biotin density in the membrane. Based on the strong interaction between biotin and streptavidin (equilibrium dissociation constant K_D, ~ 40 fM),[179] three assumptions were made in this estimation of enzyme surface density: (1) conjugation of phosphatase to streptavidin has no effect on the binding capability of streptavidin, (2) every biotin site is available for streptavidin binding, and (3) biotin sites are 100% bound to streptavidin at the ratio of 2:1. Then the value of $[E]_s$ equals half of the biotin surface density ($[B]_s$), which was calculated following our previously reported procedures.[16] The values for $[B]_s$ can be obtained by noting that the area occupied by a POPC headgroup is ~ 0.7 nm^2/molecule[137] and further assuming that the headgroup of biotin-cap-PE is roughly the same size. The results of $[B]_s$, $[E]_s$, and $[E]_T$ at different biotin concentrations were listed in the second and third column of Table 4.1.

Among the above three assumptions, the third one should be discussed to ensure that all biotin sites were bound to streptavidin bivalently under the experimental conditions. When the biotin percentage in lipid bilayers is higher than 0.08%, the biotin molecule number in the microchannel walls will be 2 times of that of 0.02 mg/mL (~ 100 nM) streptavidin in the microchannel. With the high mobility (~ 4 $\mu m^2/s$)[126] of lipid molecules in SLBs as determined by FRAP experiment, two binding sites of streptavidin can both bind to biotin. However, when the biotin density is 0.04 mol% or 0.01 mol% in POPC bilayers, some of biotin-streptavidin interactions may be monovalent since the ratio of streptavidin to biotin is higher than 1.0. In this case, we should calibrate the enzyme surface density. To prove that biotin-streptavidin interaction still follow bivalent binding at low biotin surface densities under the experimental conditions, one control experiment was conducted by using TIRFM.

As shown in the inset of Figure 4.4, pure POPC bilayers were formed in the 1st, 3rd, and 5th channels (from top to bottom) as background control, and 0.04 mol% biotin/POPC vesicles were fused through the 2nd, 4th, and 6th channels. Then Texas Red-conjugated streptavidin with high concentration (4.0 mg/mL or ~ 66.6 μM) was flowed through 5th and 6th channels very quickly, and low concentration solution of Texas Red-conjugated streptavidin (2.0×10^{-4} mg/mL or ~ 3.33 nM) was flowed through 1st and 2nd channels at the rate of 0.05 μL/min. Since streptavidin concentration in channel 2 is much lower than that of biotin and the flow rate is slow, it is easy for the monovalently bound streptavidin to encounter free biotin in the bilayer. So it is reasonable to assume that biotin-streptavidin interaction in the 2nd channel is all bivalent binding. In the 6th channel, it is hard for monovalently bound streptavidin to find free biotin in the membrane since high concentration streptavidin in bulk solution will quickly occupy all biotin binding sites. In this case, we can assume that the biotin-streptavidin interaction includes both bivalent and monovalent binding. Figure 4.4 demonstrates that the fluorescence intensity from channel 6 after subtracting background in channel 5 is ~ 1.4times of that from the 2nd channel. This result demonstrates the reasonability of the

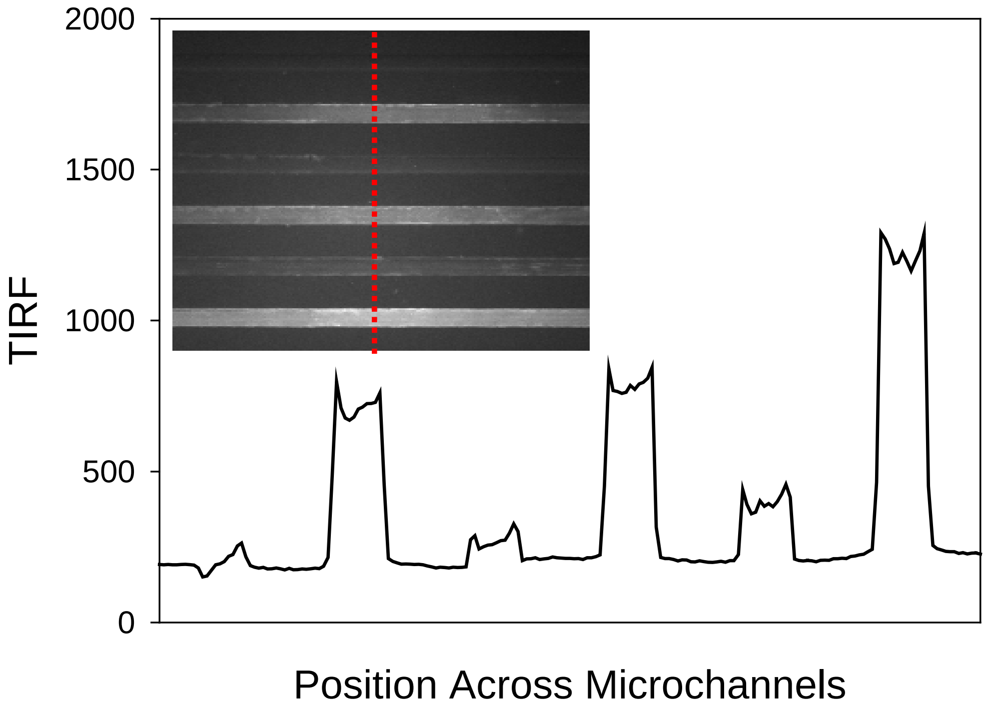

Figure 4.4. Intensity line scan of fluorescence from Texas Red-conjugated streptavidin bound to the lipid bilayer surfaces across six microchannels. From top to bottom, channel 1, 3, and 5 were coated with pure POPC bilayers, and channel 2, 4, and 6 were incubated with 0.04 mol% biotinylated POPC vesicles. Inset is the TIRF image of the six channels when the dye-label streptavidin binding reached equilibrium.

biotin-streptavidin monovalency and bivalency discussion. In the kinetics study, 0.02 mg/mL streptavidin-conjugated alkaline phosphatase (~ 100 nM) was used for the enzyme immobilization. For comparison, 100 nM Texas Red-conjugated streptavidin was flowed through the 3rd and 4th channels at the same rate (0.05 μL/min) used in the enzyme immobilization experiment. TIRF result in Figure 4.4 shows that fluorescence intensity from channel 4 after subtracting the background in channel 3 is very close to that from channel 2. From this result, we could claim that under low biotin surface density, biotin-streptavidin interaction still follows bivalent binding and that it is reasonable to estimate the enzyme surface density using $[B]_s$.

Kinetics of Immobilized and Free Phosphatase Similar kinetics experiments to those shown in Figures 4.2 and 4.3 were performed at eight biotin concentrations ranging from 0.01 to 2.0 mol% in POPC bilayers. The results of V_{max} and K_M of alkaline phosphatase immobilized on each of the biotin/POPC bilayers were extracted using the Lineweaver-Burk equation (eqn. 6). Figure 4.5 shows Lineweaver-Burk plots of the reciprocal initial reaction rates ($1/v_0$) versus the reciprocal of MUP concentration ($1/[S]$) for alkaline phosphatases immobilized on various POPC bilayers containing 2.0 mol%, 0.4 mol%, 0.2 mol%, 0.1 mol%, 0.08 mol%, and 0.04 mol% biotin. Other kinetic information can then be calculated from the known $[E]_T$, V_{max}, and K_M values. Table 4.1 summarizes the values of kinetic paramenters including Michaelis-Menten constant (K_M), maximum velocity (V_{max}), enzyme turnover number (k_{cat}), and catalytic efficiency

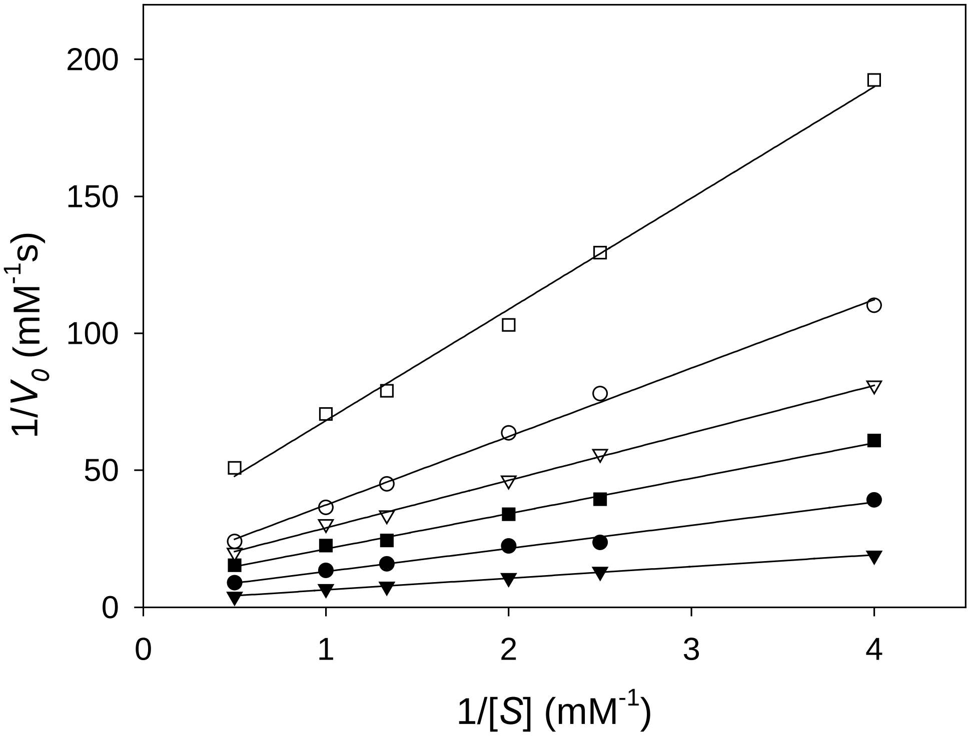

Figure 4.5. Six Lineweaver-Burk plots of $1/V_0$ vs. $1/[S]$ for the enzymes immobilized on various biotin densities in POPC bilayers: 2.0 mol%, 0.4 mol%, 0.2 mol%, 0.1 mol%, 0.08 mol%, and 0.04 mol% (from bottom to top).

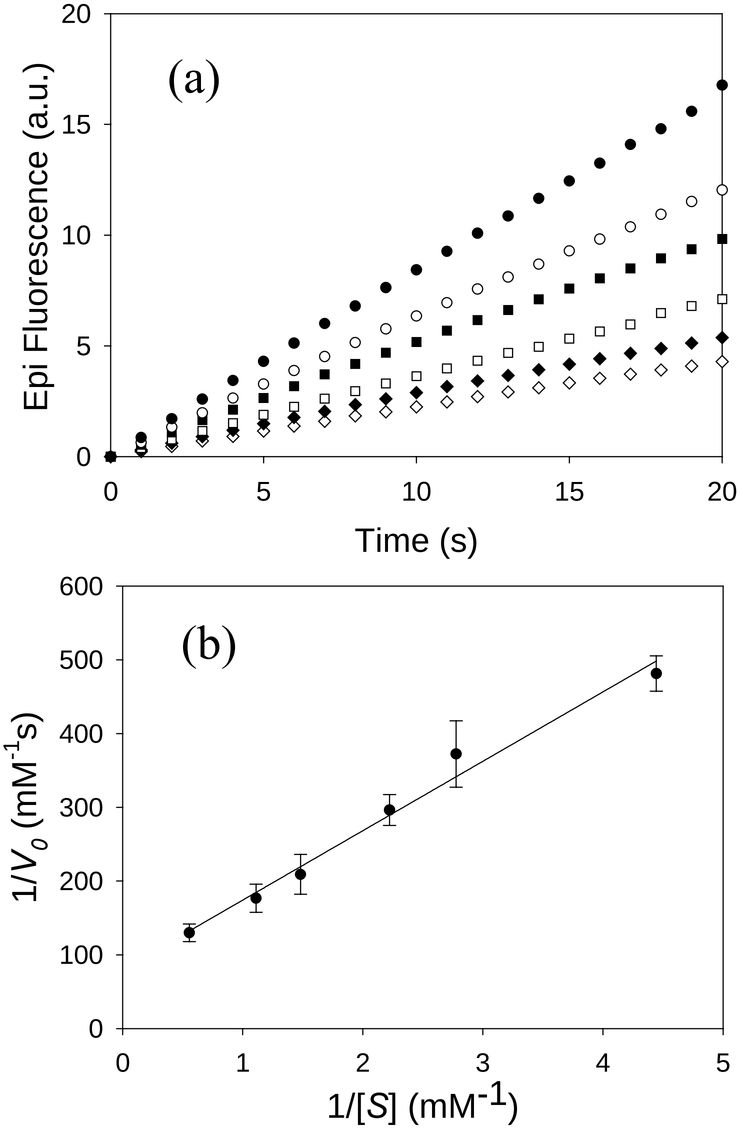

Figure 4.6. (a) Fluorescence intensity of HMC produced in the first 20 sec by soluble alkaline phosphate in six microchannels. (b) Lineweaver-Burk plot of the reciprocal initial reaction velocity obtained from (a) vs. the reciprocal of MUP substrate concentrations for 0.002mg/mL streptavidin-conjugated alkaline phosphatase in solution.

(k_{cat}/K_M) at various alkaline phosphatase densities ($[E]_T$). It can be seen that density increasing of immobilized alkaline phosphatase on lipid bilayer surfaces can result in an increase of V_{max}. The maximum velocity in the microfluidic system can reach ~ 0.5 mM/s at the high end. Surprisingly, the change of turnover number follows opposite way with the increasing $[E]_s$. The value of k_{cat} at low end of $[E]_s$ is ~ 2 times of that at high end. The enzymatic efficiency increases gradually to 0.89 $\mu M^{-1}s^{-1}$ as the enzyme surface density decreases. These phenomena will be discussed later.

For comparison, the activity of free streptavidin-conjugated alkaline phosphatase was also tested in solution for comparison with that of immobilized enzyme. The experimental conditions were identical to those used in kinetic studies of the immobilized enzyme, except for the fact that the lipid bilayers in the microchannels were absent. Instead, the streptavidin-conjugated alkaline phosphatase was quickly mixed with different concentrations of MUP using VWR Mini Vortexer and injected into each channel. In this case, the enzyme concentration in the bulk solutions was 0.002mg/mL (~ 10 nM), which is close to that of the immobilized enzyme at 0.01 mol% biotin/POPC membrane. The MUP substrate concentration ranges from 0.23 mM to 1.80 mM. Figure 4.6a shows the conversion of MUP to HMC by plotting the fluorescence intensity versus reaction time (first 20 sec) at each microchannel. Then the bulk solution values (K_M and V_{max}) were measured using the same Lineweaver-Burk analysis as plotted in Figure 4.6b. The results revealed that $V_{max} = 0.013 \pm 0.002$ mM/s and $K_M = 0.88 \pm 0.13$ mM. The turnover number and enzymatic efficiency in bulk solution were ~ 1300 s^{-1} and ~ 1.48 $\mu M^{-1}s^{-1}$, respectively. The calculations demonstrate that free alkaline phosphatase in bulk solution shows higher activity and efficiency than the enzyme tethered to lipid bilayers.

Discussion

From the above calculations, the turnover rate of alkaline phosphatase immobilized on the 2.0 mol% biotinylated membrane was roughly reduced 4 folds relative to the enzyme in solution. This result is consistent with our previous study,[17] in which several factors including steric effects and overestimation of enzyme surface density, were proposed to explain this phenomenon. It is not surprising that the high surface packing density will lower the accessibility of substrates to enzyme active sites, and may favor the conformational change and partial denaturation of the immobilized enzyme. However, few studies were conducted to probe the enzyme activity at low surface packing densities. Herein, the systematic study of effects of enzyme surface density on enzymatic activity could provide additional explanation for the apparent difference in k_{cat}.

The k_{cat} values as a function of $[E]_s$ from Table 4.1 were plotted in Figure 4.7a. As can be seen, the k_{cat} increases slowly as $[E]_s$ decreases from 0.12 to 0.024 nmoles/dm^2, and then increases quickly to level out as $[E]_s$ decreasing to 0.0012 nmoles/dm^2. In this case of alkaline phosphatase, it was demonstrated that the turnover rate at low enzyme surface densities is higher than that at high densities. However, the work reported by Xu et al.[167] and DeLouise et al.[168] showed no effect of enzyme surface

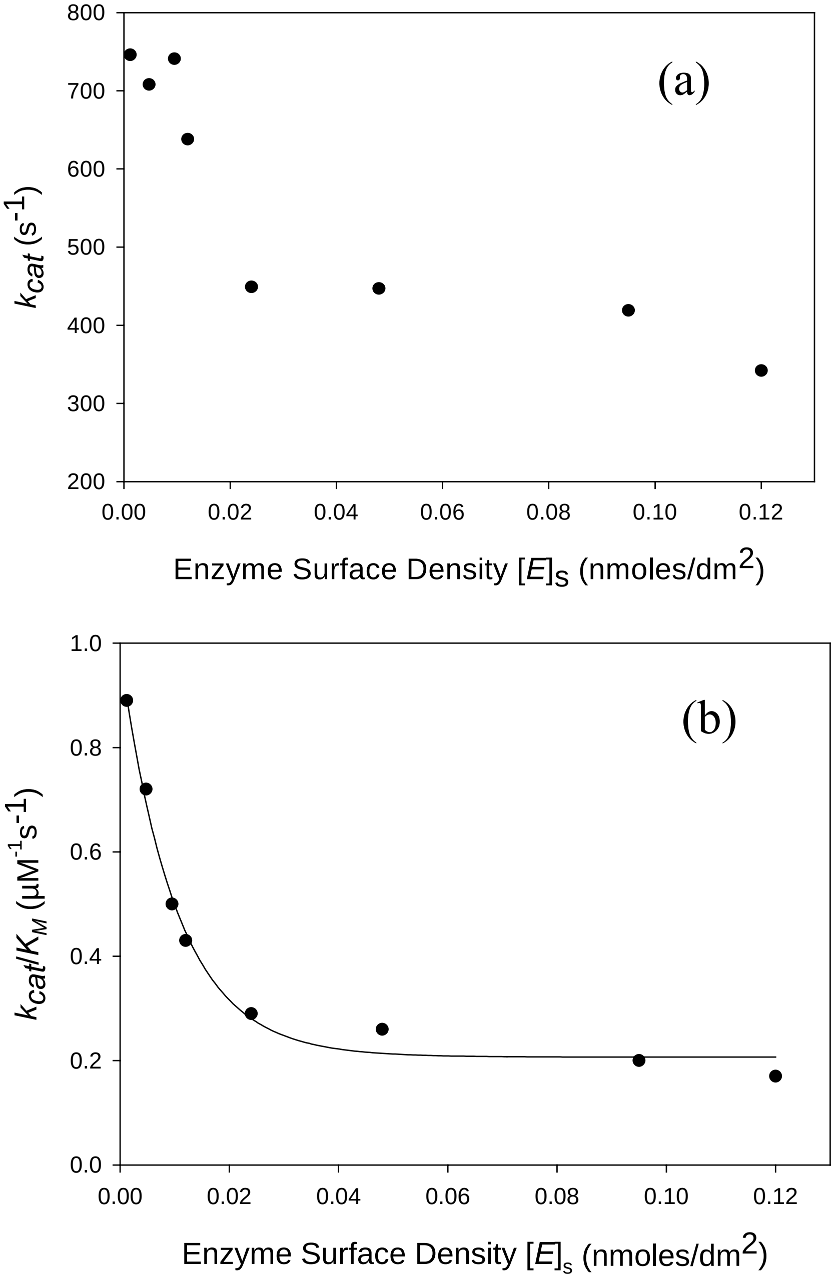

Figure 4.7. (a) Turnover rate vs. enzyme density on the lipid bilayer surfaces. (b) Fitted plot of catalytic efficiency as a function of enzyme surface density.

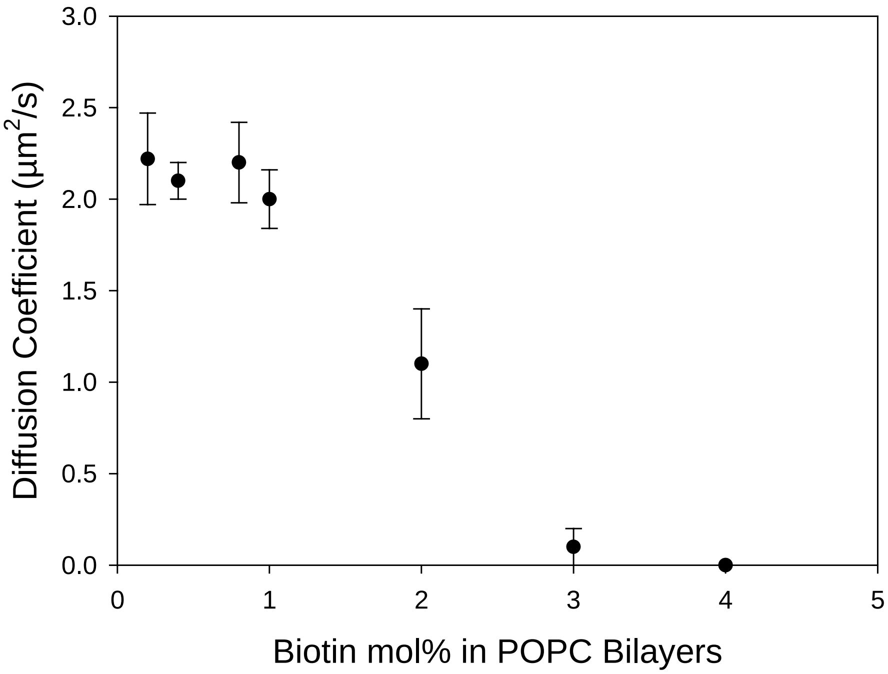

Figure 4.8. Diffusion coefficient of Texas Red-conjugated streptavidin tethered to biotinylated POPC bilayers vs. biotin density in the membrane.

density on turnover rate, although they agreed that surface immobilization would decrease the enzyme activity. One possibility of the opposite result may be from the fact that Xu and Delouise chose different enzymes. Considering another fact in their work that enzymes were immobilized on thiol- or aminosilane-terminated substrates, which means the enzyme molecules are not mobile on the surfaces, supported lipid bilayers have a unique feature of the fluidity of lipid molecules. Actually, Strittmatter and Rogers[180] proposed that a fluid bilayer is necessary to allow protein diffusion for efficient enzyme catalytic activity. They observed that the activity between cytochrome and cytochrome b5 reductase was increased 4 folds upon raising the temperature to the phase transition temperature of dimyristoyl lecithin liposome. Thus, enzyme mobility in the lipid bilayers could be one reason for the above controversial observation and one additional factor for the k_{cat} difference between the immobilized and soluble enzymes.

To investigate the mobility of enzymes tethered to the lipid membrane, FRAP experiments were performed as a function of biotin concentration in supported POPC bilayers. Texas Red-labeled streptavidin, instead of streptavidin-conjugated alkaline phosphatase, was chosen for the protein mobility study, since we know that the enzyme occupied ~ 4 times greater surface area per molecule than streptavidin alone.[17] After the formation of dye-labeled streptavidin monolayer on biotinylated POPC bilayers, Ar^+/K^+ laser was applied to make a 17.7 μm full width at half-maximum bleach spot in the protein layer. The recovery of the photobleached spot was monitored by time-lapse imaging. All fluorescence recovery curves were fit to a single exponential to obtain the half-time of recovery for the calculation of diffusion coefficient.[126] Figure 4.8 shows the effect of biotin density on the diffusion coefficient of streptavidin bound to the membrane surface. As can be seen, bilayer-tethered proteins are not mobile at high biotin densities ($\geq$ 4.0 mol%). The mobility shows an increase as the biotin density decreases, and levels out to ~ 2.0 $\mu m^2/s$ when the biotin percentage in POPC is lower than 0.8 mol%. Expanding this result to the case of streptavidin-conjugated alkaline phosphatase, it can be estimated that the bilayer-tethered enzyme molecules will be immobile at high biotin densities ($\geq$ 1.0 mol%) and reach the maximum mobility when the biotin density is lower than 0.2 mol%. Comparing this result with Figure 4.7a, we could claim that the particular property of enzyme mobility can reduce the steric crowding effects and accelerate the substrate recognition and accessibility of the enzyme active sites, resulting in the increasing of k_{cat} to some extent.

It should be noted that the k_{cat} in solution is ~ 1.7 times of that at low enzyme surface densities, under which the enzyme is highly mobile. For comparison, the k_{cat} in solution is around 4 folds of that at 2.0 mol% biotin/POPC, on which the enzyme is immobile. This fact indicates that besides the steric effects, packing density, etc., enzyme fluidity on substrate surfaces should be considered an additional factor for the k_{cat} difference between the immobilized and free enzymes. Considering that the protein diffusion coefficient in solution is much higher (10 ~ 100) than that in the fluid bilayer surface,[181,182] it is easy to understand why the free alkaline phosphatase in solution still holds higher turnover rate than the fluid one in the lipid membrane.

Effects of enzyme surface density on K_M and k_{cat}/K_M should also be discussed. The K_M values were gradually reduced with decreasing enzyme surface density. Since

K_M is an indicator of the affinity that an enzyme has for a given substrate,[177] the result means the recognition process of the enzyme and substrate was accelerated at decreased enzyme densities. This is consistent with the observation reported by Xu et al.[167] The k_{cat}/K_M, a measure of an enzyme's catalytic efficiency, was plotted in Figure 4.7b versus enzyme surface density. The catalytic efficiency decreases sharply as a function of $[E]_s$ at low densities, but begins to level out at higher densities. This curve could be fit by a single-exponential decay function: $y = y_0 + Ae^{-kx}$, where y is the quantity k_{cat}/K_M, y_0 is the lowest catalytic efficiency, A is a proportionality factor, x is enzyme surface density, and k is the apparent constant indicating the effect of $[E]_s$ on enzymatic efficiency. The abstracted parameters are $y_0 = 0.20\ \mu M^{-1}s^{-1}$, $A = 0.78\ \mu M^{-1}s^{-1}$, and $k = 98.0\ nM^{-1}dm^{-1}$. It can be inferred that at infinite low $[E]_s$, the catalytic efficiency of the immobilized enzyme can reach $0.98\ \mu M^{-1}s^{-1}$, which will be the highest enzymatic efficiency that the lipid bilayer-tethered phosphatase can obtain. This result demonstrates that the highly fluid enzymes on the membrane can get ~ 5 times improvement of the catalytic efficiency relative to the immobile enzymes.

Conclusion

In the experiments presented in this chapter, enzyme kinetics of alkaline phosphatase tethered on phospholipid bilayers was investigated using microfluidic devices in conjunction with epifluorescence microscopy. Systematic studies on the enzymatic activity of phosphatase were undertaken as a function of enzyme surface density. The turnover rate and enzymatic efficiency for the immobilized phosphatase were highly improved at low surface densities, although the enzyme in solution holds the highest activity and efficiency. This observation was ascribed to the high substrate accessibility and affinity to the enzyme active sites, as well as the high fluidity of lipid bilayer-bound enzyme molecules at low surface densities.

CHAPTER V

SUB-100 NM PATTERNING OF SUPPORTED BILAYERS BY NANOSHAVING LITHOGRAPHY

Introduction

Controlling the chemical composition of supported phospholipid bilayers (SLBs) on the micron and submicron scale has been a widely pursued goal in bioanalytical chemistry. For example, Jackson and Groves[85] applied scanning probe lithography to completely remove lipid membranes in pre-patterned 1 × 1 μm chromium arrays and then backfilled these regions with new lipid components. Orth and coworkers demonstrated ~ 1 μm scale SLB patterning using an elegant polymer lift-off method.[76] Lenhert et al.[82] developed a dip-pen nanolithography method for patterning bilayer/multi-bilayer structures down to the 100 nm scale.

These patterned membranes can be employed to address fundamental biophysical questions about cell membrane behavior.[26,37,91] For instance, Mossman and colleagues[37] showed that the radial location of T-cell receptors can be finely tuned in immunological synapses by using micropatterned SLBs. Wu et al.[91] demonstrated that micropatterned bilayers are useful for the visualization of membrane compartmentalization during receptor-mediated signaling. The fine patterning of lipid membranes may also serve as the basis for a variety of biosensor technologies.[13] One example is the formation of

---

*Reproduced with permission from "Sub-100 nm Patterning of Supported Bilayers by Nanoshaving Lithography" by Shi, J. J.; Chen, J. X.; Cremer, P. S. *J. Am. Chem. Soc.* **2008**, 130, 2718-2719. Copyright 2008 American Chemical Society.

submicron-sized SLBs inside Au nanoholes (~ 110 nm), which have been employed for label-free biorecognition in conjunction with localized surface plasmon resonance.[87,88]

Despite these successes, it is generally agreed that supported membrane patterning below the 100 nm scale would add an important new dimension to biophysical and bioanalytical studies. There should, however, be an ultimate size limit to free-standing SLB formation because these supramolecular architectures pay the cost of an edge energy in order to fuse to solid supports.[183,184] Chapter V used atomic force microscopy (AFM) based nanoshaving to control the formation of SLBs down to the sub-100 nm level. Nanoshaving employs an AFM tip to selectively remove a pre-existing thin film from a substrate.[159,185-189] The shaved region can be subsequently backfilled with new materials such as an SLB. The results in this chapter revealed that lines of phosphatidylcholine bilayers possessing widths as thin as 55 nm can be patterned on borosilicate supports, but not lines with 36 nm widths.

Experimental

Materials Bovine serum albumin (BSA) and Texas Red-conjugated BSA were purchased from Molecular Probes, Inc. (Eugene, OR). 1-Palmitoyl-2-oleoyl-*sn*-glycero-3-phosphocholine (POPC), 1,2-dihexanoyl-*sn*-glycero-3-phosphocholine (DHPC), and 1,2-dipalmitoyl-*sn*-glycero-3-phosphoethanolamine-*N*-(7-nitro-2-1,3-benzoxadiazol-4-yl) (Ammonium Salt) (NBD-PE) were purchased from Avanti Polar Lipids (Alabaster, AL). Phosphate buffered saline (PBS) solutions were used in all experiments. These solutions contained 20 mM sodium phosphate, 150 mM NaCl, and

0.2 mM sodium azide. The pH of the solution was set to 7.4 by the dropwise addition of 2.0 M NaOH. Purified water for these experiments came from a NANOpure Ultrapure Water System (≥18.2 MΩ·cm, Barnstead, Dubuque, IA). Borosilicate glass coverslips (VWR Scientific, No. 1, 22 × 22mm) were used as substrates for protein monolayer and lipid bilayer formation. It should be noted that the substrates were cleaned in a boiling 1:3 solution of ICN ×7 detergent and purified water. After cleaning, the substrates were rinsed with copious amounts of purified water, dried with nitrogen, and annealed in a kiln at 480 °C for 5 hours.

Vesicle Preparation Small unilamellar vesicles (SUVs) were prepared by vesicle extrusion.[47,48] Lipids dissolved in chloroform were dried under a stream of nitrogen followed by overnight vacuum desiccation. Next, the lipids were rehydrated in PBS solution. After five freeze-thaw cycles, the vesicles were extruded more than seven times through a polycarbonate filter (Whatman) containing 50 nm pores. These vesicles had a size distribution centered around 70 nm as determined by dynamic light scattering (Brookhaven Instruments 90Plus Particle Size Analyzer). These vesicles were employed to obtain all the data obtained in the main text. POPC vesicles containing 2.0 mol% NBD-PE were also extruded more than seven times through a polycarbonate filter (Whatman) containing 30 nm pores. The center of the size distribution for these vesicles was approximately 34 nm.

Epifluorescence Microscopy Epifluorescence images of protein patterns and SLB lines were obtained using a Nikon E800 fluorescence microscope equipped with a MicroMAX 1024B CCD camera (Roper Scientific). Removal of BSA was confirmed by fluorescently tagging protein molecules at a low degree of labeling (1 molecule in 20) with Texas Red and visualizing the system under the epifluorescence microscope. To check the quality and fluidity of the SLB lines, one-dimensional fluorescence recovery after photobleaching (FRAP)[190] studies were conducted using an inverted epifluorescence Nikon Eclipse TE2000-U microscope equipped with a Nikon Plan Fluor 40× oil immersion objective (NA 1.30). Laser radiation (488 nm, 200 mW) from a mixed gas Ar^+/K^+ laser (Stabilite 2018, Spectra Physics) was used to bleach the lipid bilayer samples. Bleaching times were less than 1 second and FRAP images were captured with the MicroMAX CCD camera.

Atomic Force Microscopy A Nanoscope IIIa Multimode SPM (Digital Instruments, Santa Barbara, CA) equipped with a J-type scanner was used for nanoshaving lithography and AFM imaging of BSA monolayers. An etched silicon tip (NSC15/NoAl; spring constant: ~ 40 N/m; MikroMasch, Wilsonville, OR) was used as the AFM probe. All images were obtained in tapping mode at a scan rate of 0.5 Hz. The only treatment applied to the images was flattening.

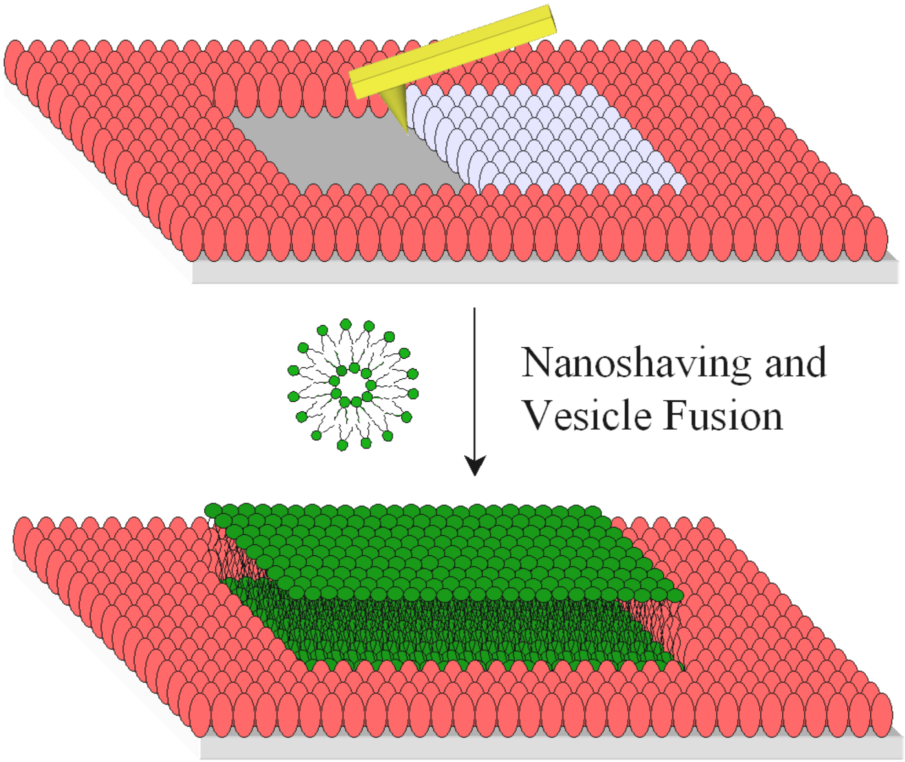

Figure 5.1. Schematic representation of AFM-based nanoshaving lithography for nanoscale SLB formation. The red and gray ellipsoids represent adsorbed BSA molecules. The gray ones are being removed by the AFM tip. A subsequently deposited lipid bilayer is shown in green.

Results and Discussion

A three-step process was conducted to create lines of SLBs as shown schematically in Figure 5.1. First, a bovine serum albumin (BSA) monolayer was formed on a planar borosilicate substrate by incubation with a phosphate buffered saline (PBS) solution containing 10 mg/mL BSA.[155] Excess protein molecules were washed away with purified water and the BSA monolayer was subsequently dried under streaming nitrogen. In a second step, immobilized protein molecules were selectively removed with an ultrasharp AFM tip in air in contact mode to create vacant lines with varying widths. The force applied to the tip was ~ 300 nN, which was sufficient to remove the protein without damaging the underlying surface. It should be noted that the Si tip was moved laterally in 2 nm steps in a process controlled by patterning software. The nanoshaving speed was 40 μm/s. The width of the patterned lines was directly measured by AFM. For convenience, 1 in 20 proteins was fluorescently tagged so that vacant regions could be observed by epifluorescence microscopy.

Backfilling was performed with a 0.5 mg/mL vesicle solution composed of 1-palmitoyl-2-oleoyl-sn-glycero-3-phosphocholine (POPC) with 2.0 mol% of a dye-labeled lipid (NBD-PE).[191] Small unilamellar lipid vesicles were incubated over the nanopatterned BSA substrate for 10 min. After rinsing with PBS solution, fluorescence microscopy clearly showed uniform fluorescence from 55 nm wide lines down to the diffraction limit (Figure 5.2a). This is consistent with the presence of lipid material within the shaved regions. The mobility of the bilayer in this narrow region was

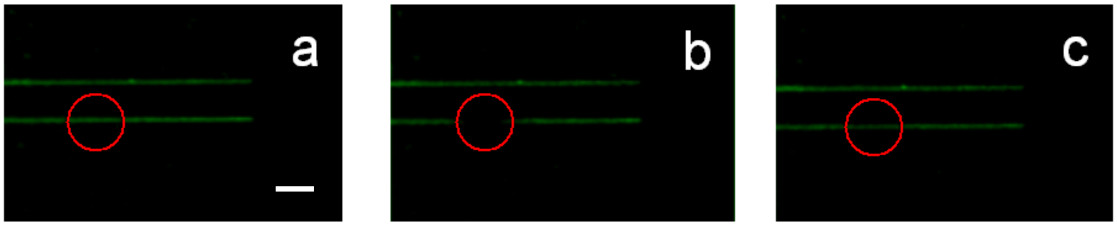

Figure 5.2. FRAP images of 2.0 mol% NBD-PE/POPC bilayer lines as a function of time that are ~ 55 nm in width. The bleached bilayer spot is shown (a) before bleaching, (b) immediately after bleaching, and (c) 120 sec later. The red circle denotes the location of the bleach spot. Only the bottom line was bleached and the upper one was used as a reference. The scale bar is 3 μm.

confirmed by one-dimensional fluorescence recovery after photobleaching (FRAP)[190]measurements. Figure 5.2b & 5.2c show the bleached spot immediately after it was made and 120 sec later, respectively.

To calculate the value of the diffusion constant, a one dimensional diffusion equation[190] was employed:

$$C_{0,t} = C_{0,0} \times R_o(R_o^2 + 8Dt)^{-1/2} \qquad (7)$$

where $C_{0,0}$ is the concentration of the bleached dye at the center point of the bleaching profile (Figure 5.3) at 0 sec, $C_{0,t}$ is the concentration of the bleached dye at the center point of the bleaching profile as a function of time, R_o is the half-width ($1/e^2$) of the bleach spot, and D is the diffusion constant. In the case of Figure 5.3, the half-width of the bleach spot is ~ 7.2 μm as calculated by fitting the initial bleaching profile ($t = 0$ sec) to a Gaussian profile.

From eqn. 7, a plot of $(C_{0,0}/C_{0,t})^2$ *vs.* time t should yield a straight line with a slope of $8D/R_o^2$. Figure 5.4 shows the linear relationship with a slope of 0.35 sec^{-1}. Hence, $D = 2.3 \times 10^{-8}$ cm^2/s. The average of 3 trials yielded a diffusion constant of $2.5 \pm 1.4 \times 10^{-8}$ cm^2/s. The mobile fraction was calculated by comparing the fluorescence intensity of the bilayer region before photobleaching and after recovery. The bottom line in Figure 5.3 was used a reference marker for the calibration of excitation light intensity and dye bleaching by continued imaging. Note that the bleached area must also be considered for the mobile fraction calculation, because the bleach spot occupied ~

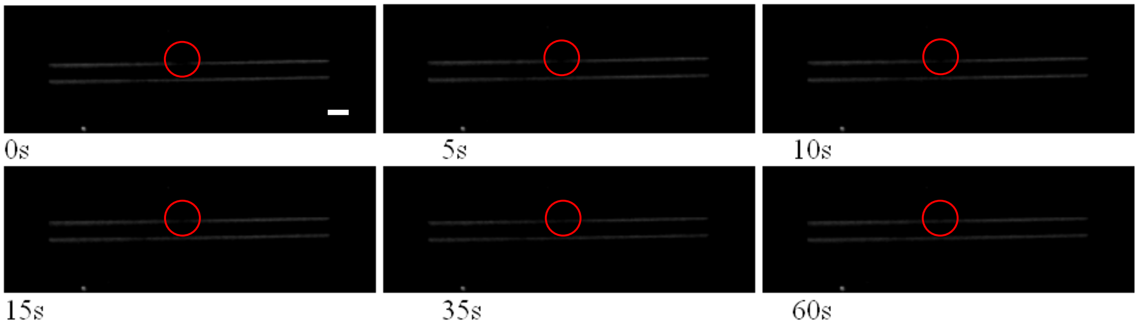

0s 5s 10s

15s 35s 60s

Figure 5.3. Time-lapse epifluorescence images of 2.0 mol% NBD-PE/POPC bilayer lines. The top line was bleached at the center, and the bottom one was used as a reference marker. The scale bar is 6 μm.

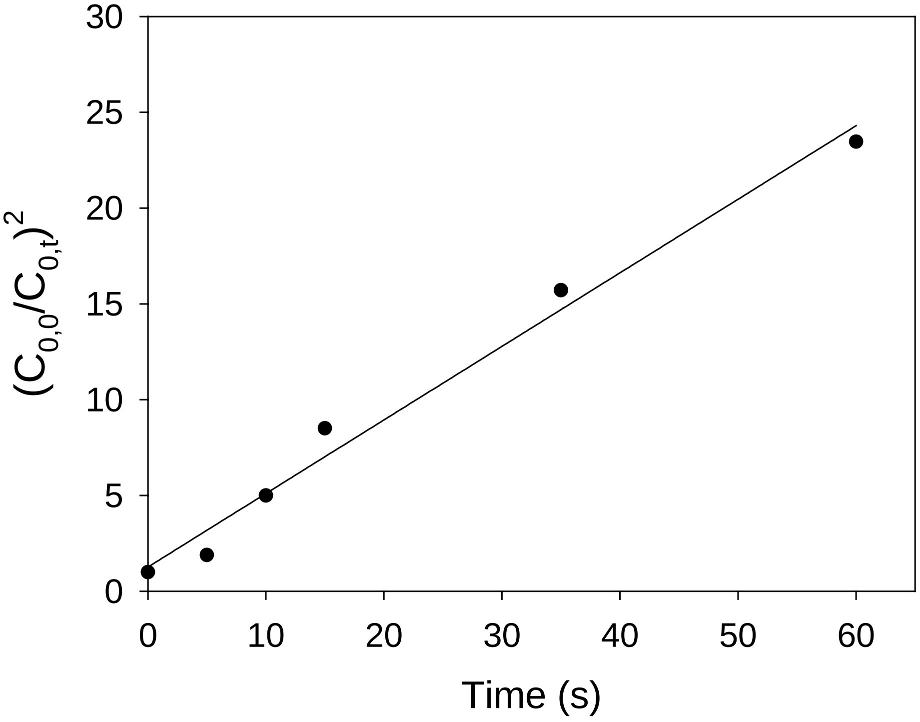

Figure 5.4. $(C_{0,0}/C_{0,t})^2$ vs. time for the calculation of the diffusion constant.

16% of the top line in Figure 5.3. Taking this into account yields a mobile fraction of ~ 0.97.

Next, a series of parallel lines ranging from 15 to 600 nm were formed under an identical set of nanoshaving conditions. After nanoshaving, the Texas Red-labeled BSA monolayer was imaged by epifluorescence microscopy (Figure 5.5a). Close-up AFM images for the identical protein line widths are provided in Figure 5.6. At this point, POPC vesicles containing 2.0 mol% NBD-PE were introduced over the sample. Epifluorescence images of the nascently formed lipid bilayers from this process are shown in Figure 5.5b. The smallest bilayer lines created by this method were 55 nm. On the other hand, the lipid material completely and consistently washed away from the surface when the line width was 36 nm or below. This finding was not changed by modulating the size of the vesicles.

Although sub-100 nm bilayer lines could be created, there is a clear size limit for POPC/glass bilayers. All free-standing SLB patches formed on solid supports (e.g. borosilicate glass) have an edge energy associated with them. Indeed, the bilayer is, presumably, highly curved along its perimeter to avoid exposing the hydrophobic lipid tails directly to water.[183,192] The concept of edge energy per unit length (γ, J/m)[183] describes the curvature cost over a given distance. The reason micron scale lipid bilayers readily fuse to planar supports is because the adhesion energy more than compensates for such line tension.[184] By contrast, the edge energy can be greater than the adhesion energy for nanoscale bilayers.

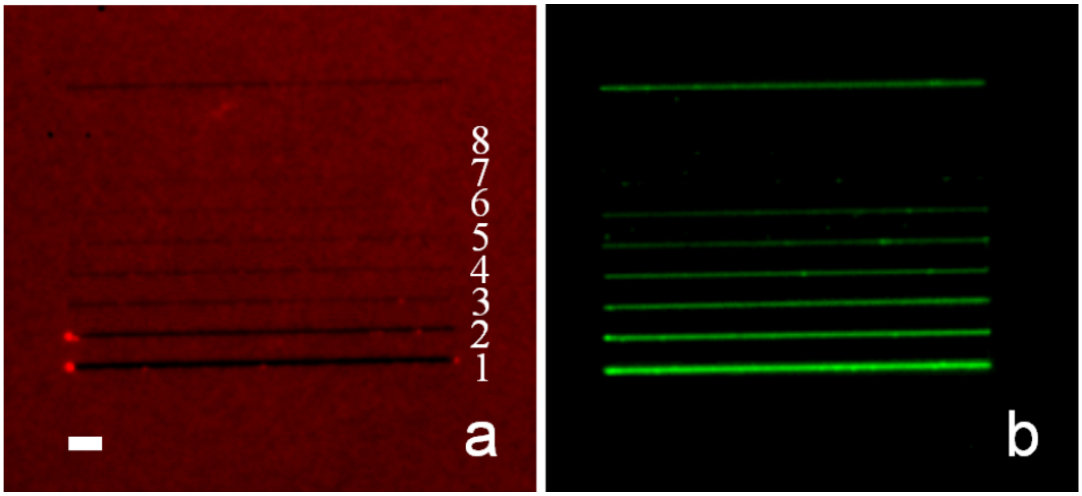

Figure 5.5. Epifluorescence images of (a) a nanoshaved BSA monolayer and (b) SLB lines. The top line, which is ~ 200 nm in width, was used as a reference marker. The widths of shaved lines in (a) from 1 to 8 are ~ 600 nm, ~ 300 nm, ~ 142 nm, ~ 103 nm, ~ 78 nm, ~ 55 nm, ~ 36 nm, and ~ 15 nm, respectively, as measured by AFM. The length of each line is 40 µm. The scale bar is 3 µm. Note, the vacant lines in (a) become increasingly difficult to observe by epifluorescence microscopy as the line width narrows. Green fluorescence emanating from these regions, however, should be trivial to observe even for the thinnest lines under the conditions of this experiment, if a bilayer is indeed present.

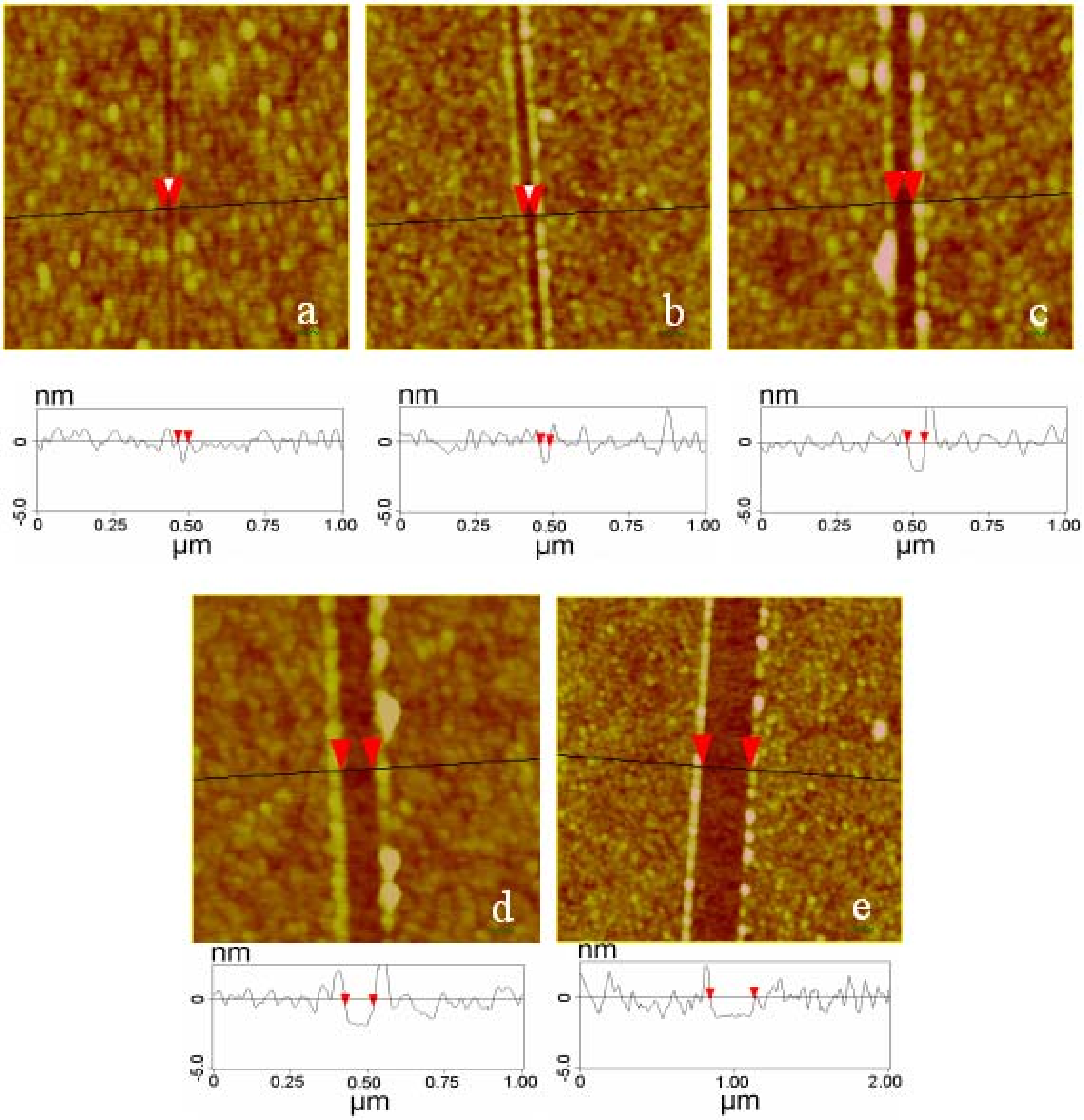

Figure 5.6. AFM images of a series of nanoshaved lines in a BSA monolayer. The width of the lines are: (a) ~ 15 nm, (b) ~ 36 nm; (c) ~ 55 nm; (d) ~ 103 nm; and (e) ~ 300 nm. The image size of (a), (b), (c), and (d) is 1 µm × 1 µm. The image size for (e) is 2 µm × 2 µm.

In the present case, bilayers are w μm wide and l μm long. Therefore, the edge energy, E_e, and surface adhesion energy, E_s, should be:

$$E_e = \gamma \times 2(w + l) \tag{8}$$

$$E_s = W \times wl \tag{9}$$

where W is the surface adhesion energy per unit area. Neglecting any interactions between the bilayer edge and the surrounding BSA molecules, the surface adhesion energy (eqn. 9) must be greater than or equal to the edge energy (eqn. 8) in order for a stable SLB to form:

$$W \times wl \geq \gamma \times 2(w + l) \tag{10}$$

since the length of the bilayer lines (e.g. 40 μm) is two to three orders of magnitude larger than their widths, eqn. 10 can be reduced and rearranged to:

$$w \geq 2\gamma / W \tag{11}$$

where the equality describes the minimum size for an SLB. The adhesion energy per unit area (W) of phosphocholine bilayers on glass substrates has been estimated to be ~ 2.0×10^{-4} J/m^2 in several reports.[88,192-194] Moreover, the typical edge energy per unit length (γ) of a phosphocholine bilayer is known to be ~ 1×10^{-11} J/m.[195-199] This leads to an estimated lower width limit of ~ 100 nm. Such a value is in reasonably good agreement with our finding of 55 nm. However, our number implies that W may be somewhat larger and/or that γ might be somewhat smaller. A slightly lower value of γ in the present case, for example, might stem from a slightly favorable interaction between the bilayer edge and neighboring BSA molecules.

The size limitations found in this chapter are almost certainly specific to the lipid composition of the membrane. Modulating the composition should lead to changes in γ. For example, supported bilayers comprised of a mixture of long-chain phospholipids with a small concentration of 1,2-dihexanoyl-*sn*-glycero-3-phosphocholine (DHPC) would be expected to have a lower edge energy and thus allow narrower line widths to be achieved. In fact, such compositions are often used to make lipid bicelles in bulk solution.[200] These pancake-like bilayer structures probably reduce edge energy by having a high concentration of DHPC along the edge. In fact, control experiments with POPC bilayers containing 6.0 mol% DHPC showed that ~ 36 nm wide lines could be made, but not ~ 15 nm.

Conclusion

Sub-100 nm wide supported phospholipid bilayers (SLBs) were patterned on a BSA patterned planar borosilicate substrate by AFM-based nanoshaving lithography. Bilayer lines were formed within the BSA vacant strips by vesicle fusion method. It was found that stable bilayers formed by this method had a lower size limit of ~ 55 nm in width. This size limit stems from a balance between a favorable bilayer adhesion energy and an unfavorable bilayer edge energy. The size limitations found in this chapter can be modulated by changing the lipid composition of the membranes. SLB arrays formed by this technique are expected to be very applicable for studying cell adhesion and growth, cell signaling, and the creation of biosensors.

CHAPTER VI

MEMBRANE-ASSOCIATED SPECIES SEPARATION BY POLYMER-CUSHIONED LIPID BILAYER ELECTROPHORESIS

Introduction

Since the first demonstration in 1977 that electric fields can reorganize the membrane-bound protein of Con A in cell membranes,[201] electrophoresis in solid-supported lipid bilayers has attracted considerable attentions. The technique has been applied in accumulation, reorganization, and separation of membrane components including charged lipids[202,203], tethered vesicles[204], and GPI-linked proteins[205]. More recently, two modified electrophoresis methods have been developed for the separation of lipid-associated fluorophores in SLBs. Daniel et al.[19] created a planar bilayer separation medium composed of phosphatidylcholine and cholesterol mixtures, which can limit the band broadening during electrophoresis. A complex mixture of lipids, tagged with three fluorescent labels, was isolated in this system. To overcome the productive limitation of planar bilayer system, Suzuki et al.[39] described a large-scale separation method by using a packed bed of bilayer-coated particles as an electrophoretic medium.

Electrophoresis in solid-supported lipid bilayers is now accepted as an ideal strategy to separate biomembrane species including lipids and transmembrane proteins, since the process does not require harsh conditions such as detergent extraction, and can maintain the structure and function of membrane components, compared to conventional methods. However, this method suffers from one fundamental drawback.[26] When transmembrane proteins, especially those presenting large peripheral domains, are incorporated in solid-supported lipid bilayers, the bilayer-substrate distance (~ 1 nm)[25] does not provide sufficient space to avoid the direct contact between the proteins and the solid surface, thus causing the immobilization and/or denaturation of the proteins.

Polymer-supported lipid bilayer system was thus proposed to separate the lipid membrane from the solid substrate by adding one ultrathin hydrophilic polymer layer between them. There are two main classes of polymers suitable for biomembrane supports. When lipid bilayers are created on polymer films, such as cellulose[53,54] and polyelectrolytes[57-61], which are deposited on solid substrates by physical absorption techniques, this system is called polymer-cushioned lipid bilayer. The polymer cushions behave like a cytoskeleton. The other strategy utilizes lipopolymer tethers to support bilayer formation. These polymers include one terminal group that binds to the substrate, another terminal group that inserts into the lipid bilayer, and one hydrophilic linker (e.g. polyethylene glycol, PEG) that defines the space between the substrate and the bilayer.[62-66] It is proven that membrane proteins are mobile and functional in such polymer-supported bilayer systems.[26]

This chapter investigated the separation of membrane-associated species by polymer-cushioned lipid bilayer electrophoresis. Bilayer separation medium was prepared on different polymer cushions including cellulose, polylysine, and poly-(*N*-isopropylacrylamide) (PNIPAM). The bilayer containing lipid-tagged fluorophores was

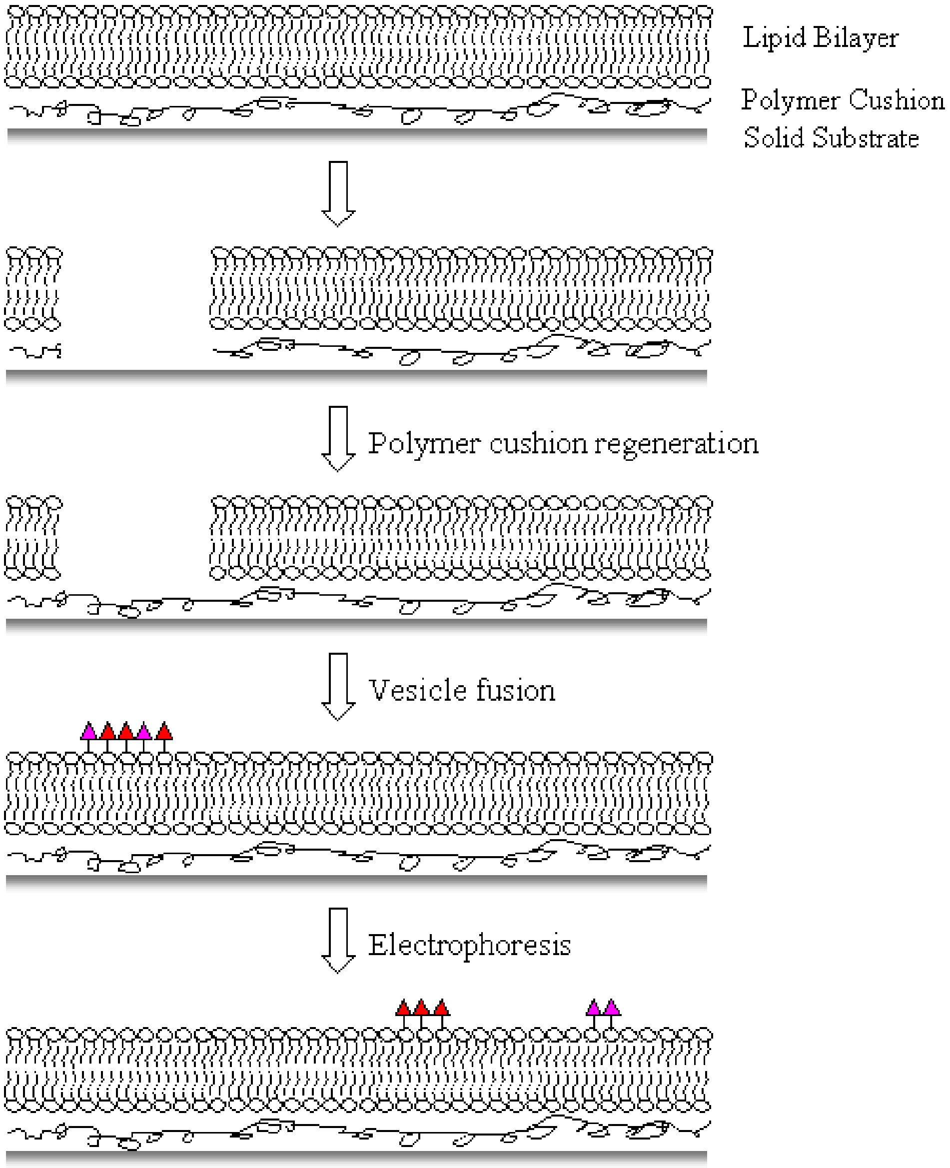

Figure 6.1. Schematic representation of the general steps for patterning and separation of membrane-associated species in polymer-cushioned lipid bilayers.

deposited adjacent to the separation medium by a three-step process (Figure 6.1). By applying potential laterally across the lipid bilayer, the Texas Red isomer mixtures were separated in the polymer-supported bilayer medium. This method was extended to the patterning of Escherichia Coli (E. Coli) membrane in the bilayer separation medium. The separation of membrane-associated proteins was discussed.

Experimental

Materials 1-palmitoyl-2-oleoyl-*sn*glycero-3-phosphocholine (POPC), 1,2-dilauroyl-sn-glycero-3-phosphocholine (DLPC), 1,2-Dipalmitoyl-sn-Glycero-3-phosphoethanolamine-N-(7-nitro-2-1,3-benzoxadiazol-4-yl) (Ammonium Salt) (NBD-PE) and cholesterol were purchased from Avanti Polar Lipids (Alabaster, AL). Texas Red 1,2-dihexadecanoyl-*sn*-glycero-3-phosphoethanolamine, triethylammonium salt (TR-DHPE) was obtained from Molecular Probes (Eugene, OR). Polymers including cellulose, polylysine, and poly-(*N*-isopropylacrylamide) were purchased from Sigma-Aldrich (St. Louis, MO). E. Coli vesicles were provided by Dr. Musser at Texas A&M Health Science Center.

Phosphate buffer saline (PBS) was made with 5 mM Na_2HPO_4, 5 mM NaH_2PO_4 and 150 mM NaCl. The pH was adjusted to 7.4 using sodium hydroxide. PBS solution was used in the preparation of vesicles. The purified water used in the preparation of all solutions was obtained from a NANOpure Ultra Water System (Barnstead, Dubuque, IA) with a minimum resistivity of 18 MΩ·cm. Quartz coverslips (1×1 inch, 0.2 mm thick, Electron Microscopy Sciences, Hatfield, PA) were used as substrates for bilayer formation, and boiled in 7X solution (MP Biomedicals, Aurora, OH) that was diluted four fold by volume with purified water. Platinum electrodes were made from platinum wire with a diameter of 0.25 mm from Alfa Aesar (Ward Hill, MA).

Thin polymer film preparation Cellulose film was prepared by Langmuir-Blodgett deposition of synthetic trimethylsilyl cellulose (TMSC) onto hydrophobic substrates and regenerated with HCl vapor.[206] TMSC was synthesized as following. Cellulose powder was first dissolved in the solution of 5-8% (w/w) lithium chloride / dimethylacetamide. The solution was then heated to 80 ^{o}C and hexamethyldisilazane was added in a steady flow in a nitrogen atmosphere. The reaction was kept overnight (~ 10 h). The product was cooled and some methanol was added to enhance the crystallization of TMSC, which was left to proceed overnight. Next, the methanol was added slowly till TMSC precipitates from the solution at 50°C. The crystallized TMSC was filtered and dissolved into tetrahydrofuran and recrystallized in methanol. After filtration, the recrystallized TMSC was washed several times with methanol and dried in a vacuum desiccator. NMR spectrum demonstrated that the silylated cellulose has a degree of substitution of ~ 2.4.

For the preparation of the TMSC film, a solution of 5 mg TMSC in 10 ml n-hexane was spread onto a water surface in a KSV5000 trough (KSV Instruments, Monroe, CT) at room temperature. The monolayer was compressed up to 17 mN/m and the deposition onto quartz slides surfaces was performed with a dipping speed of 1 cm/min. The quartz slides had been hydrophobized by incubation with 2.5mM OTS in toluene for 1 hour. After six dip-coating cycles, the TMSC film was exposed to HCl vapor for the regeneration of cellulose film.

Other polymer films were prepared by immersing the cleaned solid substrates in 1.0 mg/ml aqueous solution of polylysine or PNIPAM for 1 hour at room temperature. The bulk polymers in the solution were washed away with copious amounts of water.

Separation medium preparation The separation bilayer was formed on polymer cushions by vesicle fusion.[9] The vesicle solution was prepared by vesicle extrusion.[47,48] Lipids dissolved in chloroform were dried under a stream of nitrogen followed by overnight vacuum desiccation. Next, the lipids were rehydrated in PBS solution. After five freeze-thaw cycles, the vesicles were extruded more than seven times through a polycarbonate filter (Whatman, Fisher Scientific) containing 50 nm pores. These vesicles had a size distribution centered around 70 nm as determined by dynamic light scattering (Brookhaven Instruments 90Plus Particle Size Analyzer). The vesicle solutions were incubated on polymer films for 10 min. The vesicles in bulk were then washed away with copious amounts of purified water.

To check the quality and fluidity of polymer-cushioned bilayers, FRAP studies were conducted using an inverted epifluorescence Nikon Eclipse TE2000-U microscope with a 10× objective. Laser radiation from a 2.5 W mixed gas Ar^+/K^+ laser (Stabilite 2018, Spectra Physics) was used to bleach the lipid bilayer samples. Fluorescence recovery after photobleaching (FRAP)[125] images were obtained with a MicroMax 1024b CCD camera (Princeton Instruments).

Electrophoresis Electrophresis in the polymer-cushioned lipid bilayer was conducted with a standard regulated power supply (Lambda Electronics Corp., Long Island, NY) while monitoring the current through the system with a digital multimeter (Keithly). A 100 V potential was applied laterally across the bilayer by using platinum wire electrodes. Purified water was used to minimize Joule heating. Joule heating was negligible since we maintained currents of only a few microamps or less during all experiments. Epifluorescence image were captured by a Nikon E800 fluorescence microscope with a Roper Scientific Micromax CCD camera. Time-lapse images were collected through a 4× Nikon objective to monitor the movement of the fluorescent bands and subsequent separations.

Results and Discussion

In a first set of experiments, the formation of lipid bilayers on polymer cushions was tested. TR-DHPE/POPC vesicles were used to demonstrate the vesicle fusion on polymer cushions. The inset fluorescence images in Figure 6.2 show that the TR-DHPE/POPC bilayer is uniform on the cellulose film down to the diffraction limit. The mobility of lipid molecules in the polymer-cushioned bilayer were confirmed by the FRAP technique. The diffusion constant calculated from the FRAP recovery curve was ~ 2.4 $\mu m^2/s$ with a mobile fraction of ~ 95%. Similar results were also obtained on polylysine and PNIPAM cushions.

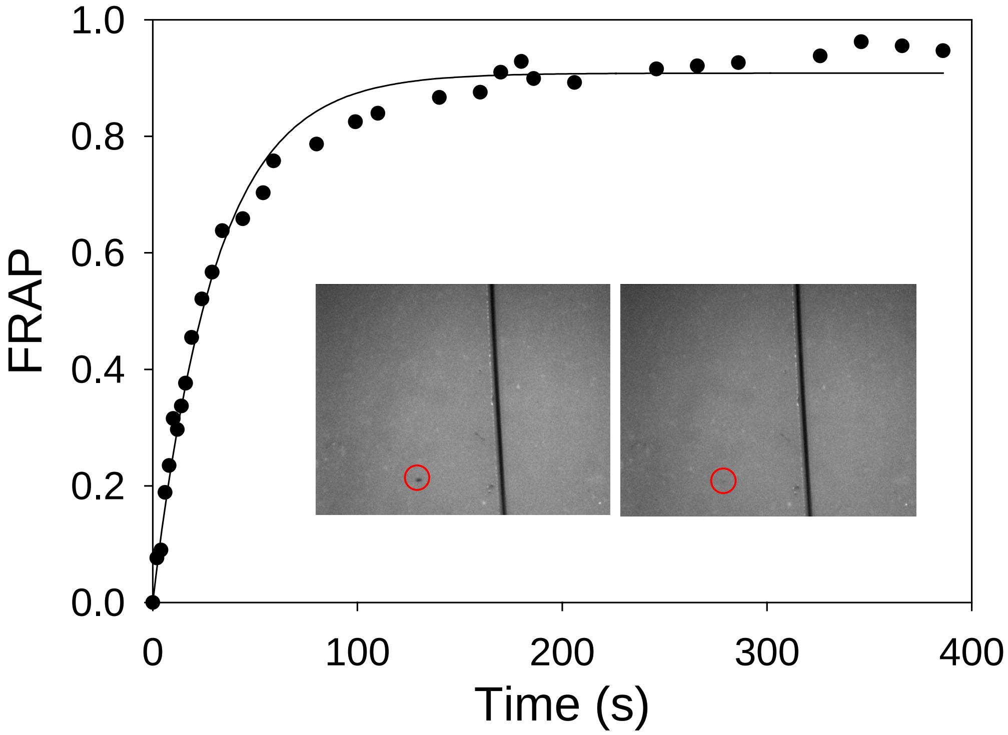

Figure 6.2. FRAP recovery curve for 0.1 mol% TR-DHPE/POPC bilayer on a cellulose cushion. Inset is the fluorescence images right after photobleaching and after recovery.

Next, it is necessary to test that membrane-associated species can be patterned in polymer-cushioned bilayer medium and separated. In this experiment, POPC bilayers containing TR-DHPE isomers were chosen for demonstration. At the beginning, DLPC bilayers with 25 mol% cholesterol and 2 mol% NBD-PE were formed on the PNIPAM thin film. Bilayers and polymers were then selectively removed by using either a sharp tip or deep UV radiation (~ 2.8 W, UVP Inc., Upland, CA). Deep UV with ~ 190 nm wavelength can completely remove the bilayer and polymer.[54,79,95] The surface was then washed with copious amounts of purified water. Next PNIPAM solution was again incubated with the patterned surface for 1 hour to refill the polymer gap. After washing away the polymers in bulk, vesicles containing 2.0 mol% TR-DHPE isomers were introduced into the aqueous phase above the surface for 10 min. Figure 6.3 illustrates that two thin lines of DLPC/cholesterol/NBD bilayer were removed by a sharp tip and the lines were refilled with POPC/TR-DHPE bilayers.

To demonstrate that the TX-DHPE isomers can be separated in the polymer-cushioned DLPC/cholesterol medium, an electric field was applied parallel to the bilayer plane. Epifluorescence images in Figure 6.4 show the original band was moved across the polymer-cushioned separation medium with compact format and resolved into two distinct band features after 30 min. The area ratio of the two bands is ~ 70:30, which is consistent with the result published by Daniel et al.[19] It is also proven that the separated bands represent two TX-DHPE isomers.[19] This result testify that electrophoresis in polymer-cushioned lipid bilayers is capable of separating membrane-associated species.

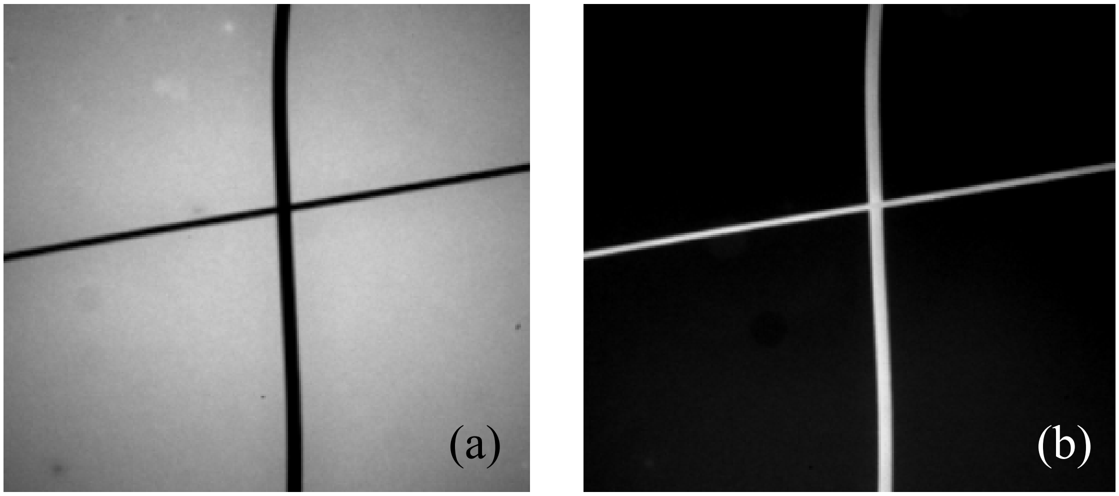

Figure 6.3. Epifluoresence image of (a) polymer-cushioned DLPC/cholesterol/NBD-PE bilayer after 10 min deep UV irradiation, and (b) POPC/TX-DHPE bilayer after polymer film regeneration and vesicle fusion.

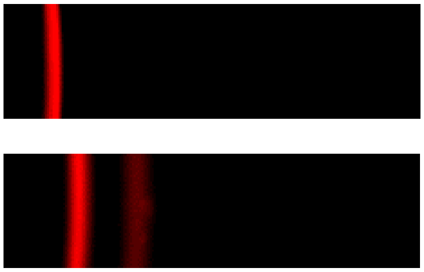

Figure 6.4. Separation of TX-DHPE isomers in a PNIPAM-cushioned DLPC/cholesterol medium. The top and bottom fluorescence signal comes from TX-DHPE before and after 30 min electrophoresis.

The possibility of extending the polymer-cushioned bilayer electrophoresis method to the purification and separation of membrane proteins is disscused in the final sets of experiments. For this purpose, we used E. Coli vesicles (~ 300 nm in diameter) containing overexpressed Tat (twin-arginine translocation) machinery as an exmaple. The E. Coli vesicle solution was incubated with the polymer-coated glass substrate for 1 hour. Then extra vesicles were washed away with copious amounts of water. To visualize the membrane on polymer cushions, Alex594 solution was added into the bulk solution. After one hour labeling reaction, the dye molecules in the solution were flushed away. It was assumed that the dye would link to the membrane proteins and membrane species with free amine groups, since E.Coli membrane contains high concentration phosphatidylethanolamines.[207]

The inset images in Figure 6.5 illustrate that Alexa594 molecules were labeled to the E. Coli membrane surface. To demonstrate E. coli vesicles can rupture to form polymer-cushioned biomembrane and the membrane is mobile, FRAP experiments were carried out for the mobility measurement of dye molecules. Results demonstrate that the fluorescence can get recovered after photobleaching, although it takes much more time than that in Figure 6.2. The FRAP recovery curve was fit to a double exponential equation, since Alexa594 was labeled to more than one species in the membrane. The diffusion constants calculated from the curve fitting was ~ 0.05 $\mu m^2/s$ and ~ 3.8 $\mu m^2/s$. The mobile fraction is ~ 74%. We speculate that the slow mobility comes from the dye-labeled proteins, and the fast from dye-labeled lipid molecules.

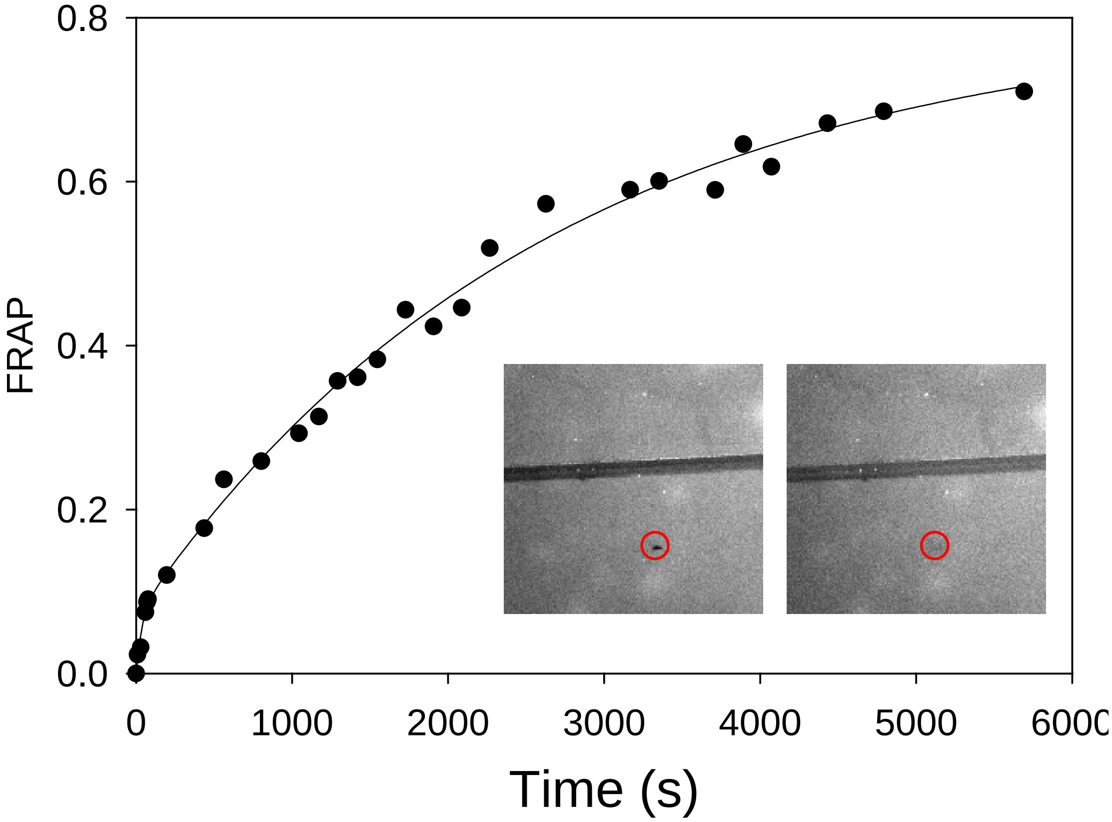

Figure 6.5. FRAP recovery curve for Alexa594-labeled E. Coli membrane on a polymer cushion. Inset is the fluorescence images immediately after photobleaching and 80min later.

The slow mobility of proteins may be ascribed to the high content of proteins associated in the membrane, which can even prevent the fusion of vesicles.[68] To solve the slow mobility problem, high protein concentration must be diluted. Several techniques have been proposed for this purpose by fusion of artificial SUVs with E. Coli vesicles to form lipid-enriched proteoliposomes.[68,208,209] The technique adopted in this chapter will utilize extrusion or sonication method to prepare small proteoliposomes, which are proven to be efficient for supported biomembrane formation. Experiments, including mixing E. Coli vesicles and artifical vesicles in various proportions for vesicle fusion and testing which one gives the best mobility, is in progress. With patterning of the E. Coli biomembrane containing highly mobile proteins adjacent to polymer-coushioned bilayer separation medium (Figure 6.1), it is expected the proteins could be moved and separated by electrophoresis.

Conclusion

The results presented in this chapter demonstrate that lipid bilayers can be deposited on different polymer cushions including cellulose, PNIPAM, and polylysine. Such polymer-supported lipid bilayers are uniform and mobile. Different biomembranes can be patterned together on polymer cushions by deep UV lithography. Electrophoresis isolation of lipid-tagged fluorophore isomers was achieved in polymer-cushioned bilayer separation medium containing the mixture of phospholipid and cholestrol. The result is consistent with the published studies using solid-supported lipid bilayers by Daniel et al.[19] This method is also extended to the separation of proteins in E. Coli membrane, since polymer cushiones are able to keep the membrane proteins mobile and functional.[26] The preliminary data demonstrate that E. Coli vesicles can rupture on polymer cushiones and form mobile bilayers. Although the protein mobility in the E. Coli membrane is slow, proteoliposome formation could be one way to solve this problem by diluting the high protein concentration with artificial vesicles. Further studies of proteoliposome preparation and electrophoresis separation of membrane proteins are underway.

CHAPTER VII

SUMMARY AND OUTLOOK

During my time at Texas A&M University, I have foucsed my research on the development of novel lithographic techniques for micro/nano-patterning supported lipid bilayers and have applied patterned biomembrane arrays to address some biophysical and bioanalytical questions. Here, I will summarize the research work I achieved and am currently doing. I will also discuss some potential future directions of SLB patterning.

My starting project was the study of multivalent interactions between CTB and GM_1 by using lipid bilayer-coated microfluidic platforms. Ligand density and ligand presentation effects on protein binding revealed that the CTB-GM_1 binding weakened with increasing GM_1 density. AFM demonstrated the clustering of GM_1 on the supported lipid bilayers, which in turn inhibits the binding of CTB. Although such bilayer-coated microfluidic devices showed high throughput and low consumption properties, these assays could still be improved considerably by measuring multiple binding constants for various membrane chemistries simultaneously. Deep UV lithography was utilized for arraying a variety of different lipid bilayers in individual microfluidic channels coated with one protein layer. Such two dimensional assays were successfully applied to probe multivalent binding as a function of four ligand densities in one-shot experiments. Bilayer-coated microfluidics is also useful for enzyme kinetics. Streptavidin conjugated enzymes were immobilized at the biotin sites in SLBs, and enzyme kinetics was monitored by fluorescence signal change from dephosphorylation reactions. Higher turnover rate and catalytic efficiency was observed at low enzyme surface density, which was ascribed to the high mobility of enzyme molecules on the membrane surface.

Next, sub-100 nm patterning of supported lipid bilayers was achieved by atomic force microscopy (AFM) based nanoshaving lithography. By considering the favorable bilayer adhesion energy and the unfavorable bilayer edge energy, it is believed that the phospholipid bilayer size limit of ~ 55 nm in width is inherent. The size limitations are also specific to the lipid composition of the membrane. Finally, polymer-cushioned lipid bilayers were proposed for electrophoretic separation of membrane-associated sepcies. Lipid-tagged fluorophore isomers were separated by this strategy. E. Coli ghost membrane formation on polymer cushions was demonstrated and the separation of membrane-associated proteins was discussed.

Supported lipid bilayer arrays will attract more and more applications in biophysical and bioanalytical studies, especially with the development of new patterning techniques. Lipid bilayer patterning in a single microchip can be utilized to study cell-matrix and cell-biomaterial interactions. For example, if SLB patches containing different ligands (such as RGD peptides)[210] are arrayed within individual microchannels, we can simultaneously observe the growth of cells on different patches, which will be useful for ligand screening. The adhesion of different cells on bilayer arrays can be employed in a high-throughput assay for studying interactions between cells and biomaterials (e.g. aptamer-conjugated micro/nano-particles).[211] Such bilayer-arrayed microfluidic platforms are also suitable for the study of blood clotting as a function of fluid flow and bilayer patch shape.[212] Besides, SLB arrays containing functional groups (e.g. carboxyl group) could play a role in controlling the growth of bio-inspired materials such as calcium carbonate.[213,214] The unique properties of SLBs will make them better templates mimicking the biomineralization in nature. Furthermore, the coupling of a temperature or concentration gradient[96] with such bilayer-arrayed platforms will make the tool much more powerful.

REFERENCES

(1) Whitesides, G. M.; Ostuni, E.; Takayama, S.; Jiang, X. Y.; Ingber, D. E. *Annu. Rev. Biomed. Eng.* **2001**, *3*, 335-373.

(2) Henzie, J.; Barton, J. E.; Stender, C. L.; Odom, T. W. *Acc. Chem. Res.* **2006**, *39*, 249-257.

(3) Tsai, I. Y.; Crosby, A. J.; Russell, T. P. *Cell Mech.* **2007**, *83*, 67-87.

(4) Salaita, K.; Wang, Y. H.; Mirkin, C. A. *Nat. Nanotech.* **2007**, *2*, 145-155.

(5) Fodor, S. P. A.; Read, J. L.; Pirrung, M. C.; Stryer, L.; Lu, A. T.; Solas, D. *Science* **1991**, *251*, 767-773.

(6) Xiang, X. D.; Sun, X. D.; Briceno, G.; Lou, Y. L.; Wang, K. A.; Chang, H. Y.; Wallacefreedman, W. G.; Chen, S. W.; Schultz, P. G. *Science* **1995**, *268*, 1738-1740.

(7) Reddington, E.; Sapienza, A.; Gurau, B.; Viswanathan, R.; Sarangapani, S.; Smotkin, E. S.; Mallouk, T. E. *Science* **1998**, *280*, 1735-1737.

(8) Mrksich, M.; Whitesides, G. M. *Trends Biotechnol.* **1995**, *13*, 228-235.

(9) Sackmann, E. *Science* **1996**, *271*, 43-48.

(10) Groves, J. T.; Ulman, N.; Boxer, S. G. *Science* **1997**, *275*, 651-653.

(11) Bayley, H.; Cremer, P. S. *Nature* **2001**, *413*, 226-230.

(12) Groves, J. T. *Curr. Opin. Drug Discov. Res.* **2002**, *5*, 606-612.

(13) Castellana, E. T.; Cremer, P. S. *Surf. Sci. Rep.* **2006**, *61*, 429-444.

(14) Groves, J. T.; Boxer, S. G. *Acc. Chem. Res.* **2002**, *35*, 149-157.

(15) Yang, T. L.; Jung, S. Y.; Mao, H. B.; Cremer, P. S. *Anal. Chem.* **2001**, *73*, 165-169.

(16) Yang, T. L.; Baryshnikova, O. K.; Mao, H. B.; Holden, M. A.; Cremer, P. S. *J. Am. Chem. Soc.* **2003**, *125*, 4779-4784.

(17) Mao, H. B.; Yang, T. L.; Cremer, P. S. *Anal. Chem.* **2002**, *74*, 379-385.

(18) Cremer, P. S.; Yang, T. L. *J. Am. Chem. Soc.* **1999**, *121*, 8130-8131.

(19) Daniel, S.; Diaz, A. J.; Martinez, K. M.; Bench, B. J.; Albertorio, F.; Cremer, P. S. *J. Am. Chem. Soc.* **2007**, *129*, 8072-8073.

(20) Braun, R. J.; Kinkl, N.; Beer, M.; Ueffing, M. *Anal. Bioanal. Chem.* **2007**, *389*, 1033-1045.

(21) Brian, A. A.; Mcconnell, H. M. *Proc. Natl. Acad. Sci.* **1984**, *81*, 6159-6163.

(22) Tamm, L. K.; Mcconnell, H. M. *Biophys. J.* **1985**, *47*, 105-113.

(23) Bayerl, T. M.; Bloom, M. *Biophys. J.* **1990**, *58*, 357-362.

(24) Koenig, B. W.; Kruger, S.; Orts, W. J.; Majkrzak, C. F.; Berk, N. F.; Silverton, J. V.; Gawrisch, K. *Langmuir* **1996**, *12*, 1343-1350.

(25) Johnson, S. J.; Bayerl, T. M.; Mcdermott, D. C.; Adam, G. W.; Rennie, A. R.; Thomas, R. K.; Sackmann, E. *Biophys. J.* **1991**, *59*, 289-294.

(26) Tanaka, M.; Sackmann, E. *Nature* **2005**, *437*, 656-663.

(27) Wolf, D. E. *Curr. Top. Membr.* **1994**, *40*, 143-165.

(28) Dietrich, C.; Bagatolli, L. A.; Volovyk, Z. N.; Thompson, N. L.; Levi, M.; Jacobson, K.; Gratton, E. *Biophys. J.* **2001**, *80*, 1417-1428.

(29) Chernomordik, L. V.; Kozlov, M. M. *Annu. Rev. Biochem.* **2003**, *72*, 175-207.

(30) Tamm, L. K.; Crane, J.; Kiessling, V. *Curr. Opin. Struc. Biol.* **2003**, *13*, 453-466.

(31) Shi, J. J.; Giano, M.; Yang, T. L.; Chen, X.; Jung, H. S.; Cremer, P. S. **2008**, *to be submitted*.

(32) Kalb, E.; Engel, J.; Tamm, L. K. *Biochemistry* **1990**, *29*, 1607-1613.

(33) Baksh, M. M.; Jaros, M.; Groves, J. T. *Nature* **2004**, *427*, 139-141.

(34) Shi, J. J.; Yang, T. L.; Kataoka, S.; Zhang, Y. J.; Diaz, A. J.; Cremer, P. S. *J. Am. Chem. Soc.* **2007**, *129*, 5954-5961.

(35) Groves, J. T.; Mahal, L. K.; Bertozzi, C. R. *Langmuir* **2001**, *17*, 5129-5133.

(36) Groves, J. T.; Dustin, M. L. *J. Immunol. Methods* **2003**, *278*, 19-32.

(37) Mossman, K. D.; Campi, G.; Groves, J. T.; Dustin, M. L. *Science* **2005**, *310*, 1191-1193.

(38) Ono, A.; Freed, E. O. *Proc. Natl. Acad. Sci.* **2001**, *98*, 13925-13930.

(39) Suzuki, K.; Hosokawa, K.; Maeda, M. *J. Am. Chem. Soc.* **2008**, *in press*.

(40) LoidlStahlhofen, A.; Kaufmann, S.; Braunschweig, T.; Bayerl, T. M. *Nat. Biotechnol.* **1996**, *14*, 999-1002.

(41) LoidlStahlhofen, A.; Ulrich, A. S.; Kaufmann, S.; Bayerl, T. M. *Eur. Biophys. J. Biophys. Lett.* **1996**, *25*, 151-153.

(42) Cunliffe, J. M.; Baryla, N. E.; Lucy, C. A. *Anal. Chem.* **2002**, *74*, 776-783.

(43) Wang, C. Z.; Lucy, C. A. *Anal. Chem.* **2005**, *77*, 2015-2021.

(44) Sackmann, E.; Tanaka, M. *Trends Biotechnol.* **2000**, *18*, 58-64.

(45) Mcconnell, H. M.; Watts, T. H.; Weis, R. M.; Brian, A. A. *Biochim. Biophys. Acta* **1986**, *864*, 95-106.

(46) Barenholz, Y.; Gibbes, D.; Litman, B. J.; Goll, J.; Thompson, T. E.; Carlson, F. D. *Biochemistry* **1977**, *16*, 2806-2810.

(47) Kalb, E.; Frey, S.; Tamm, L. K. *Biochim. Biophys. Acta* **1992**, *1103*, 307-316.

(48) Nollert, P.; Kiefer, H.; Jahnig, F. *Biophys. J.* **1995**, *69*, 1447-1455.

(49) Zasadzinski, J. A. N.; Helm, C. A.; Longo, M. L.; Weisenhorn, A. L.; Gould, S. A. C.; Hansma, P. K. *Biophys. J.* **1991**, *59*, 755-760.

(50) Plant, A. L. *Langmuir* **1993**, *9*, 2764-2767.

(51) Plant, A. L. *Langmuir* **1999**, *15*, 5128-5135.

(52) Cha, T.; Guo, A.; Zhu, X. Y. *Biophys. J.* **2006**, *90*, 1270-1274.

(53) Hillebrandt, H.; Wiegand, G.; Tanaka, M.; Sackmann, E. *Langmuir* **1999**, *15*, 8451-8459.

(54) Tanaka, M.; Wong, A. P.; Rehfeldt, F.; Tutus, M.; Kaufmann, S. *J. Am. Chem. Soc.* **2004**, *126*, 3257-3260.

(55) Goennenwein, S.; Tanaka, M.; Hu, B.; Moroder, L.; Sackmann, E. *Biophys. J.* **2003**, *85*, 646-655.

(56) Elender, G.; Kuhner, M.; Sackmann, E. *Biosens. Bioelectron.* **1996**, *11*, 565-577.

(57) Majewski, J.; Wong, J. Y.; Park, C. K.; Seitz, M.; Israelachvili, J. N.; Smith, G. S. *Biophys. J.* **1998**, *75*, 2363-2367.

(58) Wong, J. Y.; Majewski, J.; Seitz, M.; Park, C. K.; Israelachvili, J. N.; Smith, G. S. *Biophys. J.* **1999**, *77*, 1445-1457.

(59) Smith, E. A.; Coym, J. W.; Cowell, S. M.; Tokimoto, T.; Hruby, V. J.; Yamamura, H. I.; Wirth, M. J. *Langmuir* **2005**, *21*, 9644-9650.

(60) Ma, C.; Srinivasan, M. P.; Waring, A. J.; Lehrer, R. I.; Longo, M. L.; Stroeve, P. *Colloids Surf. B* **2003**, *28*, 319-329.

(61) Lindholm-Sethson, B. *Langmuir* **1996**, *12*, 3305-3314.

(62) Cornell, B. A.; BraachMaksvytis, V. L. B.; King, L. G.; Osman, P. D. J.; Raguse, B.; Wieczorek, L.; Pace, R. J. *Nature* **1997**, *387*, 580-583.

(63) Raguse, B.; Braach-Maksvytis, V.; Cornell, B. A.; King, L. G.; Osman, P. D. J.; Pace, R. J.; Wieczorek, L. *Langmuir* **1998**, *14*, 648-659.

(64) Fortig, A.; Jordan, R.; Graf, K.; Schiavon, G.; Purrucker, O.; Tanaka, M. *Macromol. Symp.* **2004**, *210*, 329-338.

(65) Lahiri, J.; Kalal, P.; Frutos, A. G.; Jonas, S. T.; Schaeffler, R. *Langmuir* **2000**, *16*, 7805-7810.

(66) Schiller, S. M.; Naumann, R.; Lovejoy, K.; Kunz, H.; Knoll, W. *Angew. Chem. Int. Edit* **2003**, *42*, 208-211.

(67) Berquand, A.; Mazeran, P. E.; Pantigny, J.; Proux-Delrouyre, V.; Laval, J. M.; Bourdillon, C. *Langmuir* **2003**, *19*, 1700-1707.

(68) Elie-Caille, C.; Fliniaux, O.; Pantigny, J.; Maziere, J. C.; Bourdillon, C. *Langmuir* **2005**, *21*, 4661-4668.

(69) Ulman, N.; Groves, J. T.; Boxer, S. G. *Adv. Mater.* **1997**, *9*, 1121-1123.

(70) Cremer, P. S.; Groves, J. T.; Kung, L. A.; Boxer, S. G. *Langmuir* **1999**, *15*, 3893-3896.

(71) Cremer, P. S.; Boxer, S. G. *J. Phys. Chem. B* **1999**, *103*, 2554-2559.

(72) Hovis, J. S.; Boxer, S. G. *Langmuir* **2000**, *16*, 894-897.

(73) Hovis, J. S.; Boxer, S. G. *Langmuir* **2001**, *17*, 3400-3405.

(74) Jung, S. Y.; Holden, M. A.; Cremer, P. S.; Collier, C. P. *ChemPhysChem* **2005**, *6*, 423-426.

(75) Majd, S.; Mayer, M. *Angew. Chem. Int. Edit* **2005**, *44*, 6697-6700.

(76) Orth, R. N.; Kameoka, J.; Zipfel, W. R.; Ilic, B.; Webb, W. W.; Clark, T. G.; Craighead, H. G. *Biophys. J.* **2003**, *85*, 3066-3073.

(77) Fang, Y.; Frutos, A. G.; Lahiri, J. *J. Am. Chem. Soc.* **2002**, *124*, 2394-2395.

(78) Yamazaki, V.; Sirenko, O.; Schafer, R. J.; Nguyen, L.; Gutsmann, T.; Brade, L.; Groves, J. T. *BMC Biotechnol.* **2005**, *5: 18*.

(79) Yee, C. K.; Amweg, M. L.; Parikh, A. N. *J. Am. Chem. Soc.* **2004**, *126*, 13962-13972.

(80) Yee, C. K.; Amweg, M. L.; Parikh, A. N. *Adv. Mater.* **2004**, *16*, 1184-1189.

(81) Mager, M. D.; Melosh, N. A. *Langmuir* **2007**, *23*, 9369-9377.

(82) Lenhert, S.; Sun, P.; Wang, Y. H.; Fuchs, H.; Mirkin, C. A. *Small* **2007**, *3*, 71-75.

(83) Shi, J. J.; Chen, J. X.; Cremer, P. S. *J. Am. Chem. Soc.* **2008**, *in press*.

(84) Kam, L.; Boxer, S. G. *J. Am. Chem. Soc.* **2000**, *122*, 12901-12902.

(85) Jackson, B. L.; Groves, J. T. *J. Am. Chem. Soc.* **2004**, *126*, 13878-13879.

(86) Yang, T. L.; Simanek, E. E.; Cremer, P. *Anal. Chem.* **2000**, *72*, 2587-2589.

(87) Dahlin, A.; Zach, M.; Rindzevicius, T.; Kall, M.; Sutherland, D. S.; Höök, F. *J. Am. Chem. Soc.* **2005**, *127*, 5043-5048.

(88) Jonsson, M. P.; Jönsson, P.; Dahlin, A. B.; Höök, F. *Nano Lett.* **2007**, *7*, 3462-3468.

(89) Orth, R. N.; Wu, M.; Holowka, D. A.; Craighead, H. G.; Baird, B. A. *Langmuir* **2003**, *19*, 1599-1605.

(90) Mossman, K.; Groves, J. *Chem. Soc. Rev.* **2007**, *36*, 46-54.

(91) Wu, M.; Holowka, D.; Craighead, H. G.; Baird, B. *Proc. Natl. Acad. Sci.* **2004**, *101*, 13798-13803.

(92) Griffitts, J. S.; Haslam, S. M.; Yang, T. L.; Garczynski, S. F.; Mulloy, B.; Morris, H.; Cremer, P. S.; Dell, A.; Adang, M. J.; Aroian, R. V. *Science* **2005**, *307*, 922-925.

(93) Cannon, B.; Weaver, N.; Pu, Q. S.; Thiagarajan, V.; Liu, S. R.; Huang, J. Y.; Vaughn, M. W.; Cheng, K. H. *Langmuir* **2005**, *21*, 9666-9674.

(94) Moran-Mirabal, J. M.; Edel, J. B.; Meyer, G. D.; Throckmorton, D.; Singh, A. K.; Craighead, H. G. *Biophys. J.* **2005**, *89*, 296-305.

(95) Shi, J. J.; Yang, T. L.; Cremer, P. S. **2008**, *to be submitted.*

(96) Mao, H. B.; Yang, T. L.; Cremer, P. S. *J. Am. Chem. Soc.* **2002**, *124*, 4432-4435.

(97) Choi, S. K. *Synthetic Multivalent Molecules*; Wiley: Hoboken, N.J., 2004.

(98) Heldin, C. H. *Cell* **1995**, *80*, 213-223.

(99) Mammen, M.; Choi, S. K.; Whitesides, G. M. *Angew. Chem. Int. Edit* **1998**, *37*, 2755-2794.

(100) Baranowski, E.; Ruiz-Jarabo, C. M.; Domingo, E. *Science* **2001**, *292*, 1102-1105.

(101) Kiessling, L. L.; Pohl, N. L. *Chem. Biol.* **1996**, *3*, 71-77.

(102) Keizer, J. *Acc. Chem. Res.* **1985**, *18*, 235-241.

(103) Mourez, M.; Kane, R. S.; Mogridge, J.; Metallo, S.; Deschatelets, P.; Sellman, B. R.; Whitesides, G. M.; Collier, R. J. *Nat. Biotechnol.* **2001**, *19*, 958-961.

(104) Kiessling, L. L.; Gestwicki, J. E.; Strong, L. E. *Angew. Chem. Int. Edit* **2006**, *45*, 2348-2368.

(105) Cuatreca.P *Biochemistry* **1973**, *12*, 3547-3558.

(106) Cuatreca.P *Biochemistry* **1973**, *12*, 3558-3566.

(107) Holmgren, J.; Lonnroth, I.; Mansson, J. E.; Svennerholm, L. *Proc. Natl. Acad. Sci.* **1975**, *72*, 2520-2524.

(108) Goins, B.; Freire, E. *Biochemistry* **1988**, *27*, 2046-2052.

(109) Schon, A.; Freire, E. *Biochemistry* **1989**, *28*, 5019-5024.

(110) Terrettaz, S.; Stora, T.; Duschl, C.; Vogel, H. *Langmuir* **1993**, *9*, 1361-1369.

(111) Kuziemko, G. M.; Stroh, M.; Stevens, R. C. *Biochemistry* **1996**, *35*, 6375-6384.

(112) MacKenzie, C. R.; Hirama, T.; Lee, K. K.; Altman, E.; Young, N. M. *J. Biol. Chem.* **1997**, *272*, 5533-5538.

(113) Cooper, M. A.; Hansson, A.; Lofas, S.; Williams, D. H. *Anal. Biochem.* **2000**, *277*, 196-205.

(114) Janshoff, A.; Steinem, C.; Sieber, M.; elBaya, A.; Schmidt, M. A.; Galla, H. J. *Eur. Biophys. J. Biophys. Lett.* **1997**, *26*, 261-270.

(115) Lauer, S.; Goldstein, B.; Nolan, R. L.; Nolan, J. P. *Biochemistry* **2002**, *41*, 1742-1751.

(116) Singh, A. K.; Harrison, S. H.; Schoeniger, J. S. *Anal. Chem.* **2000**, *72*, 6019-6024.

(117) Ma, G. Y.; Cheng, Q. *Langmuir* **2006**, *22*, 6743-6745.

(118) Cai, X. E.; Yang, J. *Biochemistry* **2003**, *42*, 4028-4034.

(119) Winter, E. M.; Groves, J. T. *Anal. Chem.* **2006**, *78*, 174-180.

(120) Smith, E. A.; Thomas, W. D.; Kiessling, L. L.; Corn, R. M. *J. Am. Chem. Soc.* **2003**, *125*, 6140-6148.

(121) Huskens, J.; Mulder, A.; Auletta, T.; Nijhuis, C. A.; Ludden, M. J. W.; Reinhoudt, D. N. *J. Am. Chem. Soc.* **2004**, *126*, 6784-6797.

(122) Lencer, W. I.; Chu, S. H.; Walker, W. A. *Infect. Immun.* **1987**, *55*, 3126-3130.

(123) Xia, Y. N.; Whitesides, G. M. *Angew. Chem. Int. Edit* **1998**, *37*, 551-575.

(124) Lin, C. H.; Lee, G. B.; Lin, Y. H.; Chang, G. L. *J. Micromech. Microeng.* **2001**, *11*, 726-732.

(125) Axelrod, D.; Koppel, D. E.; Schlessinger, J.; Elson, E.; Webb, W. W. *Biophys. J.* **1976**, *16*, 1055-1069.

(126) Albertorio, F.; Diaz, A. J.; Yang, T. L.; Chapa, V. A.; Kataoka, S.; Castellana, E. T.; Cremer, P. S. *Langmuir* **2005**, *21*, 7476-7482.

(127) Howland, M. C.; Sapuri-Butti, A. R.; Dixit, S. S.; Dattelbaum, A. M.; Shreve, A. P.; Parikh, A. N. *J. Am. Chem. Soc.* **2005**, *127*, 6752-6765.

(128) Axelrod, D.; Burghardt, T. P.; Thompson, N. L. *Annu. Rev. Biophys. Bioeng.* **1984**, *13*, 247-268.

(129) Starr, T. E.; Thompson, N. L. *Biophys. J.* **2001**, *80*, 1575-1584.

(130) Burmeister, J. S.; Olivier, L. A.; Reichert, W. M.; Truskey, G. A. *Biomaterials* **1998**, *19*, 307-325.

(131) Doudevski, I.; Schwartz, D. K. *Phys. Rev. B* **1999**, *60*, 14-17.

(132) Losic, D.; Short, K.; Gooding, J. J.; Shapter, J. G. *J. Serb. Chem. Soc.* **2004**, *69*, 93-106.

(133) Pisarchick, M. L.; Thompson, N. L. *Biophys. J.* **1990**, *58*, 1235-1249.

(134) Yuan, C. B.; Johnston, L. J. *Biophys. J.* **2001**, *81*, 1059-1069.

(135) Mcdaniel, R. V.; Mcintosh, T. J. *Biophys. J.* **1986**, *49*, 94-96.

(136) Mcintosh, T. J.; Simon, S. A. *Biochemistry* **1994**, *33*, 10477-10486.

(137) White, S. H.; King, G. I. *Proc. Natl. Acad. Sci.* **1985**, *82*, 6532-6536.

(138) Israelachvili, J. N. *Intermolecular and Surface Forces*, 2nd ed.; Academic Press: San Diego, CA, 1991.

(139) Merritt, E. A.; Sarfaty, S.; Vandenakker, F.; Lhoir, C.; Martial, J. A.; Hol, W. G. J. *Protein Sci.* **1994**, *3*, 166-175.

(140) Turnbull, W. B.; Precious, B. L.; Homans, S. W. *J. Am. Chem. Soc.* **2004**, *126*, 1047-1054.

(141) Sharom, F. J.; Grant, C. W. M. *Biochim. Biophys. Acta* **1978**, *507*, 280-293.

(142) Peters, M. W.; Mehlhorn, I. E.; Barber, K. R.; Grant, C. W. M. *Biochim. Biophys. Acta* **1984**, *778*, 419-428.

(143) Fantini, J. G., N.; Mahfoud, R.; Yahi, N. *Lipid Rafts: Structure, Function and Role in HIV, Alzheimer's and Prion Diseases*; Cambridge University Press: UK, 2002.

(144) van der Goot, F. G.; Harder, T. *Semin. Immunol.* **2001**, *13*, 89-97.

(145) Wolf, A. A.; Jobling, M. G.; Wimer-Mackin, S.; Ferguson-Maltzman, M.; Madara, J. L.; Holmes, R. K.; Lencer, W. I. *J. Cell Biol.* **1998**, *141*, 917-927.

(146) Clemons, P. A. *Curr. Opin. Chem. Biol.* **1999**, *3*, 112-115.

(147) Lee, H. J.; Goodrich, T. T.; Corn, R. M. *Anal. Chem.* **2001**, *73*, 5525-5531.

(148) Wegner, G. J.; Lee, H. J.; Corn, R. M. *Anal. Chem.* **2002**, *74*, 5161-5168.

(149) Su, J.; Bringer, M. R.; Ismagilov, R. F.; Mrksich, M. *J. Am. Chem. Soc.* **2005**, *127*, 7280-7281.

(150) Holden, M. A.; Jung, S. Y.; Cremer, P. S. *Anal. Chem.* **2004**, *76*, 1838-1843.

(151) Yu, C. H.; Parikh, A. N.; Groves, J. T. *Adv. Mater.* **2005**, *17*, 1477-1480.

(152) Dulcey, C. S.; Georger, J. H.; Krauthamer, V.; Stenger, D. A.; Fare, T. L.; Calvert, J. M. *Science* **1991**, *252*, 551-554.

(153) Mooney, J. F.; Hunt, A. J.; McIntosh, J. R.; Liberko, C. A.; Walba, D. M.; Rogers, C. T. *Proc. Natl. Acad. Sci.* **1996**, *93*, 12287-12291.

(154) Sleytr, U. B.; Messner, P.; Pum, D.; Sara, M. *Angew. Chem. Int. Edit* **1999**, *38*, 1035-1054.

(155) Wertz, C. F.; Santore, M. M. *Langmuir* **2001**, *17*, 3006-3016.

(156) Kung, L. A.; Kam, L.; Hovis, J. S.; Boxer, S. G. *Langmuir* **2000**, *16*, 6773-6776.

(157) Brown, R. F. *Biochim. Biophys. Acta* **1992**, *1113*, 375-389

(158) Kaji, H.; Tsukidate, K.; Matsue, T.; Nishizawa, M. *J. Am. Chem. Soc.* **2004**, *126*, 15026-15027.

(159) Tinazli, A.; Piehler, J.; Beuttler, M.; Guckenberger, R.; Tampe, R. *Nat. Nanotech.* **2007**, *2*, 220-225

(160) Willner, I.; Katz, E. *Angew. Chem. Int. Edit* **2000**, *39*, 1180-1218.

(161) Holden, M. A.; Cremer, P. S. *J. Am. Chem. Soc.* **2003**, *125*, 8074-8075.

(162) Chaplin, M. F. B., C. *Enzyme Technology*; Cambridge University Press: New York, 1990.

(163) Kim, J.; Jia, H. F.; Wang, P. *Biotechnol. Adv.* **2006**, *24*, 296-308.

(164) Bickerstaff, G. F. *Immobilization of Enzymes and Cells*; Humana Press: Totowa, N.J., 1997.

(165) Gleason, N. J.; Carbeck, J. D. *Langmuir* **2004**, *20*, 6374-6381.

(166) Zhen, G. L.; Eggli, V.; Voros, J.; Zammaretti, P.; Textor, M.; Glockshuber, R.; Kuennemann, E. *Langmuir* **2004**, *20*, 10464-10473.

(167) Xu, F.; Zhen, G. L.; Yu, F.; Kuennemann, E.; Textor, M.; Knoll, W. *J. Am. Chem. Soc.* **2005**, *127*, 13084-13085.

(168) DeLouise, L. A.; Kou, P. M.; Miller, B. L. *Anal. Chem.* **2005**, *77*, 3222-3230.

(169) Vianello, F.; Zennaro, L.; Di Paolo, M. L.; Rigo, A.; Malacarne, C.; Scarpa, M. *Biotech. Bioeng.* **2000**, *68*, 488-495.

(170) Caseli, L.; Furriel, R. P. M.; de Andrade, J. F.; Leone, F. A.; Zaniquelli, M. E. D. *J. Colloid Interf. Sci.* **2004**, *275*, 123-130.

(171) Edmiston, P. L.; Saavedra, S. S. *Biophys. J.* **1998**, *74*, 999-1006.

(172) Huang, W.; Wang, J. Q.; Bhattacharyya, D.; Bachas, L. G. *Anal. Chem.* **1997**, *69*, 4601-4607.

(173) Jayakumari, V. G.; Pillai, V. N. R. *J. Appl. Polym. Sci.* **1991**, *42*, 583-590.

(174) Penzol, G.; Armisen, P.; Fernandez-Lafuente, R.; Rodes, L.; Guisan, J. M. *Biotech. Bioeng.* **1998**, *60*, 518-523.

(175) Nouaimi, M.; Moschel, K.; Bisswanger, H. *Enzyme Microb. Tech.* **2001**, *29*, 567-574.

(176) Edmiston, P. L.; Saavedra, S. S. *J. Am. Chem. Soc.* **1998**, *120*, 1665-1671.

(177) Voet, D. V., J. G.; Charlotte, W. P. *Fundamentals of Biochemistry*, Upgrade ed.; John Wiley & Sons: New York, 2002.

(178) Kim, E. E.; Wyckoff, H. W. *J. Mol. Biol.* **1991**, *218*, 449-464.

(179) Chilkoti, A.; Stayton, P. S. *J. Am. Chem. Soc.* **1995**, *117*, 10622-10628.

(180) Strittmatter, P.; Rogers, M. J. *Proc. Natl. Acad. Sci.* **1975**, *72*, 2658-2661.

(181) Brune, D.; Kim, S. *Proc. Natl. Acad. Sci.* **1993**, *90*, 3835-3839.

(182) Liu, M. K.; Li, P.; Giddings, J. C. *Protein Sci.* **1993**, *2*, 1520-1531.

(183) Litster, J. D. *Phys. Lett. A* **1975**, *A 53*, 193-194.

(184) Lipowsky, R.; Seifert, U. *Mol. Cryst. Liq. Cryst.* **1991**, *202*, 17-25.

(185) Xu, S.; Liu, G. Y. *Langmuir* **1997**, *13*, 127-129.

(186) Wadu-Mesthrige, K.; Amro, N. A.; Garno, J. C.; Xu, S.; Liu, G. Y. *Biophys. J.* **2001**, *80*, 1891-1899.

(187) Jang, C. H.; Stevens, B. D.; Carlier, P. R.; Calter, M. A.; Ducker, W. A. *J. Am. Chem. Soc.* **2002**, *124*, 12114-12115.

(188) Liu, M. Z.; Amro, N. A.; Chow, C. S.; Liu, G. Y. *Nano Lett.* **2002**, *2*, 863-867.

(189) Schonherr, H.; Rozkiewicz, D. I.; Vancso, G. J. *Langmuir* **2004**, *20*, 7308-7312.

(190) Mullineaux, C. W.; Tobin, M. J.; Jones, G. R. *Nature* **1997**, *390*, 421-424.

(191) 1,2-Dipalmitoyl-sn-glycero-3-phosphoethanolamine-N-(7-nitro-2-1,3-benzoxadiazol-4-yl), ammonium salt (NBD-PE).

(192) Radler, J.; Strey, H.; Sackmann, E. *Langmuir* **1995**, *11*, 4539-4548.

(193) Schonherr, H.; Johnson, J. M.; Lenz, P.; Frank, C. W.; Boxer, S. G. *Langmuir* **2004**, *20*, 11600-11606.

(194) Nissen, J.; Gritsch, S.; Wiegand, G.; Radler, J. O. *Eur. Phys. J. B* **1999**, *10*, 335-344.

(195) Jiang, F. Y.; Bouret, Y.; Kindt, J. T. *Biophys. J.* **2004**, *87*, 182-192.

(196) Zhelev, D. V.; Needham, D. *Biochim. Biophys. Acta* **1993**, *1147*, 89-104.

(197) Taupin, C.; Dvolaitzky, M.; Sauterey, C. *Biochemistry* **1975**, *14*, 4771-4775.

(198) Genco, I.; Gliozzi, A.; Relini, A.; Robello, M.; Scalas, E. *Biochim. Biophys. Acta* **1993**, *1149*, 10-18.

(199) Chernomordik, L. V.; Kozlov, M. M.; Melikyan, G. B.; Abidor, I. G.; Markin, V. S.; Chizmadzhev, Y. A. *Biochim. Biophys. Acta* **1985**, *812*, 643-655.

(200) Sanders, C. R.; Schwonek, J. P. *Biochemistry* **1992**, *31*, 8898-8905.

(201) Poo, M. M.; Robinson, K. R. *Nature* **1977**, *265*, 602-605.

(202) Stelzle, M.; Miehlich, R.; Sackmann, E. *Biophys. J.* **1992**, *63*, 1346-1354.

(203) Groves, J. T.; Boxer, S. G. *Biophys. J.* **1995**, *69*, 1972-1975.

(204) Yoshina-Ishii, C.; Boxer, S. G. *Langmuir* **2006**, *22*, 2384-2391.

(205) Groves, J. T.; Wulfing, C.; Boxer, S. G. *Biophys. J.* **1996**, *71*, 2716-2723.

(206) Schaub, M.; Wenz, G.; Wegner, G.; Stein, A.; Klemm, D. *Adv. Mater.* **1993**, *5*, 919-922

(207) Dowhan, W.; Bogdanov, M. In *Biochemistry of Lipids, Lipoproteins and Membranes,* 4th ed.; Vance, D. E., Vance, J. E., Eds.; Elsevier: Amsterdam; Boston 2002; Vol. 1.

(208) Schneider, H.; Lemasters, J. J.; Hochli, M.; Hackenbrock, C. R. *Proc. Natl. Acad. Sci.* **1980**, *77*, 442-446.

(209) Casadio, R.; Venturoli, G.; Digioia, A.; Castellani, P.; Leonardi, L.; Melandri, B. A. *J. Biol. Chem.* **1984**, *259*, 9149-9157.

(210) Jensen, T. W.; Hu, B. H.; Delatore, S. M.; Garcia, A. S.; Messersmith, P. B.; Miller, W. M. *J. Am. Chem. Soc.* **2004**, *126*, 15223-15230.

(211) Farokhzad, O. C.; Khademhosseini, A.; Yon, S. Y.; Hermann, A.; Cheng, J. J.; Chin, C.; Kiselyuk, A.; Teply, B.; Eng, G.; Langer, R. *Anal. Chem.* **2005**, *77*, 5453-5459.

(212) Kastrup, C. J.; Ismagilov, R. F. *J. Phys. Org. Chem.* **2007**, *20*, 711-715.

(213) Meldrum, F. C. *Int. Mater. Rev.* **2003**, *48*, 187-224.

(214) Aizenberg, J.; Muller, D. A.; Grazul, J. L.; Hamann, D. R. *Science* **2003**, *299*, 1205-1208.

VITA

JINJUN SHI

Department of Chemistry
Texas A&M University
College Station, TX 77843-3255
E-mail: jshi@mail.chem.tamu.edu

Education

2003-2008	Ph.D. in Chemistry Texas A&M University, College Station, TX; GPA: 4.0/4.0 Thesis: Micro/Nano-Patterning of Supported Lipid Bilayers: Biophysical Studies and Membrane-Associated Species Separation Advisor: Professor Paul S. Cremer
1996-2000	B.S. in Chemistry Tsinghua University, Beijing, P.R. China; GPA: 3.7/4.0 Thesis: Development of Nanomaterial Based Optical Sensors Advisor: Professor Xinrong Zhang and Professor Yongfa Zhu

Selected Publications

(1) Shi, J.J.; Yang, T.L.; Cremer, P.S. “Multiple Multivalent Ligand-Receptor Interactions Measurement Within One-Shot Binding Experiments”, *to be submitted*

(2) Shi, J.J.; Chen, J.X.; Cremer, P.S. “Sub-100 nm Patterning of Supported Bilayers by Nanoshaving Lithography” ***J. Am. Chem. Soc.*** 2008, *130*, 2718-2719.

(3) Shi, J.J.; Yang, T.L.; Kataoka, S.; Zhang, Y.J.; Diaz, A.J.; Cremer, P.S. “GM_1 Clustering Inhibits Cholera Toxin Binding in Supported Phospholipid Membranes” ***J. Am. Chem. Soc.*** 2007, *129*, 5954-5961.

(4) Shi, J.J.; Zhu, Y.F.; Zhang, X.R.; Baeyens, W.R.G.; García-Campaña, A.M. “Recent Developments in Nanomaterial Optical Sensors” ***TRAC-Trends in Anal. Chem.*** 2004, 23, 351-360

(5) Zhu, Y.F.; Shi, J.J.; Zhang, Z.Y.; Zhang, C.; Zhang, X.R. “Development of a New Gas Sensor Utilizing Chemiluminescence on Nanosized Titanium Dioxide” ***Anal. Chem.*** 2002, 74, 120-124